

Effects of Advanced Material Morphologies on
Thermal, Electrical and Thermo-electric Properties

by

Faizan Ejaz

A Dissertation Presented in Partial Fulfillment
of the Requirements for the Degree
Doctor of Philosophy

Approved March 2023 by the
Graduate Supervisory Committee:

Beomjin Kwon, Chair
Houlong Zhuang
Kenan Song
Robert Wang
Wonmo Kang

ARIZONA STATE UNIVERSITY

May 2023

ABSTRACT

Progressive miniaturization in electronics demands advanced materials with excellent energy conversion and transport properties. Opportunities exist in novel material morphologies such as hierarchical structures, multi-functional composites and nanoscale architectures which may offer mechanical, thermal and electronic properties tailored to a wide range of applications (e.g., aerospace, robotics, biomedical etc.). However, the manufacturing capabilities have always posed a grand challenge in realizing the advanced material morphologies. Furthermore, the multi-scale modeling of complex material architectures has been extremely challenging owing to the limitations in computation methodologies and lack of understanding in nano-/micro-meter scale physics. To address these challenges, this work considers the morphology effect on carbon nanotube (CNT)-based composites, CNT fibers and thermoelectric (TE) materials. First, this work reports additively manufacturable TE morphologies and analyzes the thermo-electric transport behavior. This research introduces innovative honeycomb TE architectures that showed ~26% efficiency increase and ~25% density reduction compared to conventional rectangular TE architectures. Moreover, this work presents 3D printable compositionally segmented TE architecture which provides record-high efficiencies (up to 8.7%) over wide temperature ranges if the composition and aspect ratio of multiple TE materials are optimized within a single TE device. Next, this research proposes computationally efficient two-dimensional (2D) finite element model (FEM) to study the electrical and thermal properties in CNT based composites by simultaneously considering the stochastic CNT distributions, CNT fractions (upto 80%) and interfacial resistances. The FEM allows to

estimate the theoretical maximum possible conductivities with corresponding interfacial resistances if the CNT morphologies are carefully controlled, along with appreciable insight into the energy transport physics. Then, this work proposes a data-driven surrogate model based on convolutional neural networks to rapidly approximate the composite conductivities in a second with accuracy $> 98\%$, compared to FEM taking >100 minutes per simulation. Finally, this research presents a pseudo 2D FEM to approximate the electrical and thermal properties in CNT fibers at various CNT aspect ratios (up to 10,000) by simultaneously considering CNT-CNT interfacial effects along with the stochastic distribution of inter-bundle voids.

DEDICATION

To my family

for their unconditional love and encouragement

ACKNOWLEDGMENTS

First and foremost, I would like to acknowledge and express extreme gratitude to my advisor and mentor, Prof. Beomjin Kwon, for his generous support and guidance throughout my PhD career. I have greatly benefited from his incredible insight and intuition. I would also like to thank the members of my Supervisory Committee, Prof. Houlong Zhuang, Prof. Kenan Song, Prof. Robert Wang, and Prof. Wonmo Kang, for their time and providing constructive criticism, valuable suggestions, and comments. I would like to express my gratitude to my friends, who have always supported and encouraged me during my Ph.D journey.

I would like to acknowledge the funding sources that supported the research presented in this dissertation, including: (i) ASU startup fund; (ii) Korea Institute of Science and Technology (Grant No. 2Z06541).

TABLE OF CONTENTS

	Page
LIST OF TABLES	viii
LIST OF FIGURES	ix
CHAPTER	
1. INTRODUCTION	1
1.1. Material Morphology on Various Scales.....	1
1.2. Significance of Material Morphologies on Thermal Transport.....	2
1.3. Significance of Material Morphologies on Electrical Transport	4
1.4. Significance of Material Morphologies on Thermoelectric Transport	5
1.5. Research Objectives.....	6
2. ENERGY CONVERSION MODELING IN 3D PRINTABLE THERMOELECTRIC CELLULAR ARCHITECTURES	9
2.1. Abstract	9
2.2. Introduction.....	9
2.3. Problem Statement and Background Review	11
2.4. Finite Element Model	13
2.5. FEM Results and Discussion.....	17
2.6. Comparison to Experimental Samples	19
2.7. Conclusions.....	22
2.8. References.....	23

CHAPTER	Page
3. ENERGY CONVERSION MODELING IN 3D PRINTABLE COMPOSITIONALLY SEGMENTED THERMOELECTRIC LEGS	28
3.1. Abstract	28
3.2. Introduction	29
3.3. Problem Statement and Background Review	29
3.4. FEM and Experiment Results.....	31
3.5. Conclusions.....	35
3.6. References.....	36
4. NON-LINEAR TRANSPORT MECHANISM MODELING IN COPPER- CARBON NANOTUBE COMPOSITES	43
4.1. Abstract	43
4.2. Introduction.....	43
4.3. Background Review and Problem Statement.....	44
4.4. Finite Element Model	49
4.4.1. Generation of Stochastic Cu-CNT networks	53
4.4.2. Computational Domain size and Grid Independence Test	54
4.5. Model Estimations and Comparison to Experiments	56
4.6. Conclusions	64
4.7. References	65

CHAPTER	Page
5. DATA-DRIVEN MODELING OF TRANSPORT MECHANISMS IN COPPER-CARBON NANOTUBE COMPOSITES	71
5.1. Introduction	71
5.2. Background Review and Problem Statement	72
5.3. Training Data Generation	73
5.4. Convolutional Neural Network.....	77
5.5. Results and Discussion	79
5.6. Conclusions.....	83
6. NON-LINEAR TRANSPORT MECHANISM MODELING IN CARBON-NANOTUBE FIBERS	84
6.1. Introduction.....	84
6.2. Finite Element Model	86
6.3. Domain Independence Analysis	90
6.4. Results and Discussion	91
6.5. Conclusions	94
7. CONCLUSION AND FUTURE WORK.....	96
7.1. Conclusions	96
7.2. Future Work	99
REFERENCES	102
APPENDIX	
A. PERMISSION STATEMENTS.....	117

LIST OF TABLES

Table	Page
4.1. Properties Used to Simulate the Cu-CNT Composites	53
5.1. CNN Model R^2 and Training Time with Various Hidden Layer Neurons.....	80

LIST OF FIGURES

Figure	Page
1.1. Material Morphologies on Various Scales.....	2
1.2. Various Material Categories Compared to Manufacturing Difficulty and Resource Dependence to Property-to-cost Ratio	7
2.1. Design of Cu ₂ Se TE Cellular Architectures.....	16
2.2. Scheme for 3D Printing Process of the Cu ₂ Se-based Honeycomb Cellular Architecture by Using All Inorganic Cu _{2-x} Se Ink	19
2.3. Comparison of Cuboid, Hexagonal and Honeycomb Properties	21
3.1. Scheme of a Sequential 3D Printing of Multi-segmented TE Materials	31
3.2. Compositionally Segmented BiSbTe TEG	33
4.1. (a) 3D Schematic of a Cu-CNT Composite. (b) Three Types of Contacts in Cu-CNT Composites.....	50
4.2. Cu-CNT Composite Model Generation: (a) Locating CNTs at y_1 , (b) Locating CNTs at y_2 , (c) Locating CNTs at All y Positions, and (d) Giving Random Offsets to CNTs and Truncating CNTs Outside the Domain $L \times W$	52
4.3. Randomly Generated Cu-CNT Composite Models with (a) $f = 5\%$, (b) $f = 20\%$, (c) $f =$ 50% , and (d) $f = 80\%$	53
4.4. Electrical and Thermal Conductivities at Various Interfacial Resistances and Range of Domain Sizes	55
4.5. σ_e/σ_m as a Function of f for Different R_c	57

Figure	Page
4.6. Electrical Potential Distributions in a Cu-CNT Composite when (a) $f = 20\%$, $R_c = 60 \Omega$, (b) $f = 20\%$, $R_c = 60 \text{ k}\Omega$, (c) $f = 80\%$, $R_c = 60 \Omega$, and (d) $f = 80\%$, $R_c = 60 \text{ k}\Omega$	60
4.7. k_e/k_m as a Function of f for Different $R''_{t,c}$	61
4.8. Temperature Distributions in a Cu-CNT Composite when (a) $f = 20\%$, $R''_{t,c} = 10^{-10} \text{ m}^2\text{W/K}$, (b) $f = 20\%$, $R''_{t,c} = 10^{-7} \text{ m}^2\text{W/K}$, (c) $f = 80\%$, $R''_{t,c} = 10^{-10} \text{ m}^2\text{W/K}$, and (d) $f = 80\%$, $R''_{t,c} = 10^{-7} \text{ m}^2\text{W/K}$	63
5.1. (a) Schematics of Cu-CNT Networks with Various CNT fractions f , (b) Schematic of a Cu-CNT Network with Boundary Conditions	75
5.2. Schematic for the Data Preparation	76
5.3. The Architecture of CNN to Approximate the Effective Electrical and Thermal Conductivities of Cu-CNT Networks	78
5.4. Comparison between CNN Approximations and FEM Predictions for (a) Effective Electrical Conductivities with $R^2_{Train} = 0.991$, $R^2_{Valid} = 0.982$, and (b) Effective Thermal Conductivities with $R^2_{Train} = 0.992$, $R^2_{Valid} = 0.986$	82
6.1. 2-row CNT Bundle Extracted from 3D Schematic of CNT Fiber	87
6.2. (a) Schematic of 2D CNT Fiber Layout, (b) Resistive Element for the Type-I (End-to-End) CNT Interface (Left) and Resistive Element for the Type-II (Side-to-Side) CNT Interface	88

Figure	Page
6.3. (a) Effective Thermal Conductivity as a Function of CNT Fiber Width, d , and (b) Effective Thermal Conductivity as a Function of CNT Fiber Length, L	91
6.4. Effective Electrical Conductivity as a Function of CNT Aspect Ratio for (a) $\sigma_{CNT} = 7.1 \times 10^6$ S/m and (b) $\sigma_{CNT} = 7.1 \times 10^9$ S/m.....	92
6.5. Effective Thermal Conductivity as a Function of CNT Aspect Ratio for (a) $k_{CNT} = 500$ W/mK and (b) $k_{CNT} = 1000$ W/mK	93

1. INTRODUCTION

1.1. Material Morphology on Various Scales

Material morphology, in general, defines the shape, size, and structure of an architecture [1]. The term ‘morphology’ is defined and perceived in various ways depending on scale of analysis (i.e., atomic, nano, macro, and miniscale). Figure 1.1 shows the type of morphologies on various analysis scales. On atomic scale, the lattice arrangement of atoms in single crystal defines the material morphology, often terms as crystal morphology [2]. The intrinsic physical and chemical properties of a material are governed by the atomic level morphologies [2,3]. The nanoscale morphologies are defined by arrangement of grains and grain boundaries in structure, termed as grain morphologies[4]. The grain boundaries characterize the macroscopic as-built material properties [4]. In microscale morphologies, the arrangement, orientation, and location of constituent elements are defined, e.g., carbon nanotube distribution in metallic/polymer matrix [5]. The effective composite material properties are controlled and influenced by such morphologies [5]. On macroscale particularly with cellular materials, the size, shape and orientation of an individual cell in a built cellular structure dictates the macroscale or cellular morphologies [6]. Given any analysis scale, material morphology significantly influences the intrinsic and effective thermal, electrical, and thermoelectric properties. The primary focus of this research is to explore how macro and micro scale morphologies influence the effective transport mechanisms through advanced materials. The advanced materials have engineered properties created through the development of specialized processes and synthesis techniques. Typically, advanced materials are utilized in the high-

tech products such as spacecrafts, aircrafts, satellites, wearable techs, carbon nanofiber-based composites.

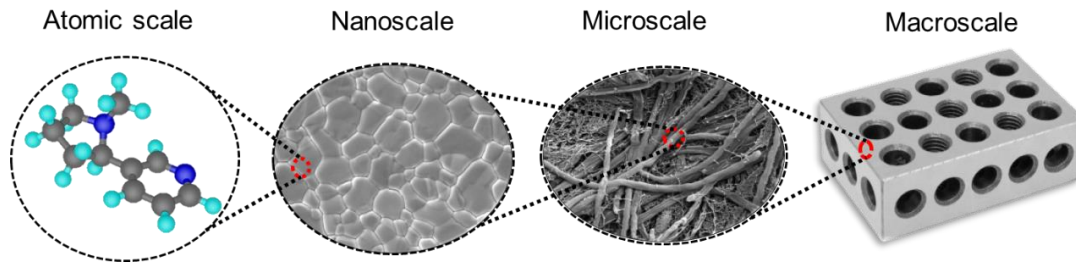


Figure 1.1. Material morphologies on various scales

1.2. Significance of Material Morphologies on Thermal Transport

In terms of thermal transport, a plethora of scientific literature is available focusing on morphological parameters impact on the thermal properties. One past research used analytical models to maximize heat transfer in aluminum honeycomb heat exchangers by optimizing the cell morphology such as cell orientation, cell wall thickness and cell size [6]. A previous experimental study fabricated L-shaped kinked polymer composite consisting of poly(vinylidene fluoride) and graphene nanoflake films (GNF) to improve directional thermal conductivity with anisotropic thermal conduction ratio greater than six [7]. The high directional thermal conduction was attributed to the two-dimensional planar shape of GNFs readily adaptable to the molten polymer flow, compared with highly entangled carbon nanotubes and three-dimensional graphite fillers. Another past research used numerical simulations to compare the thermal gradients in thermoelectric (TE) legs of various shapes [8]. The thermal gradients were found to be significantly higher in hollow

TE legs relative to filled legs, pointing towards strong potential of using interior voids and hierarchical geometries in TE generators for enhanced thermal resistance. One previous research carried out mesoscopic simulations for carbon nanotube (CNT)-polymer composites and observed that the CNT alignment to thermal gradient field provided up-to ~16-times enhancement in thermal conductivity [9].

The implication of morphological properties on thermal transport mechanism can be understood using Fourier's law of thermal conduction given in Eq. (1.1):

$$\frac{\partial Q}{\partial t} = -k \oint_s \nabla T \cdot dS \quad (1.1)$$

Where $\partial Q/\partial t$ is the amount of heat transferred per unit time, k is thermal conductivity of material, ∇T is temperature gradient across the medium and dS is an oriented surface area element. This law states that the rate of heat transfer through a material is proportional to the negative gradient in the temperature and to the area, at right angles to that gradient, through which the heat flows. The basis of Fourier's law stands on the assumption of constant thermal conductivity of material. This is particularly true for small temperature gradients; however, the proportionality no longer holds if the material is subject to large temperature gradients (i.e., the thermal conductivity of material is a function of temperature). For anisotropic materials, the thermal conductivity generally varies in different plane directions depending on lattice topology. Consequently, the spatial location and orientation of anisotropic material relative to applied thermal gradient is critical. In addition, the physical or chemical combination of two or more materials lead to range of thermal conductivities, depending on processing methods, filling materials volume fraction, and distribution structure of added materials. Taking into account all the

morphological parameters and composition properties, the resulting thermal conductivity is termed as effective thermal conductivity, k_e . By controlling the macroscale geometric parameters and nanoscale particulate morphologies, the effective thermal conductivity can either be improved for an effective thermal transport or deteriorated to augment the thermal resistance of the material.

1.3. Significance of Material Morphologies on Electrical Transport

The morphological parameters impact on electrical properties is widely explored in the scientific literature. One previous research theoretically investigated the effective electrical conductivity of metal-polymer composite as a function of morphological properties of metal particulates such as particle shape, size and the volume of loading [10]. The study demonstrated that the percolation threshold of metal-polymer composites decreases rapidly with increasing the metal particle axial ratio and decreasing the metal particle size. It was shown that the effective electrical conductivity increases rapidly with the increase of the metal particle axial ratio before it reaches the axial ratio threshold. A past study analyzed the carbon nanotube (CNT) morphology effect on the electrical transport through epoxy-CNT composite. The study demonstrated that the electrical conductivity of epoxy-CNT composites increased ~2.5 orders of magnitude when bias potential was parallel to the CNT alignment orientations [11]. In another previous similar experimental study, an electric field of 43.5 kV/m at frequency of 10 Hz was applied to align CNTs in a single wall CNT-polymer composite, resulting in 5 orders of magnitude increase in electrical conductivity [12]. For electrical transport, similar to Fourier's law of

heat conduction, Ohm's law describes the flow of electric charge in electrical conductors subjected to the potential difference. The continuum mathematical form of Ohm's law is given in Eq. (1.2):

$$\mathbf{E} = \rho \mathbf{J} \quad (1.2)$$

$$\rho = RA_c/L \quad (1.3)$$

where \mathbf{J} is the current density at a given location in a material, \mathbf{E} is the electric field at that location and ρ is a material dependent parameter called the electrical resistivity. It states that the current density at any location within a conductor is proportional to the electrical field strength at location. The basis of Ohm's law also uses fundamental assumption that the material resistivity remains constant at any location within the resistive material. However, like thermal conductivity, the electrical conductivity (inverse of electrical resistivity) also varies with large temperature gradient and lattice morphology in anisotropic materials. The empirical relation of electrical resistivity, ρ , is given in Eq. (1.3), in which R is the electrical resistance, L is the length, A_c is cross-sectional area of the conductor. By controlling the geometrical parameters along with the distribution and orientation of constituent, the effective resistivity of the material can be enhanced or degraded depending on the application requirements.

1.4. Significance of Material Morphologies on Thermoelectric Properties

The thermoelectric properties of thermoelectric materials are characterized by figure of merit (ZT), given as:

$$ZT = S^2 \sigma T / k \quad (1.4)$$

where S is seebeck coefficient, σ is electrical conductivity, k is thermal conductivity and T is the absolute temperature at which ZT is measured. The key phenomenon to generate thermoelectric effect is Seebeck effect, where electricity generates due to temperature differences. The Seebeck coefficient is an intrinsic property of the materials related to their electronic properties and independent of geometric parameters. A typical thermoelectric material should have high electrical conductivity and low thermal conductivity to maintain large temperature gradient. Thus far, to achieve an efficient TE energy conversion, considerable efforts have been devoted toward the development of efficient TE materials [13–15]. In addition to the development of materials, the module structural design, especially the geometrical design of TE legs, is another essential factor in the efficiencies, durability, and cost of thermoelectric generators (TEGs). Numerous numerical simulations have demonstrated the remarkable effect of the three-dimensional (3D) geometries of TE legs on the energy conversion efficiency in a module and proposed various new designs of structures of TE legs that aim to enhance the efficiency [16–19].

1.5. Research Objectives

The manufacturing limitations pose a major challenge in achieving better material morphologies in advanced materials. Figure 1.2 shows an abstract comparison between different material categories with manufacturing difficulty and resource dependence with property-to-cost ratio. The process of converting traditional materials to advanced ones involve several material tailoring techniques to improve functionality by controlling morphologies in plainfield and composite materials. However, controlling material

morphologies has been extremely challenging which inhibits the practical realization of advanced materials. With recent advancements in fabrication techniques and additive manufacturing, there is an opportunity for practical realization of advanced materials with superior physical and chemical properties to other competitive materials. There is a need of developing design methods to provide insight into morphology control recommendations for enhanced thermal, electrical and thermoelectric properties.

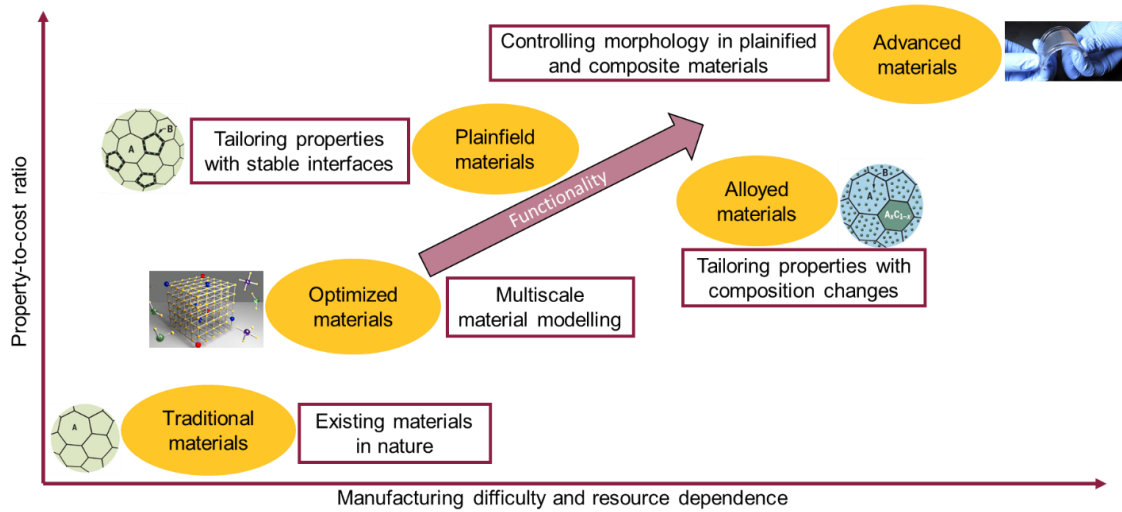


Figure 1.2. Various material categories compared to manufacturing difficulty and resource dependence to property-to-cost ratio

From vast available advanced materials, this research focuses on thermoelectric materials and copper-carbon nanotube (Cu-CNT) composites for studying the influence of macroscale and microscale morphologies for transport properties. The primary objective and contributions to this research are:

1. Develop finite element model (FEM) for 3D printable thermoelectric legs along with 3D printable compositionally segmented legs (chapter 2 and 3).
2. Develop FEM for predicting electrical and thermal conductivities in Cu-CNT composites for stochastic CNT distributions and range of interfacial resistances (chapter 4).
3. Develop data-driven models for rapid approximation of electrical and thermal conductivities in CNT based composites (chapter 5).
4. Develop FEM for predicting the electrical and thermal conductivity in CNT fibers by considering the CNT-CNT interfacial resistance, void distributions, and large CNT aspect ratios (chapter 6).

For chapter 2 and 3, our FEM helped the researchers to establish comparison to the experimental findings which validated the proposed ideas. All of the chapters are collectively and directly linked to analyze the effect of morphology control on thermal, electrical, and thermoelectric properties of advanced materials and make quantitative recommendations towards superior properties.

2. ENERGY CONVERSION MODELING IN 3D PRINTABLE THERMOELECTRIC CELLULAR ARCHITECTURES

2.1. Abstract

Thermoelectric power generation offers a promising way to recover waste heat. The geometrical design of thermoelectric legs in modules is important to ensure sustainable power generation but cannot be easily achieved by traditional fabrication processes. Herein, we propose the design of cellular thermoelectric architectures for efficient and durable power generation, realized by the extrusion-based 3D printing process of Cu_2Se thermoelectric materials. We design the optimum aspect ratio of a cuboid thermoelectric leg to maximize the power output and extend this design to the mechanically stiff cellular architectures of hollow hexagonal column- and honeycomb-based thermoelectric legs. Moreover, we develop organic binder-free Cu_2Se -based 3D-printing inks with desirable viscoelasticity, tailored with an additive of inorganic Se_8^{2-} polyanion, fabricating the designed topologies. The computational simulation and experimental measurement demonstrate the superior power output and mechanical stiffness of the proposed cellular thermoelectric architectures to other designs, unveiling the importance of topological designs of thermoelectric legs toward higher power and longer durability.

2.2. Introduction

With the rapid increase in global energy consumption, the world is facing serious energy and environmental crises as a result of fossil fuel depletion and environmental pollution, critically requiring sustainable and renewable energy sources. Among the

various types of renewable energy sources, thermal energy is omnipresent in natural and artificial environments, but more than 60% is dissipated. Thermoelectric (TE) power generation has been regarded as a reliable and durable way to recover dissipated waste heat, as it enables the direct conversion of heat to electricity without any environmental pollution [20–24]. Thus far, to achieve an efficient TE energy conversion, considerable efforts have been devoted toward the development of efficient TE materials, including traditional Bi_2Te_3 [25–28], PbTe [14], and SiGe -based [13] alloys and emerging materials of liquid-like materials [29–32], skutterudites [33], half-Heuslers [34], SnSe [35,36], MgSb -based materials [37], etc. [38–40]. Among them, liquid-like TE materials within the “phonon-glass electroncrystal” concept have attracted tremendous attention due to their high efficiencies arising from ultralow thermal conductivities at high temperatures. Such unusual properties originate from their structural characteristics in which one immobile ion forms a rigid sublattice framework for the free transport of electrons, whereas other mobile ions are comprised of liquid-like sublattice to interrupt the thermal transports. Moreover, Cu_2Se - or $\text{Cu}_{1.97}\text{S}$ -based compounds representing this class of materials have nontoxic and earth-abundant elements, which significantly reduce the cost by at least one order of magnitude compared with state-of-the-art TE materials [29–31]. In addition to the development of materials, the module structural design, especially the geometrical design of TE legs, is another essential factor in the efficiencies, durability, and cost of thermoelectric generators (TEGs).

2.3. Problem Statement and Background Review

Numerous numerical simulations have demonstrated the remarkable effect of the 3D geometries of TE legs on the energy conversion efficiency in a module and proposed various new designs of structures of TE legs that aim to enhance the efficiency [16–19,41]. However, most studies have focused only on efficiency maximization, neglecting the mechanical durability and cost, despite their actual importance. Moreover, experimental research on the geometrical design of TE legs remains in the early stages in that the basic geometrical parameters, such as the aspect ratio or cross-sectional area ratio of stereotypical cuboid-shaped TE legs, have been investigated [42,43]. This geometrical limitation of TE legs may originate from the conventional process of the top-down dicing of TE ingots to produce TE legs, where there is no choice of shapes in a TE leg other than a cuboid.

Nature-inspired architected cellular materials are an emerging class of materials with high stiffness, controllable heat dissipation and transfer, and light weightness, which allow potential applications in highly stiff panels, energy absorbers, heat exchangers, vibration damping, and catalysts [44,45]. Cellular materials generally consist of an interconnected network of solid structures formed by cell walls separated by periodic or stochastic pores. The shape and layout of pores are critical to the mechanical properties of the cellular materials, since they determine the effective density and deformation modes. For example, in stochastic open-cell structures, structural Young's modulus decreases with density as an empirical power law with an exponent of two to three. However, in periodic closed cellular structures such as honeycomb architecture, both the mechanical strength

and stiffness linearly decrease with the relative density [44,46]. Thus, the closed-cellular structures tend to exhibit greater mechanical performance than open-cellular structures when their densities are reduced in a similar amount [47]. Honeycombs represent the 2D closed-cellular architectures used almost exclusively today due to their relatively simple structures and excellent mechanical properties, such as high in-plane compression and out-of-plane shear properties. When compared with triangular and hexagonal truss-structured materials with similar densities, optimally designed honeycombs exhibited multi-fold enhancement in compressive strength. The honeycomb architecture resisted buckling upon compression unlike the truss-based counterparts [48]. Recently, the specific stiffnesses of ceramic hexagonal and triangular honeycombs were reported as $>10^7 \text{ Pa kg}^{-1}\text{m}^{-3}$ that surpass other micro and nanoscale lattices of similar relative densities [49]. The 3D printing process has been recognized as an advanced technology for directly producing such 3D cellular architectures with great geometrical complexity in a cost-effective manner [50,51]. However, the complex 3D geometries of TE materials and modules have never been realized so far because the full functionality of 3D printing technology has yet not been applied to TE technology, though many approaches based on stereolithography, extrusion-based printing, and selective laser sintering have been reported to produce TE materials [52–57]. Moreover, in most reports, 3D-printable materials have still been limited to Bi_2Te_3 -based materials, requiring the expansion of available materials operatable at high temperatures for the widespread applications of this technology [53–56,58].

Here, we designed the cellular honeycomb topology of Cu_2Se TE legs by the 3D finite element models (FEMs) for higher power generating performances and stronger

mechanical stiffness than a typical cuboid. To fabricate the designed topology, we developed the extrusion-based 3D printing process of Cu_2Se TE materials. The extrusion-based 3D printing process has been extensively studied for the production of inorganic 3D objects using concentrated colloid inks. In this process, colloid inks containing semiconductor metal chalcogenides must have the desired rheological properties to ensure 3D printability. To this end, we designed the Cu_2Se colloid ink to have particles with surface charges, achieved by the addition of Se_{82}^- polyanion, showing significantly improved printability. Moreover, Se_{82}^- polyanion acts as a sintering promoting aid, which leads to the liquid-phase sintering of Cu_2Se particles to shape and scale robust Cu_2Se materials with the competitive ZT value of 1.2 at 1000 K by the 3D printing process. The fabrication and characterization of the power-generating modules chipped with a cuboid, a hollow hexagonal column, and a honeycomb showed the highest power performance of a honeycomb-architected TE leg, demonstrating the feasibility of our nature-inspired design toward the fabrication of efficient and durable TEGs.

2.4. Finite Element Model

To design the topology of Cu_2Se TE legs toward higher power generating performance as well as mechanical durability, we developed a 3D FEM to calculate P , ΔT , and electrical resistance of a TEG (Fig. 2.1(a–d)). Generally, the major geometrical control parameter of a TE leg is an aspect ratio in a cuboid since the aspect ratio dependence on the output power has the trade-off relation between a module resistance and a temperature difference (ΔT) across a TE leg [42,43,59]. Accordingly, we define the aspect ratio as the

ratio of the leg length (l) to cross-sectional area (A) (Fig. 2.1(a)). In this computation, we used the TE properties of the 3D-printed Cu_2Se TE materials. The detailed TE properties are discussed in the following sections. Based on the 3D FEM, a Cu_2Se cuboid TE leg is expected to produce the maximum P near l/A of 1.5 at a various hot-side temperatures ranging from 700 to 850 K (Fig. 2.1(b)). The optimum l/A results from the characteristic dependence of ΔT and resistance on l/A . If l/A varies from 0.5 to 10, ΔT increases in a loglinear manner while the electrical resistance increases linearly with l/A . In addition to the power output, the topology control of a TE leg can be beneficial to enhance the mechanical strength, which is critical for the practical use of TEGs. In a real-world application, TE legs in a TEG are forced to experience various mechanical stresses such as compressive or tensile stresses because of materials' thermal expansion or shear, torsion, and bending stresses arising from external environments. However, despite its actual importance, the module design for mechanical durability has been largely neglected so far. In this study, we propose a cellular honeycomb architecture to improve the mechanical durability of a TE leg. Honeycomb structures have been known to exhibit high strength to weight ratio, which comes from the efficient dispersion of external forces, particularly in the out-of-plane load. Further, the in-plane compressive strength can be optimized by controlling the ratio between wall thickness and the unit-cell size. Considering our printing capability, we consider a cuboid, a hollow hexagonal column, which is a basic unit to build a honeycomb architecture, and a honeycomb comprising of seven hexagonal columns (Fig. 2.1(c–g)). Figure 1(c, d) show the cross-sectional areas of the cellular architectures. In our design, hexagon length is 2.5 mm, wall thickness is 0.33 mm, and the inclination angle is

30°. The cross-sectional area is 4 mm² for the hexagonal column and 105.21 mm² for the honeycomb, resulting in an aspect ratio of 1.5 for the hexagonal column and 0.06 for the honeycomb. The leg length of all TEGs in this work is 6 mm. We hypothesize that the optimum aspect ratio is similar for both hexagonal column and cuboid TE legs, since the aspect ratio is a key factor for both thermal and electrical resistances. To accurately optimize the aspect ratio, the electrical and thermal contact resistances at TE leg-electrode interface need to be considered. When electrical current or heat transfers from the TE leg to an electrode, the cross-sectional shape of the TE leg affects how the current or heat spreads into the electrode [60]. Furthermore, solder properties may be influenced by the TE leg thickness, if the TE leg is not sufficiently thick. If empirical correlations between the TE leg geometry and contact resistances are available for the cellular or other architectures, the topology of the 3D TE module will be more accurately determined. For the honeycomb architecture, we select a relatively small aspect ratio, because it is challenging to achieve the optimum l/A in the actual device, as fabricating high-aspect-ratio, multiple hexagonal columns are not feasible yet.

hexagonal column-, and (d) honeycomb-shaped Cu₂Se TE legs. e–g Simulated heat flux distribution in the cold side of (e) cuboid-, (f) hollow hexagonal column-, and (g) honeycomb-shaped Cu₂Se TE legs when the hot side temperature is 873 K. (h) Compressive stiffness-density Ashby plot showing the cellular Cu₂Se materials described in this paper compared with other materials. (I) Generation efficiencies of Cu₂Se TE legs at the hot side temperatures ranging from 323 to 873 K.

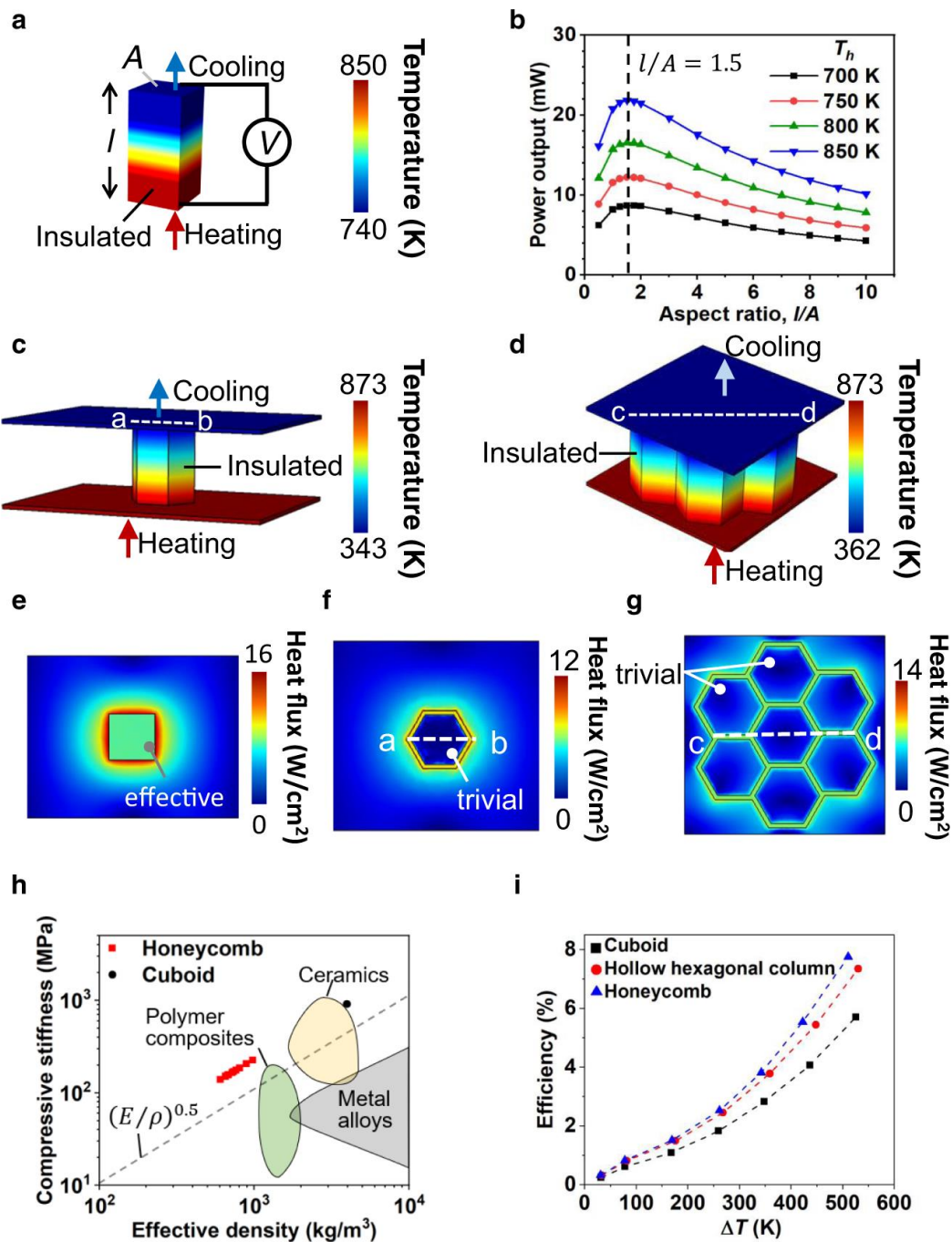


Figure 2.1. Design of Cu₂Se TE cellular architectures. (a) Simulated temperature distributions in cuboid-, -shaped Cu₂Se TE legs. (b) Output power of cuboid shaped Cu₂Se TE leg as a function of aspect ratio. c, d Simulated temperature distributions in (c) hollow

2.5. FEM Results and Discussion

The mechanical properties of the 3D-printed Cu_2Se were measured by compressive test under the uniaxial compression mode on a cuboid and a honeycomb. The stress-strain curve of the 3D-printed honeycomb in the elastic region exhibits similar behaviour to that of the cuboid. The calculated modulus 939 MPa, which was almost identical to 911 MPa of the cuboid. Interestingly, the honeycomb exhibited a larger plastic deformation region and higher fracture strain by three times, compared with the cuboid. This improvement may originate from unique structural characteristics of the honeycomb, which can distribute the stress concentration into a whole structure [61–63]. Sun et al. [63] demonstrated the distribution of the stress concentration in honeycomb architectures by the FEM simulations and experiments. Based on the measured properties, we predicted the compressive stiffness of the Cu_2Se honeycomb architecture using the Ashby-Gibson relation (Fig. 2.1(h)). As the number of unit cell in the honeycomb architecture increases, effective compressive stiffness decreases in the range of 100–200 MPa due to the decrease in density (ρ), agreeing with the measured value of 174.7 MPa in the honeycomb with the effective cross-sectional area including pores. The effective density of the Cu_2Se honeycomb architecture is merely 600–1000 kg m^{-3} . Compared with other common materials with a density near 1000 kg m^{-3} , the Cu_2Se honeycomb architecture exhibits a superior property. Other materials with high specific stiffness follow $(E/\rho)^{0.5}$ line in the Ashby E - ρ plot. However, the honeycomb architecture shows the specific stiffness of $198\text{kPa m}^3 \text{ kg}^{-1}$ that is greater than $(E/\rho)^{0.5}$ by a factor of 2. The honeycomb architectures take <25% density of the traditional cuboid architecture, making it lightweight and stiff

inorganic TE materials. Thus, for mobility applications and for large-scale energy harvesting systems, the hexagonal architecture can be considered useful due to its excellent strength-weight ratio.

In addition to the mechanical properties, the simulation results showed that the proposed cellular architectures could enhance the power generation efficiency, compared with a cuboid. With 3D FEM, we compared three different topologies including a cuboid, a hollow hexagonal column, and a honeycomb. The generation efficiency is defined as the ratio of power output to heat input. A hexagonal column and honeycomb architectures are expected to exhibit 7.3% and 7.7% efficiency when the hot-side temperature is 873 K that are 22 and 26% greater than the efficiency of traditional cuboids (Fig. 2.1(i)). Under similar ΔT , both the hexagonal column and cuboid TEGs with an equal aspect ratio produce analogous potential distributions (Fig. 2.1(a, c, and d)). However, compared with a cuboid module, in hexagonal and honeycomb modules, less amount of heat is required to achieve the same ΔT than the cuboid module due to less effective heat spread in the electrodes. In the hexagonal module, the TE legs contact electrodes over a large region enclosing an area of 16.24 mm². As seen in the simulated heat flux distribution (Fig. 2.1(e–g)), the steady-state heat flux is predicted as trivial within the enclosed area on the cold side of the hexagonal and honeycomb modules because the electrode temperature is maintained uniform (Fig. 2.1(e)). The uniform temperature within the enclosed region strongly suppresses in-plane heat flow within the electrode. However, the cuboid module efficiently spreads heat from the electrode center to outward radially, leading to reduced TE leg-electrode interface thermal resistance. The inefficient heat spreads in electrodes cause the

hexagonal and honeycomb modules to achieve a large generation efficiency. Interestingly, the efficiency slightly increases when the honeycomb module scales up.

2.6. Comparison to Experimental Samples

Figure 2.2 shows the apparatus cartoon which was used to fabricate complex TE architectures with Cu_2Se ink with Se polyanion as sintering binder.

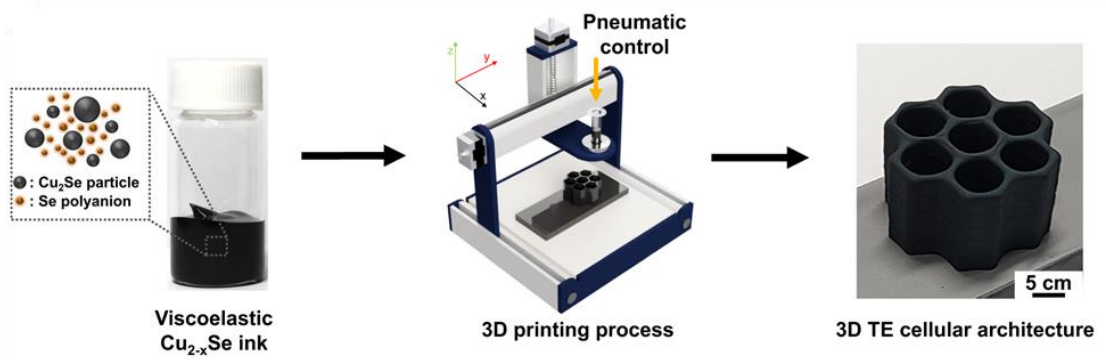


Figure 2.2: Scheme for 3D printing process of the Cu_2Se -based honeycomb cellular architecture by using all inorganic Cu_{2-x}Se ink.

To validate our designs of nature-inspired cellular architectures, we prepared three different TE legs of a cuboid, a hollow hexagonal column, and a honeycomb and fabricated the p-type single leg power generators by the 3D printing process (Fig. 2.3(a–c)). Recently, a few studies have been reported on n-type semiconductors of ternary or quaternary copper chalcogenide compounds of CuAgSe [64], CuFeS_2 , and $\text{Cu}_{1-x}\text{Zn}_x\text{FeS}_2$ [65]. However, the ZT values of these materials are <0.6 at the highest, not high enough to use them as an n-type pair of our Cu_2Se . As alternatives, different classes of n-type TE semiconductors such

as doped SnSe, skutterudites, half-Heusler can be potential candidates as an n-type cellular pair of our 3Dprinted Cu₂Se. The top and bottom of the 3D-printed Cu₂Se TE legs were metallized with Ni layers through sputtering, subsequently attaching to Cu electrodes using an Ag paste as a solder. For a reliable measurement, the area ratios of the cold-side Cu electrodes/ TE legs were equalized for all modules to ensure an equivalent cooling rate. Also, we set the identical hot-side temperatures for the measurement of the power-generating performances of these modules by heating the top of the modules with a ceramic heater. The cold side was cooled at the bottom with a water-circulating cooler under the same water flow rate and water temperature. Upon heating, all modules showed almost linear increases in the output voltages and quadratic increases in the output power, demonstrating the reliability of the measurement (Fig. 2.3(d–f)). Moreover, the measured electrical output values and of the TEGs are in line with the simulation results (Fig. 2.3(g)). This agreement suggests that the simulated models (Fig. 2.1(i)), that predicted higher efficiencies of the hexagonal- and honeycomb modules than that of the cuboid module, were well realized in the 3D printed modules.

In addition, the honeycomb-based module showed a significantly larger power than those of the other modules (Fig. 2.3(g)), which can be understood by a lower module resistance due to its larger cross-sectional area by approximately five times. This larger cross section is beneficial in the reduction of the contact resistance at TE legs and electrodes. The calculated contact resistances of the modules from the material properties were the lowest at the honeycomb among all the modules. Accordingly, the honeycomb exhibited the highest power density of 621.40 mW cm⁻² among the three topologies (Fig.

2.3(h)). These power generating performances validate our topology designs and demonstrates feasibility of the proposed strategy of the topological designs of TE legs for enhancing power performance and mechanical durability.

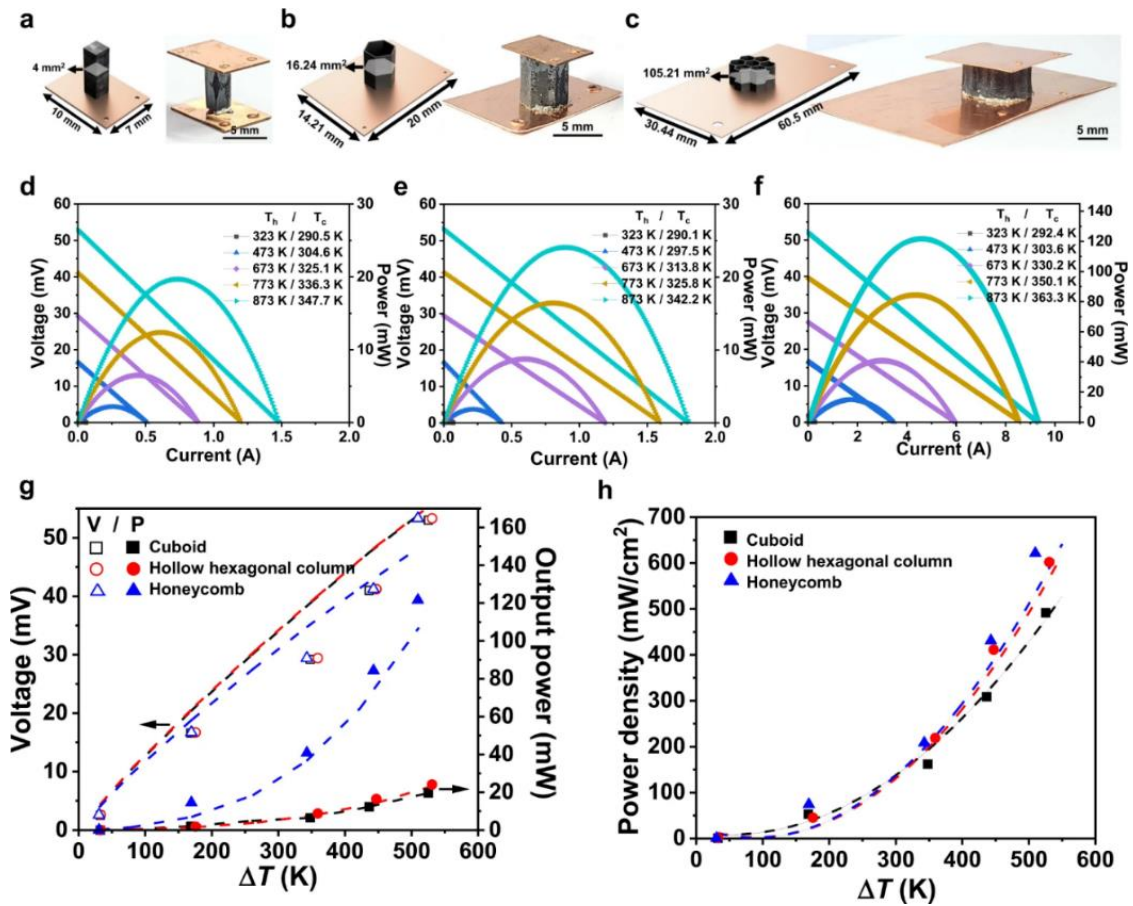


Figure 2.3: (a–c) 3D illustrated models and photograph of TEGs chipped with (a) cuboid-, (b) hollow hexagonal column-, and (c) honeycomb-shaped Cu_2Se TE legs. (d–f) Output voltages and powers of (d) cuboid-, (e) hollow hexagonal column-, and (f) honeycomb-shaped Cu_2Se TE legs at the hot side temperatures ranging from 323 to 873 K. (g) Output voltages and powers, and (h) power densities of TEGs as a function of the temperature

differences. The points and the dotted lines in the panels of (g) and (h) are the measured values and the predicted values by the FEM simulation.

2.7. Conclusions

In summary, we have demonstrated the applicability of 3D printed cellular architectures of Cu₂Se-based TE materials for designing efficient and durable TEGs. We developed the 3D FEMs for cuboid, hollow hexagonal column, and cellular honeycomb structures that allowed us to comparatively design the topology of TE legs with perspectives of higher output power and mechanical strength. Moreover, we developed all-inorganic Cu₂Se TE inks with tailored rheological properties by the electro viscous effect of Se₈²⁻ polyanions. These inks allowed the building of complex 3D architectures of Cu₂Se TE materials that exhibit a peak ZT value of 1.21 at 1000 K. The experimental measurements of the fabricated TEGs chipped with the 3D-printed TE legs showed good agreement with the predicted power-generating performances, in which the honeycomb TE architecture with the highest predicted mechanical stiffness exhibited superior power density to typical cuboid TE legs. Undoubtedly, higher power generation performance can be obtained in the future using TE materials with higher ZT values. In addition to improving material properties, this study shows another system-level design to enhance the power-generating performance and durability in TE modules through the topological design of TE legs, which will accelerate the application of TE power generators to prevalent fields.

2.8. References

- [20] Bell, L. E., 2008, “Cooling, Heating, Generating Power, and Recovering Waste Heat with Thermoelectric Systems,” *Science* (80-.), **321**(5895), pp. 1457–1461.
- [21] Disalvo, F. J., 1999, “Thermoelectric Cooling and Power Generation,” *Science* (80-.), **285**(5428), pp. 703–706.
- [22] He, J., and Tritt, T. M., 2017, “Advances in Thermoelectric Materials Research: Looking Back and Moving Forward,” *Science* (80-.), **357**(6358), p. eaak9997.
- [23] Snyder, G. J., and Toberer, E. S., 2008, “Complex Thermoelectric Materials,” *Nat. Mater.*, **7**(2), pp. 105–114.
- [24] Zhang, Y., Cleary, M., Wang, X., Kempf, N., Schoensee, L., Yang, J., Joshi, G., and Meda, L., 2015, “High-Temperature and High-Power-Density Nanostructured Thermoelectric Generator for Automotive Waste Heat Recovery,” *Energy Convers. Manag.*, **105**, pp. 946–950.
- [25] Jo, S., Park, S. H., Ban, H. W., Gu, D. H., Kim, B. S., Son, J. H., Hong, H. K., Lee, Z., Han, H. S., Jo, W., Lee, J. E., and Son, J. S., 2016, “Simultaneous Improvement in Electrical and Thermal Properties of Interface-Engineered BiSbTe Nanostructured Thermoelectric Materials,” *J. Alloy. Comp.*, **689**, pp. 899–907.
- [26] Jo, S., Park, S. H., Shin, H., Oh, I., Heo, S. H., Ban, H. W., Jeong, H., Kim, F., Choo, S., Gu, D. H., Baek, S., Cho, S., Kim, J. S., Kim, B. S., Lee, J. E., Song, S., Yoo, J. W., Song, J. Y., and Son, J. S., 2019, “Soluble Telluride-Based Molecular Precursor for Solution-Processed High-Performance Thermoelectrics,” *ACS Appl. Energy Mater.*, **2**(7), pp. 4582–4589.
- [27] Kim, S. Il, Lee, K. H., Mun, H. A., Kim, H. S., Hwang, S. W., Roh, J. W., Yang, D. J., Shin, W. H., Li, X. S., Lee, Y. H., Snyder, G. J., and Kim, S. W., 2015, “Dense Dislocation Arrays Embedded in Grain Boundaries for High-Performance Bulk Thermoelectrics,” *Science* (80-.), **348**(6230), pp. 109–114.
- [28] Zheng, G., Su, X., Xie, H., Shu, Y., Liang, T., She, X., Liu, W., Yan, Y., Zhang, Q., Uher, C., Kanatzidis, M. G., and Tang, X., 2017, “High Thermoelectric Performance of P-BiSbTe Compounds Prepared by Ultra-Fast Thermally Induced Reaction,” *Energy Environ. Sci.*, **10**(12), pp. 2638–2652.
- [29] Liu, H., Shi, X., Xu, F., Zhang, L., Zhang, W., Chen, L., Li, Q., Uher, C., Day, T., and Snyder Jeffrey, G., 2012, “Copper Ion Liquid-like Thermoelectrics,” *Nat. Mater.*, **11**(5), pp. 422–425.
- [30] Liu, W. Di, Yang, L., Chen, Z. G., and Zou, J., 2020, “Promising and Eco-Friendly Cu₂X-Based Thermoelectric Materials: Progress and Applications,” *Adv. Mater.*, **32**(8), p. e1905703.

- [31] Wei, T. R., Qin, Y., Deng, T., Song, Q., Jiang, B., Liu, R., Qiu, P., Shi, X., and Chen, L., 2018, “Copper Chalcogenide Thermoelectric Materials,” *Sci. China Mater.*, **62**(1), pp. 8–24.
- [32] Zhao, K., Qiu, P., Shi, X., and Chen, L., 2019, “Recent Advances in Liquid-like Thermoelectric Materials,” *Adv. Funct. Mater.*, **30**(8), p. 1903867.
- [33] Zong, P. A., Hanus, R., Dylla, M., Tang, Y., Liao, J., Zhang, Q., Snyder, G. J., and Chen, L., 2017, “Skutterudite with Graphene-Modified Grain-Boundary Complexion Enhances ZT Enabling High-Efficiency Thermoelectric Device,” *Energy Environ. Sci.*, **10**(1), pp. 183–191.
- [34] Xing, Y., Liu, R., Liao, J., Zhang, Q., Xia, X., Wang, C., Huang, H., Chu, J., Gu, M., Zhu, T., Zhu, C., Xu, F., Yao, D., Zeng, Y., Bai, S., Uher, C., and Chen, L., 2019, “High-Efficiency Half-Heusler Thermoelectric Modules Enabled by Self-Propagating Synthesis and Topologic Structure Optimization,” *Energy Environ. Sci.*, **12**(11), pp. 3390–3399.
- [35] Heo, S. H., Jo, S., Kim, H. S., Choi, G., Song, J. Y., Kang, J. Y., Park, N. J., Ban, H. W., Kim, F., Jeong, H., Jung, J., Jang, J., Lee, W. B., Shin, H., and Son, J. S., 2019, “Composition Change-Driven Texturing and Doping in Solution-Processed SnSe Thermoelectric Thin Films,” *Nat. Commun.*, **10**(1).
- [36] Zhao, L. D., Lo, S. H., Zhang, Y., Sun, H., Tan, G., Uher, C., Wolverton, C., Dravid, V. P., and Kanatzidis, M. G., 2014, “Ultralow Thermal Conductivity and High Thermoelectric Figure of Merit in SnSe Crystals,” *Nature*, **508**(7496), pp. 373–377.
- [37] Kraemer, D., Sui, J., McEnaney, K., Zhao, H., Jie, Q., Ren, Z. F., and Chen, G., 2015, “High Thermoelectric Conversion Efficiency of MgAgSb-Based Material with Hot-Pressed Contacts,” *Energy Environ. Sci.*, **8**(4), pp. 1299–1308.
- [38] Choi, J., Jung, Y., Yang, S. J., Oh, J. Y., Oh, J., Jo, K., Son, J. G., Moon, S. E., Park, C. R., and Kim, H., 2017, “Flexible and Robust Thermoelectric Generators Based on All-Carbon Nanotube Yarn without Metal Electrodes,” *ACS Nano*, **11**(8), pp. 7608–7614.
- [39] Gu, D. H., Jo, S., Jeong, H., Ban, H. W., Park, S. H., Heo, S. H., Kim, F., Jang, J. I., Lee, J. E., and Son, J. S., 2017, “Colloidal Synthesis of Te-Doped Bi Nanoparticles: Low-Temperature Charge Transport and Thermoelectric Properties,” *ACS Appl. Mater. Interfaces*, **9**(22), pp. 19143–19151.
- [40] Kim, J., Bae, E. J., Kang, Y. H., Lee, C., and Cho, S. Y., 2020, “Elastic Thermoelectric Sponge for Pressure-Induced Enhancement of Power Generation,” *Nano Energy*, **74**, p. 104824.
- [41] Ferreira-Teixeira, S., and Pereira, A. M., 2018, “Geometrical Optimization of a Thermoelectric Device: Numerical Simulations,” *Energy Convers. Manag.*, **169**,

pp. 217–227.

- [42] Xing, T., Song, Q., Qiu, P., Zhang, Q., Gu, M., Xia, X., Liao, J., Shi, X., and Chen, L., 2021, “High Efficiency GeTe-Based Materials and Modules for Thermoelectric Power Generation,” *Energy Environ. Sci.*, **14**(2), pp. 995–1003.
- [43] Qiu, P., Mao, T., Huang, Z., Xia, X., Liao, J., Agne, M. T., Gu, M., Zhang, Q., Ren, D., Bai, S., Shi, X., Snyder, G. J., and Chen, L., 2019, “High-Efficiency and Stable Thermoelectric Module Based on Liquid-like Materials,” *Joule*, **3**(6), pp. 1538–1548.
- [44] Yeo, S. J., Oh, M. J., and Yoo, P. J., 2019, “Structurally Controlled Cellular Architectures for High Performance Ultra Lightweight Materials,” *Adv. Mater.*, **31**(34), p. 1803670.
- [45] Tian, X., and Zhou, K., 2020, “3D Printing of Cellular Materials for Advanced Electrochemical Energy Storage and Conversion,” *Nanoscale*, **12**(14), pp. 7416–7432.
- [46] Schaedler, T. A., Jacobsen, A. J., Torrents, A., Sorensen, A. E., Lian, J., Greer, J. R., Valdevit, L., and Carter, W. B., 2011, “Ultralight Metallic Microlattices,” *Science* (80-.), **334**(6058), pp. 962–965.
- [47] Berger, J. B., Wadley, H. N. G., and McMeeking, R. M., 2017, “Mechanical Metamaterials at the Theoretical Limit of Isotropic Elastic Stiffness,” *Nature*, **543**(7646), pp. 533–537.
- [48] Bauer, J., Hengsbach, S., Tesari, I., Schwaiger, R., and Kraft, O., 2014, “High-Strength Cellular Ceramic Composites with 3D Microarchitecture,” *Proc. Natl Acad. Sci. USA*, **111**(7), pp. 2453–2458.
- [49] Muth, J. T., Dixon, P. G., Woish, L., Gibson, L. J., and Lewis, J. A., 2017, “Architected Cellular Ceramics with Tailored Stiffness via Direct Foam Writing,” *Proc. Natl Acad. Sci. USA*, **114**(8), pp. 1832–1837.
- [50] Lewis, J. A., and Ahn, B. Y., 2015, “Three-Dimensional Printed Electronics,” *Nature*, **518**(7537), pp. 42–43.
- [51] Sun, K., Wei, T. S., Ahn, B. Y., Seo, J. Y., Dillon, S. J., and Lewis, J. A., 2013, “3D Printing of Interdigitated Li-Ion Microbattery Architectures,” *Adv. Mater.*, **25**(33), pp. 4539–4543.
- [52] He, M., Zhao, Y., Wang, B., Xi, Q., Zhou, J., and Liang, Z., 2015, “3D Printing Fabrication of Amorphous Thermoelectric Materials with Ultralow Thermal Conductivity,” *Small*, **11**(44), pp. 5889–5894.
- [53] Qiu, J., Yan, Y., Luo, T., Tang, K., Yao, L., Zhang, J., Zhang, M., Su, X., Tan, G., Xie, H., Kanatzidis, M. G., Uher, C., and Tang, X., 2019, “3D Printing of Highly Textured Bulk Thermoelectric Materials: Mechanically Robust BiSbTe Alloys

- with Superior Performance,” *Energy Environ. Sci.*, **12**(10), pp. 3106–3117.
- [54] Du, Y., Chen, J., Meng, Q., Xu, J., Paul, B., and Eklund, P., 2020, “Flexible Ternary Carbon Black/Bi₂Te₃ Based Alloy/Poly(lactic Acid) Thermoelectric Composites Fabricated by Additive Manufacturing,” *J. Mater.*, **6**(2), pp. 293–299.
- [55] Oztan, C., Ballikaya, S., Ozgun, U., Karkkainen, R., and Celik, E., 2019, “Additive Manufacturing of Thermoelectric Materials via Fused Filament Fabrication,” *Appl. Mater. Today*, **15**, pp. 77–82.
- [56] Jo, S., Choo, S., Kim, F., Heo, S. H., and Son, J. S., 2019, “Ink Processing for Thermoelectric Materials and Power-Generating Devices,” *Adv. Mater.*, **31**(20), p. e1804930.
- [57] Aw, Y. Y., Yeoh, C. K., Idris, M. A., Teh, P. L., Hamzah, K. A., and Sazali, S. A., 2018, “Effect of Printing Parameters on Tensile, Dynamic Mechanical, and Thermoelectric Properties of FDM 3D Printed CABS/ZnO Composites,” *Materials (Basel)*, **11**(4), p. 466.
- [58] Su, N., Zhu, P., Pan, Y., Li, F., and Li, B., 2020, “3D-Printing of Shape-Controllable Thermoelectric Devices with Enhanced Output Performance,” *Energy*, **195**, p. 116892.
- [59] Yazawa, K., and Shakouri, A., 2017, “Optimization of Power and Efficiency of Thermoelectric Devices with Asymmetric Thermal Contacts,” *J. Appl. Phys.*, **111**(2), p. 024509.
- [60] Roh, I. J., Lee, Y. G., Kang, M. S., Lee, J. U., Baek, S. H., Kim, S. K., Ju, B. K., Hyun, D. Bin, Kim, J. S., and Kwon, B., 2016, “Harman Measurements for Thermoelectric Materials and Modules under Non-Adiabatic Conditions,” *Sci. Rep.*, **6**.
- [61] Meo, M., Morris, A. J., Vignjevic, R., and Marengo, G., 2003, “Numerical Simulations of Low-Velocity Impact on an Aircraft Sandwich Panel,” *Compos. Struct.*, **62**(3–4), pp. 3–4.
- [62] Lu, C., Zhao, M., Jie, L., Wang, J., Gao, Y., Cui, X., and Chen, P., 2015, “Stress Distribution on Composite Honeycomb Sandwich Structure Suffered from Bending Load,” *Procedia Eng.*, **99**, pp. 405–412.
- [63] Sun, G., Huo, X., Chen, D., and Li, Q., 2017, “Experimental and Numerical Study on Honeycomb Sandwich Panels under Bending and In-Panel Compression,” *Mater. Des.*, **133**, pp. 154–168.
- [64] Wang, X., Qiu, P., Zhang, T., Ren, D., Wu, L., Shi, X., Yang, J., and Chen, L., 2015, “Compound Defects and Thermoelectric Properties in Ternary CuAgSe-Based Materials,” *J. Mater. Chem. A*, **3**(26), pp. 13662–13670.

[65] Xie, H., 2008, "The Role of Zn in Chalcopyrite CuFeS₂: Enhanced Thermoelectric Properties of Cu_{1-x}Zn_xFeS₂ with in Situ Nanoprecipitates," *Adv. Energy Mater.*, **112**, pp. 521–525.

3. ENERGY CONVERSION MODELING IN 3D PRINTABLE COMPOSITIONALLY SEGMENTED THERMOELECTRIC LEGS

3.1. Abstract

Segmented thermoelectric generators (TEGs) comprising multiple TE elements can operate over a large thermal gradient without inherent conversion efficiency (ZT) losses of materials. However, despite excellent theoretical efficiencies, the performance of actual segmented TEGs are critically affected by several challenges related to material incompatibility and limited design flexibility in conventional fabrication processes. Herein, we report the multi-material 3D printing of composition-segmented BiSbTe materials by the sequential deposition of all-inorganic viscoelastic TE inks containing $\text{Bi}_x\text{Sb}_{2-x}\text{Te}_3$ particles, tailored with $\text{Sb}_2\text{Te}_4^{2-}$ chalcogenidometallate binders. The peak ZT s of the 3D-printed materials controllably shifted from room temperature to 250 °C by composition engineering of $\text{Bi}_x\text{Sb}_{2-x}\text{Te}_3$ particles. We fabricated the optimally designed TEG comprising the 3D-printed, composition-segmented tri-block $\text{Bi}_{0.55}\text{Sb}_{1.45}\text{Te}_3/\text{Bi}_{0.5}\text{Sb}_{1.5}\text{Te}_3/\text{Bi}_{0.35}\text{Sb}_{1.65}\text{Te}_3$ TE leg, which extends the peak ZT s and satisfies full compatibility across the entire temperature range, realizing a record-high efficiency of 8.7% under the temperature difference of 236 °C. Our approach offers a promising strategy to optimize segmented TEGs.

3.2. Introduction

Thermoelectric (TE) devices, serving as a platform for power generation from waste heat, have attracted considerable academic and industrial interest [20,23,24]. The performance of TE generators (TEGs) directly depends on the inherent conversion efficiency of the materials, $ZT = S^2\sigma T/\kappa$, where S , σ , κ and T are the Seebeck coefficient, electrical conductivity, thermal conductivity, and absolute temperature, respectively. While various classes of TE materials have been developed, BiSbTe-based compounds are predominantly used because of their high efficiency and manufacturability [15,27,29,66–71]. It is, however, a typical observation that the ZT of BiSbTe-based compounds peaks around unity at room temperature, then rapidly decreases with increasing temperature, limiting their application as a promising TEG device [28,72]. Thus, it is desired to have a wide temperature coverage of the peak ZT of the compounds, or it would be beneficial to have higher average ZT over a wider temperature range. Studies have attempted to address the issues by adjusting the composition of BiSbTe or doping it with Cd, Ag, etc [73,74]. However, such strategies cannot avoid the significant reduction of the peak ZT in BiSbTe-based compounds. A possible system-level strategy to achieve a high conversion efficiency over a wide temperature range is to make segmented TE devices comprising multiple TE elements with different operational temperatures.

3.3. Problem Statement and Background Review

Ideally, each constituent TE element needs to exhibit peak ZT at different temperature range, enabling the TEG to exploit the entire available temperature potential

[75,76]. However, despite the excellent theoretical efficiency, there are two major issues in the implementation of the segmented TEGs: materials and device fabrication. In segmented legs, the power generating performance is usually reduced by compatibility mismatch between materials with different electrical and thermal properties. However, it is difficult to fully match the compatibility among multiple TE elements considering that feasible combinations of TE compounds are quite limited in reality. Meanwhile, segmented device fabrication requires precise geometric control, since the shapes of TE segments determine the temperature distribution, heat flux, and current density [77,78]. Moreover, the bonding of the segments inevitably causes interfacial electrical and thermal losses originated from Joule heating and contact resistances. One possible solution for these challenges would be to carefully choose compatible materials, and precisely manipulate their shapes through a single-pass fabrication procedure. However, typical TE device fabrication still relies on traditional powder sintering, dicing, and assembly of TE legs, which cannot fulfil the design requirements of segmented TE devices [79–81]. Three-dimensional (3D) printing is excellent for manufacturing customized designs [82]. In this context, 3D printing can offer a substantial route to control the geometric parameters of TE legs [32]. However, the 3D printing of TE materials and devices is still in the early stage and the full functionality has not been yet applied to TE technology [52,53,83]. Recently, the development of multi-material 3D printing has extended the designability of objects beyond shaping to elaborate heterogeneous architectures [84,85]. Herein, we report the multi-material 3D printing of geometrically controlled, composition segmented multi-

BiSbTe materials by the sequential deposition of different viscoelastic TE inks (Fig. 3.1(a)).

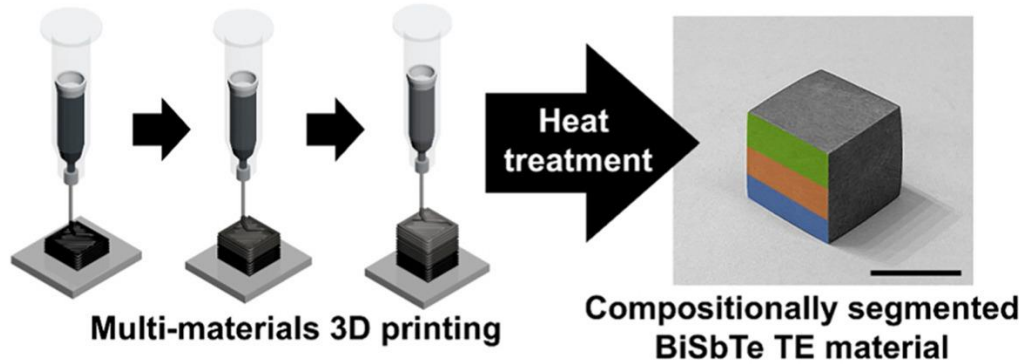


Figure 3.1. a) Scheme of a sequential 3D printing of multi-segmented TE materials. Green (Top), orange (Middle), and blue (Bottom) colored patterns correspond to each block in the compositionally segmented TE legs by multi-material 3D printing using TE inks containing $\text{Bi}_{0.55}\text{Sb}_{1.45}\text{Te}_3$, $\text{Bi}_{0.5}\text{Sb}_{1.5}\text{Te}_3$, and $\text{Bi}_{0.35}\text{Sb}_{1.65}\text{Te}_3$ particles, respectively.

3.4. FEM and Experiment Results

We conducted numerical analysis by the development of 3D finite element model (FEM) using the experimental transport data to validate our segmented TE leg design for optimal power generating performance by considering the temperature distribution, heat flux, and potential distribution (Fig. 3.2(b)). The calculated height proportions of the segments were geometrically designed to be 36.2%, 34%, and 29.8% for corresponding segments (Fig. 3.1(a)). A TEG chipped with the p-type segmented TE leg was fabricated with Cu electrodes bonded to the TE legs by Bi/Sn solder (Fig. 3.2(a)). The module resistance in the measured temperature range was as low as $1.7 \text{ m}\Omega$ at room temperatures

and was only slightly higher than the predicted values considering the material properties, demonstrating the negligible contribution of contact resistance at the smooth interfaces between segments. The TEG output characteristics were measured while heating the TEG bottom surface with heated a Cu/Sn block by a ceramic heater and cooling the top with a water-circulating cooler (Fig. 3.2(c)). To prevent excessive heat loss to the surrounding air, the lateral surfaces of the TEG and other experimental components were covered with a glass fabric insulator. During measurements, the hot-side temperature was gradually increased from 68.3 °C to 266 °C, and all properties were recorded at a steady state when the temperature fluctuation was < 3 °C. As the temperature difference (ΔT) in the TEG increased to 236 °C, the maximum voltage was recorded as 56.7 mV (Fig. 3.2(d)), and the maximum power density was estimated as 259.3 mW/cm² (Fig. 3.2(e)). For comparison, we fabricated and tested another TEG made of a single TE element only, i.e., Bi_{0.55}Sb_{1.45}Te₃ with the composition with the highest peak ZT in this work. Although the segmented TE block has the same ZT_{peak} value with Bi_{0.55}Sb_{1.45}Te₃, the average ZT of the segmented TE block is higher than that of any single element TE blocks. As shown in Fig. 3.2(d), when compared with the segmented TEG, the single-element TEG exhibited a similar power output at low temperatures, but it increased more slowly than that generated from the segmented TEG with increasing ΔT , eventually, leading to ~30% lower output at high temperatures. This demonstrates how composition-segmented TEGs can be powerful when generating over a wide temperature range. We evaluated the energy conversion efficiency (η) of the 3D-printed segmented TEG by $\eta = P/Q_h$, where P is the output power to a load, and Q_h are the heat absorbed by the TEG [20]. To determine Q_h , ΔT across a Cu/Sn block

mounted between the heater and the hot side of the TEG was measured (Fig. 3.2(c)). Similar to an ideal TEG with a constant ZT over a wide temperature range, the segmented TEG exhibited monotonically increasing η with ΔT . Importantly, η reached 8.7% at the maximum ΔT , 236 °C, which is, to the best of our knowledge, higher than previous reports at this temperature (Fig. 3.2(f)) [28,37,86–88].

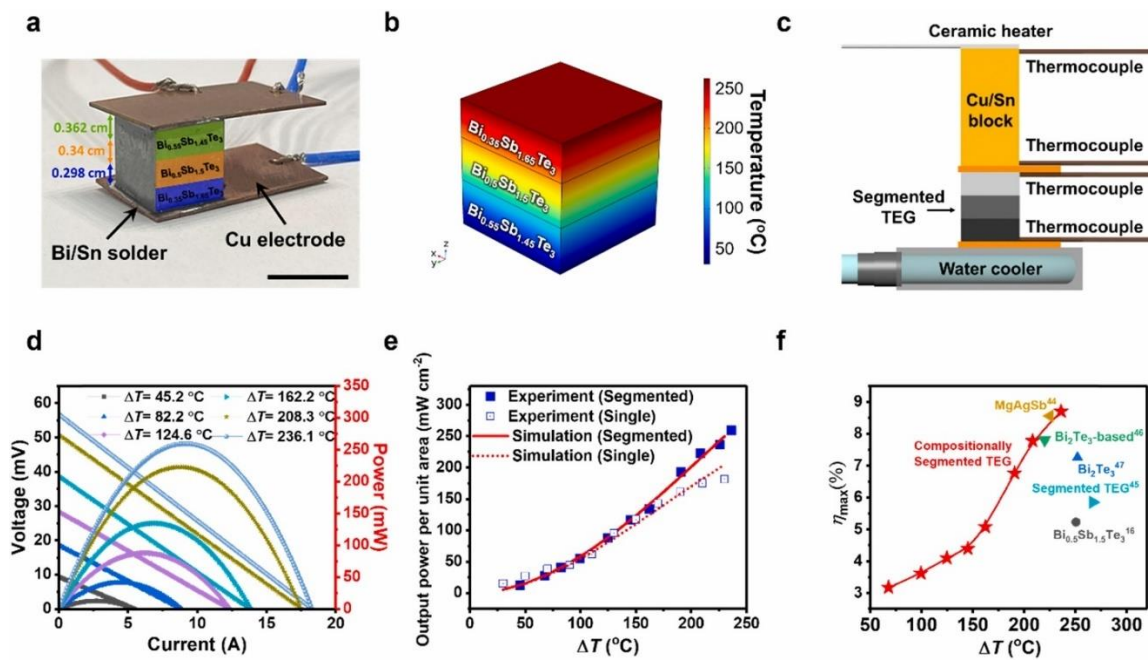


Figure 3.2. Compositionally segmented BiSbTe TEG. (a) Photograph showing compositionally segmented tri-block TE leg consisting of $\text{Bi}_{0.55}\text{Sb}_{1.45}\text{Te}_3$, $\text{Bi}_{0.5}\text{Sb}_{1.5}\text{Te}_3$, and $\text{Bi}_{0.35}\text{Sb}_{1.65}\text{Te}_3$ blocks with optimum geometry in consideration of (b) the temperature distribution derived by the numerical analysis. (c) Scheme showing the measurement set-up of output power and efficiency of the TEG. (d) Output voltage and power of the composition-segmented TEGs at different ΔT . (e) Output power densities of the composition-segmented TEGs and the 3D-printed $\text{Bi}_{0.55}\text{Sb}_{1.45}\text{Te}_3$ TEG as a function of

ΔT obtained by experiment (symbol) and FEM (line). (f) Maximum conversion efficiency as a function of ΔT for the 3D-printed, composition-segmented BiSbTe-based TEG developed in this work and data from reference [28], [37], [86], [87], [88] are shown for comparison.

The ideal Carnot engine would exhibit an efficiency of 13–44% in the same temperature range, indicating that the segmented TEG efficiency relative to the Carnot efficiency is approximately 16.4–19.8%. The main reason for such a high efficiency is that the average ZT of all leg compositions remains high throughout the wide temperature range. Such a high efficiency of 8.7% of the current 3D-printed segmented module under the ΔT of 236 °C can be understood by the optimum design of our module. The composition-segmented TE module ideally realized i) high average ZT over wide operational temperatures, ii) full compatibility among TE segments, and iii) minimal electrical and thermal losses at the junctions. Firstly, the average ZT of our segmented leg reaches as high as 0.94 in the temperature range from room temperature to 250 °C. Secondly, the composition-segmentation in a TE leg well satisfied the compatibility among TE segments, less than the factor of unity. Thirdly, this compatibility of a TE leg and the device structure consisting of a single leg led to minimal electrical and thermal losses at the junction due to the accordant electrical and thermal properties. Typically, the electrical and thermal losses at interfaces of various bonded parts of an integrated module are unavoidable, such as temperature drops across the electrodes and bonded junctions, Joule heating at bonded interfaces and thermal radiation or convection through the element gaps

or fillers. In the present work, the segmented TEG is the single leg system minimizing the number of the junctions, by which we could minimize undesired external losses in the module. For example, the measured module resistance was similar or slightly higher than the expected value by the material properties, which demonstrates the minimal electrical loss in our segmented TE leg. Kraemer, et al. reported an efficiency of 8.5% in the TE module consisting of the MgAgSb-based single leg at the temperature difference of 225 °C [37]. In this study, the average ZT of the material is 0.91 at this temperature range which is similar to that of our segmented TE leg, further supporting the reliability of our measurement and the feasibility of the design of our segmented module.

3.5. Conclusions

This study demonstrates that a compositionally segmented BiSbTe-based TEG exhibiting record-high power generation can be easily fabricated by multi-material 3D printing. The all-inorganic, composition-engineered BiSbTe-based inks enable the control of the peak ZT s in a wide temperature range without substantial loss of ZT , which extends the operating temperature range from room temperature to 250 °C. It was demonstrated that the sequential multi-material 3D printing of BiSbTe provides an unlimited degree of freedom for geometrically designing segmented TE legs without electrical or thermal losses at the interfaces, yielding a record-high efficiency. This approach will pave a new way for designing high-performance segmented TEGs in a cost-effective manner, shedding a light on the TE research community. Moreover, we believe that the currently developed process will extend the versatility of 3D printing into energy and electronic materials.

3.6. References

- [20] Bell, L. E., 2008, “Cooling, Heating, Generating Power, and Recovering Waste Heat with Thermoelectric Systems,” *Science* (80-.), **321**(5895), pp. 1457–1461.
- [21] Disalvo, F. J., 1999, “Thermoelectric Cooling and Power Generation,” *Science* (80-.), **285**(5428), pp. 703–706.
- [22] He, J., and Tritt, T. M., 2017, “Advances in Thermoelectric Materials Research: Looking Back and Moving Forward,” *Science* (80-.), **357**(6358), p. eaak9997.
- [23] Snyder, G. J., and Toberer, E. S., 2008, “Complex Thermoelectric Materials,” *Nat. Mater.*, **7**(2), pp. 105–114.
- [24] Zhang, Y., Cleary, M., Wang, X., Kempf, N., Schoensee, L., Yang, J., Joshi, G., and Meda, L., 2015, “High-Temperature and High-Power-Density Nanostructured Thermoelectric Generator for Automotive Waste Heat Recovery,” *Energy Convers. Manag.*, **105**, pp. 946–950.
- [25] Jo, S., Park, S. H., Ban, H. W., Gu, D. H., Kim, B. S., Son, J. H., Hong, H. K., Lee, Z., Han, H. S., Jo, W., Lee, J. E., and Son, J. S., 2016, “Simultaneous Improvement in Electrical and Thermal Properties of Interface-Engineered BiSbTe Nanostructured Thermoelectric Materials,” *J. Alloy. Comp.*, **689**, pp. 899–907.
- [26] Jo, S., Park, S. H., Shin, H., Oh, I., Heo, S. H., Ban, H. W., Jeong, H., Kim, F., Choo, S., Gu, D. H., Baek, S., Cho, S., Kim, J. S., Kim, B. S., Lee, J. E., Song, S., Yoo, J. W., Song, J. Y., and Son, J. S., 2019, “Soluble Telluride-Based Molecular Precursor for Solution-Processed High-Performance Thermoelectrics,” *ACS Appl. Energy Mater.*, **2**(7), pp. 4582–4589.
- [27] Kim, S. Il, Lee, K. H., Mun, H. A., Kim, H. S., Hwang, S. W., Roh, J. W., Yang, D. J., Shin, W. H., Li, X. S., Lee, Y. H., Snyder, G. J., and Kim, S. W., 2015, “Dense Dislocation Arrays Embedded in Grain Boundaries for High-Performance Bulk Thermoelectrics,” *Science* (80-.), **348**(6230), pp. 109–114.
- [28] Zheng, G., Su, X., Xie, H., Shu, Y., Liang, T., She, X., Liu, W., Yan, Y., Zhang, Q., Uher, C., Kanatzidis, M. G., and Tang, X., 2017, “High Thermoelectric Performance of P-BiSbTe Compounds Prepared by Ultra-Fast Thermally Induced Reaction,” *Energy Environ. Sci.*, **10**(12), pp. 2638–2652.
- [29] Liu, H., Shi, X., Xu, F., Zhang, L., Zhang, W., Chen, L., Li, Q., Uher, C., Day, T., and Snyder Jeffrey, G., 2012, “Copper Ion Liquid-like Thermoelectrics,” *Nat. Mater.*, **11**(5), pp. 422–425.
- [30] Liu, W. Di, Yang, L., Chen, Z. G., and Zou, J., 2020, “Promising and Eco-Friendly Cu₂X-Based Thermoelectric Materials: Progress and Applications,” *Adv. Mater.*, **32**(8), p. e1905703.

- [31] Wei, T. R., Qin, Y., Deng, T., Song, Q., Jiang, B., Liu, R., Qiu, P., Shi, X., and Chen, L., 2018, “Copper Chalcogenide Thermoelectric Materials,” *Sci. China Mater.*, **62**(1), pp. 8–24.
- [32] Zhao, K., Qiu, P., Shi, X., and Chen, L., 2019, “Recent Advances in Liquid-like Thermoelectric Materials,” *Adv. Funct. Mater.*, **30**(8), p. 1903867.
- [33] Zong, P. A., Hanus, R., Dylla, M., Tang, Y., Liao, J., Zhang, Q., Snyder, G. J., and Chen, L., 2017, “Skutterudite with Graphene-Modified Grain-Boundary Complexion Enhances ZT Enabling High-Efficiency Thermoelectric Device,” *Energy Environ. Sci.*, **10**(1), pp. 183–191.
- [34] Xing, Y., Liu, R., Liao, J., Zhang, Q., Xia, X., Wang, C., Huang, H., Chu, J., Gu, M., Zhu, T., Zhu, C., Xu, F., Yao, D., Zeng, Y., Bai, S., Uher, C., and Chen, L., 2019, “High-Efficiency Half-Heusler Thermoelectric Modules Enabled by Self-Propagating Synthesis and Topologic Structure Optimization,” *Energy Environ. Sci.*, **12**(11), pp. 3390–3399.
- [35] Heo, S. H., Jo, S., Kim, H. S., Choi, G., Song, J. Y., Kang, J. Y., Park, N. J., Ban, H. W., Kim, F., Jeong, H., Jung, J., Jang, J., Lee, W. B., Shin, H., and Son, J. S., 2019, “Composition Change-Driven Texturing and Doping in Solution-Processed SnSe Thermoelectric Thin Films,” *Nat. Commun.*, **10**(1).
- [36] Zhao, L. D., Lo, S. H., Zhang, Y., Sun, H., Tan, G., Uher, C., Wolverton, C., Dravid, V. P., and Kanatzidis, M. G., 2014, “Ultralow Thermal Conductivity and High Thermoelectric Figure of Merit in SnSe Crystals,” *Nature*, **508**(7496), pp. 373–377.
- [37] Kraemer, D., Sui, J., McEnaney, K., Zhao, H., Jie, Q., Ren, Z. F., and Chen, G., 2015, “High Thermoelectric Conversion Efficiency of MgAgSb-Based Material with Hot-Pressed Contacts,” *Energy Environ. Sci.*, **8**(4), pp. 1299–1308.
- [38] Choi, J., Jung, Y., Yang, S. J., Oh, J. Y., Oh, J., Jo, K., Son, J. G., Moon, S. E., Park, C. R., and Kim, H., 2017, “Flexible and Robust Thermoelectric Generators Based on All-Carbon Nanotube Yarn without Metal Electrodes,” *ACS Nano*, **11**(8), pp. 7608–7614.
- [39] Gu, D. H., Jo, S., Jeong, H., Ban, H. W., Park, S. H., Heo, S. H., Kim, F., Jang, J. I., Lee, J. E., and Son, J. S., 2017, “Colloidal Synthesis of Te-Doped Bi Nanoparticles: Low-Temperature Charge Transport and Thermoelectric Properties,” *ACS Appl. Mater. Interfaces*, **9**(22), pp. 19143–19151.
- [40] Kim, J., Bae, E. J., Kang, Y. H., Lee, C., and Cho, S. Y., 2020, “Elastic Thermoelectric Sponge for Pressure-Induced Enhancement of Power Generation,” *Nano Energy*, **74**, p. 104824.
- [41] Ferreira-Teixeira, S., and Pereira, A. M., 2018, “Geometrical Optimization of a Thermoelectric Device: Numerical Simulations,” *Energy Convers. Manag.*, **169**,

pp. 217–227.

- [42] Xing, T., Song, Q., Qiu, P., Zhang, Q., Gu, M., Xia, X., Liao, J., Shi, X., and Chen, L., 2021, “High Efficiency GeTe-Based Materials and Modules for Thermoelectric Power Generation,” *Energy Environ. Sci.*, **14**(2), pp. 995–1003.
- [43] Qiu, P., Mao, T., Huang, Z., Xia, X., Liao, J., Agne, M. T., Gu, M., Zhang, Q., Ren, D., Bai, S., Shi, X., Snyder, G. J., and Chen, L., 2019, “High-Efficiency and Stable Thermoelectric Module Based on Liquid-like Materials,” *Joule*, **3**(6), pp. 1538–1548.
- [44] Yeo, S. J., Oh, M. J., and Yoo, P. J., 2019, “Structurally Controlled Cellular Architectures for High Performance Ultra Lightweight Materials,” *Adv. Mater.*, **31**(34), p. 1803670.
- [45] Tian, X., and Zhou, K., 2020, “3D Printing of Cellular Materials for Advanced Electrochemical Energy Storage and Conversion,” *Nanoscale*, **12**(14), pp. 7416–7432.
- [46] Schaedler, T. A., Jacobsen, A. J., Torrents, A., Sorensen, A. E., Lian, J., Greer, J. R., Valdevit, L., and Carter, W. B., 2011, “Ultralight Metallic Microlattices,” *Science* (80-.), **334**(6058), pp. 962–965.
- [47] Berger, J. B., Wadley, H. N. G., and McMeeking, R. M., 2017, “Mechanical Metamaterials at the Theoretical Limit of Isotropic Elastic Stiffness,” *Nature*, **543**(7646), pp. 533–537.
- [48] Bauer, J., Hengsbach, S., Tesari, I., Schwaiger, R., and Kraft, O., 2014, “High-Strength Cellular Ceramic Composites with 3D Microarchitecture,” *Proc. Natl Acad. Sci. USA*, **111**(7), pp. 2453–2458.
- [49] Muth, J. T., Dixon, P. G., Woish, L., Gibson, L. J., and Lewis, J. A., 2017, “Architected Cellular Ceramics with Tailored Stiffness via Direct Foam Writing,” *Proc. Natl Acad. Sci. USA*, **114**(8), pp. 1832–1837.
- [50] Lewis, J. A., and Ahn, B. Y., 2015, “Three-Dimensional Printed Electronics,” *Nature*, **518**(7537), pp. 42–43.
- [51] Sun, K., Wei, T. S., Ahn, B. Y., Seo, J. Y., Dillon, S. J., and Lewis, J. A., 2013, “3D Printing of Interdigitated Li-Ion Microbattery Architectures,” *Adv. Mater.*, **25**(33), pp. 4539–4543.
- [52] He, M., Zhao, Y., Wang, B., Xi, Q., Zhou, J., and Liang, Z., 2015, “3D Printing Fabrication of Amorphous Thermoelectric Materials with Ultralow Thermal Conductivity,” *Small*, **11**(44), pp. 5889–5894.
- [53] Qiu, J., Yan, Y., Luo, T., Tang, K., Yao, L., Zhang, J., Zhang, M., Su, X., Tan, G., Xie, H., Kanatzidis, M. G., Uher, C., and Tang, X., 2019, “3D Printing of Highly Textured Bulk Thermoelectric Materials: Mechanically Robust BiSbTe Alloys

- with Superior Performance,” *Energy Environ. Sci.*, **12**(10), pp. 3106–3117.
- [54] Du, Y., Chen, J., Meng, Q., Xu, J., Paul, B., and Eklund, P., 2020, “Flexible Ternary Carbon Black/Bi₂Te₃ Based Alloy/Poly(lactic Acid) Thermoelectric Composites Fabricated by Additive Manufacturing,” *J. Mater.*, **6**(2), pp. 293–299.
- [55] Oztan, C., Ballikaya, S., Ozgun, U., Karkkainen, R., and Celik, E., 2019, “Additive Manufacturing of Thermoelectric Materials via Fused Filament Fabrication,” *Appl. Mater. Today*, **15**, pp. 77–82.
- [56] Jo, S., Choo, S., Kim, F., Heo, S. H., and Son, J. S., 2019, “Ink Processing for Thermoelectric Materials and Power-Generating Devices,” *Adv. Mater.*, **31**(20), p. e1804930.
- [57] Aw, Y. Y., Yeoh, C. K., Idris, M. A., Teh, P. L., Hamzah, K. A., and Sazali, S. A., 2018, “Effect of Printing Parameters on Tensile, Dynamic Mechanical, and Thermoelectric Properties of FDM 3D Printed CABS/ZnO Composites,” *Materials (Basel)*, **11**(4), p. 466.
- [58] Su, N., Zhu, P., Pan, Y., Li, F., and Li, B., 2020, “3D-Printing of Shape-Controllable Thermoelectric Devices with Enhanced Output Performance,” *Energy*, **195**, p. 116892.
- [59] Yazawa, K., and Shakouri, A., 2017, “Optimization of Power and Efficiency of Thermoelectric Devices with Asymmetric Thermal Contacts,” *J. Appl. Phys.*, **111**(2), p. 024509.
- [60] Roh, I. J., Lee, Y. G., Kang, M. S., Lee, J. U., Baek, S. H., Kim, S. K., Ju, B. K., Hyun, D. Bin, Kim, J. S., and Kwon, B., 2016, “Harman Measurements for Thermoelectric Materials and Modules under Non-Adiabatic Conditions,” *Sci. Rep.*, **6**.
- [61] Meo, M., Morris, A. J., Vignjevic, R., and Marengo, G., 2003, “Numerical Simulations of Low-Velocity Impact on an Aircraft Sandwich Panel,” *Compos. Struct.*, **62**(3–4), pp. 3–4.
- [62] Lu, C., Zhao, M., Jie, L., Wang, J., Gao, Y., Cui, X., and Chen, P., 2015, “Stress Distribution on Composite Honeycomb Sandwich Structure Suffered from Bending Load,” *Procedia Eng.*, **99**, pp. 405–412.
- [63] Sun, G., Huo, X., Chen, D., and Li, Q., 2017, “Experimental and Numerical Study on Honeycomb Sandwich Panels under Bending and In-Panel Compression,” *Mater. Des.*, **133**, pp. 154–168.
- [64] Wang, X., Qiu, P., Zhang, T., Ren, D., Wu, L., Shi, X., Yang, J., and Chen, L., 2015, “Compound Defects and Thermoelectric Properties in Ternary CuAgSe-Based Materials,” *J. Mater. Chem. A*, **3**(26), pp. 13662–13670.
- [65] Xie, H., 2008, “The Role of Zn in Chalcopyrite CuFeS₂: Enhanced Thermoelectric

Properties of Cu₁-XZn_xFeS₂ with in Situ Nanoprecipitates,” *Adv. Energy Mater.*, **112**, pp. 521–525.

- [66] Zhao, L. D., Lo, S. H., Zhang, Y., Sun, H., Tan, G., Uher, C., Wolverton, C., Dravid, V. P., and Kanatzidis, M. G., 2014, “Ultralow Thermal Conductivity and High Thermoelectric Figure of Merit in SnSe Crystals,” *Nature*, **508**(7496), pp. 373–377.
- [67] Heremans, J. P., Jovovic, V., Toberer, E. S., Saramat, A., Kurosaki, K., Charoenphakdee, A., Yamanaka, S., and Snyder, G. J., 2008, “Enhancement of Thermoelectric Efficiency in PbTe by Distortion of the Electronic Density of States,” *Science* (80-.), **321**(5888), pp. 554–557.
- [68] Sales, B. C., Mandrus, D., and Williams, R. K., 1996, “Filled Skutterudite Antimonides: A New Class of Thermoelectric Materials,” *Science* (80-.), **272**(5266), pp. 1325–1328.
- [69] Lan, Y., Minnich, A. J., Chen, G., and Ren, Z., 2010, “Enhancement of Thermoelectric Figure-of-Merit by a Bulk Nanostructuring Approach,” *Adv. Funct. Mater.*, **20**(3), pp. 357–376.
- [70] Pei, Y., Shi, X., Lalonde, A., Wang, H., Chen, L., and Snyder, G. J., 2011, “Convergence of Electronic Bands for High Performance Bulk Thermoelectrics,” *Nature*, **473**(7345), pp. 66–69.
- [71] Hao, F., Qiu, P., Tang, Y., Bai, S., Xing, T., Chu, H. S., Zhang, Q., Lu, P., Zhang, T., Ren, D., Chen, J., Shi, X., and Chen, L., 2016, “High Efficiency Bi₂Te₃-Based Materials and Devices for Thermoelectric Power Generation between 100 and 300 °c,” *Energy Environ. Sci.*, **9**(10), pp. 3120–3127.
- [72] Mun, H., Choi, S. M., Lee, K. H., and Kim, S. W., 2015, “Boundary Engineering for the Thermoelectric Performance of Bulk Alloys Based on Bismuth Telluride,” *ChemSusChem*, **8**(14), pp. 2312–2326.
- [73] Seo, S., Desilva, M. A., Xia, H., and Brennecke, J. F., 2015, “Effect of Cation on Physical Properties and CO₂ Solubility for Phosphonium-Based Ionic Liquids with 2-Cyanopyrrolide Anions,” *J. Phys. Chem. B*, **119**(35), pp. 11807–11814.
- [74] Wei, Z., Li, Z., Luo, P., Zhang, J., and Luo, J., 2020, “Simultaneously Increased Carrier Concentration and Mobility in P-Type Bi_{0.5}Sb_{1.5}Te₃ Throng Cd Doping,” *J. Alloys Compd.*, **830**.
- [75] Ngan, P. H., Christensen, D. V., Snyder, G. J., Hung, L. T., Linderoth, S., Nong, N. Van, and Pryds, N., 2014, “Towards High Efficiency Segmented Thermoelectric Unicouples,” *Phys. Status Solidi Appl. Mater. Sci.*, **211**(1), pp. 9–17.
- [76] Zhang, Q., Liao, J., Tang, Y., Gu, M., Ming, C., Qiu, P., Bai, S., Shi, X., Uher, C.,

- and Chen, L., 2017, “Realizing a Thermoelectric Conversion Efficiency of 12% in Bismuth Telluride/Skutterudite Segmented Modules through Full-Parameter Optimization and Energy-Loss Minimized Integration,” *Energy Environ. Sci.*, **10**(4), pp. 956–963.
- [77] Badillo-Ruiz, C. A., Olivares-Robles, M. A., and Ruiz-Ortega, P. E., 2018, “Performance of Segmented Thermoelectric Cooler Micro-Elements with Different Geometric Shapes and Temperature-Dependent Properties,” *Entropy*, **20**(2).
- [78] Qiu, P., Mao, T., Huang, Z., Xia, X., Liao, J., Agne, M. T., Gu, M., Zhang, Q., Ren, D., Bai, S., Shi, X., Snyder, G. J., and Chen, L., 2019, “High-Efficiency and Stable Thermoelectric Module Based on Liquid-Like Materials,” *Joule*, **3**(6), pp. 1538–1548.
- [79] Pu, H. Y., Xie, R. Q., Peng, Y., Yang, Y., He, S. Y., Luo, J., Sun, Y., Xie, S. R., and Luo, J., 2019, “Accelerating Sample Preparation of Graded Thermoelectric Materials Using an Automatic Powder Feeding System,” *Adv. Manuf.*, **7**(3), pp. 278–287.
- [80] Qi, X., Chen, J., Guo, K., He, S., Yang, J., Li, Z., Xing, J., Hu, J., Luo, H., Zhang, W., and Luo, J., 2019, “Thermal Stability of Ag₉GaSe₆ and Its Potential as a Functionally Graded Thermoelectric Material,” *Chem. Eng. J.*, **374**, pp. 494–501.
- [81] Gelbstein, Y., Dashevsky, Z., and Dariel, M. P., 2007, “Powder Metallurgical Processing of Functionally Graded P-Pb₁-XS_nTe Materials for Thermoelectric Applications,” *Phys. B Condens. Matter*, **391**(2), pp. 256–265.
- [82] Farahani, R. D., Dubé, M., and Therriault, D., 2016, “Three-Dimensional Printing of Multifunctional Nanocomposites: Manufacturing Techniques and Applications,” *Adv. Mater.*, **28**(28), pp. 5794–5821.
- [83] Burton, M. R., Mehraban, S., Beynon, D., McGettrick, J., Watson, T., Lavery, N. P., and Carnie, M. J., 2019, “3D Printed SnSe Thermoelectric Generators with High Figure of Merit,” *Adv. Energy Mater.*, **9**(26).
- [84] Skylar-Scott, M. A., Mueller, J., Visser, C. W., and Lewis, J. A., 2019, “Voxelated Soft Matter via Multimaterial Multinozzle 3D Printing,” *Nature*, **575**(7782), pp. 330–335.
- [85] Hardin, J. O., Ober, T. J., Valentine, A. D., and Lewis, J. A., 2015, “Microfluidic Printheads for Multimaterial 3D Printing of Viscoelastic Inks,” *Adv. Mater.*, **27**(21), pp. 3279–3284.
- [86] Crane, D. T., Kossakovski, D., and Bell, L. E., 2009, “Modeling the Building Blocks of a 10% Efficient Segmented Thermoelectric Power Generator,” *J. Electron. Mater.*, **38**(7), pp. 1382–1386.

- [87] Anatyshuk, L. I., Vikhor, L. N., Strutynska, L. T., and Termena, I. S., 2011, "Segmented Generator Modules Using Bi₂Te₃-Based Materials," *J. Electron. Mater.*, **40**(5), pp. 957–961.
- [88] Kuroki, T., Kabeya, K., Makino, K., Kajihara, T., Kaibe, H., Hachiuma, H., Matsuno, H., and Fujibayashi, A., 2014, "Thermoelectric Generation Using Waste Heat in Steel Works," *J. Electron. Mater.*, **43**(6), pp. 2405–2410.

4. NON-LINEAR TRANSPORT MECHANISM MODELING IN COPPER-CARBON NANOTUBE COMPOSITES

4.1. Abstract

Copper (Cu)-carbon nanotube (CNT) composites are considered as potential alternatives for pure Cu based on the theoretical predictions of their superior electrical, thermal, and mechanical properties. However, the conductivities of experimentally synthesized Cu-CNT composites rarely exceed those of Cu primarily due to the large inherent interface resistances. Here, this article presents a two-dimensional (2D) finite element model (FEM) which account for the interface resistances both at CNT-CNT and Cu-CNT contacts, random distribution of CNTs, and CNT fractions up to 80%. The model predicts that the high concentration of single-walled CNTs in Cu matrix may enhance the composite electrical and thermal conductivity by up-to ~ 5 times at 27 °C only when interface resistances are highly regulated below 1 k Ω and 10^{-7} m²K/W. The streamlines of electrical current and heat flow reveal that the CNTs serve as an effective conduction medium only with the low levels of interface resistance. This work elucidates the importance of interface resistances for the electrical and thermal transport in Cu-CNT composites.

4.2. Introduction

Carbon nanotubes possess remarkable properties, including high electrical and thermal conductivity. Their unique electronic and crystal structures enable the delocalization of electrons along their length, resulting in high electrical conductivity. The

strong covalent bonds between carbon atoms also enable rapid transfer of thermal energy, making them useful in heat management applications. Carbon nanotubes (CNTs) are mechanically flexible, tortuous, readily form entangled networks, and are highly anisotropic because of their extremely large length-to-diameter aspect ratios (from 500 to 2000) [89]. Such CNT characteristics are crucial for the composite properties, necessitating the alignment of CNT orientations to enhance their bulk properties. In a single-walled CNT (SWCNT) at room temperature, the electrical conductivity is ~24 times greater [90] and the thermal conductivity is two orders of magnitude greater along the longitudinal direction than those along the transverse direction [91]. Due to the significant anisotropy, the experimentally measured electrical conductance of copper (Cu)-CNT composite approximately doubled when SWCNT were perfectly oriented to the electric bias (orientation angle = 0°) relative to the orientation angle of 45° [92]. According to effective-medium model calculations, the electrical conductivities of Cu-CNT composite were twice that of pure copper when 30–40 vol.% of defect-free CNTs were aligned along the bias direction [93]. Atomistic simulations predicted that Cu-CNT composites with minimally aggregated and aligned CNTs showed up-to ~2.25 times greater thermal conductivities than pure copper [94–96].

4.3. Background Review and Problem Statement

There have been extensive efforts to align the CNT orientations and reduce tortuosity in manufacturing processes to enhance the bulk conductivities in a desired direction. Several studies have reported post-production steps in powder-processed

composites like die stretching [97,98], speed rolling [99], magnetic [100] and electric field applications [101]. A study demonstrated a die-stretching method to align CNTs in Cu-CNT composite, which increased the tensile strength by ~30% and thermal conductivity by ~29% [12]. In another work, researchers fabricated Cu-CNT composites with uniaxial freeze-drying, aligned the CNTs using a magnetic field of 1 tesla, and augmented the composite thermal conductivity by ~300% [100]. In one study, CNT based polymer composites with 3 wt.% of CNT presented 35% reduction in electrical resistivity and 10% increase in thermal conductivity by aligning the CNTs via magnetic field processing [102]. In CNT based epoxy composites, the electrical conductivity increased by 10 orders of magnitude by aligning 3 wt.% of CNTs using die stretching technique [103]. In another study, researchers embedded quasi-straight CNTs in epoxy resin via solution casting and repetitive stretching [104]. The study reported that the electrical conductivity was enhanced by ~3 orders of magnitude when the CNT orientations rotated from perpendicular to parallel direction toward the electrical potential. Similarly, another study showed that the electrical conductivity of epoxy-CNT composites increased ~2.5 orders of magnitude when bias potential was parallel to the CNT alignment orientations [11]. In a previous experimental study, an electric field of 43.5 kV/m at frequency of 10 Hz was applied to align CNTs in a SWCNT-polymer composite, resulting in 5 orders of magnitude increase in electrical conductivity [12]. Similarly, an electric field and current assisted alignment contributed to 360% increase in electrical conductivity in CNT based polyvinylidene fluoride (PVDF) composite [105]. One previous research carried out mesoscopic

simulations for CNT-polymer composites and observed that the CNT alignment provided up-to ~4.5-fold enhancement in thermal conductivity [9].

For metal-CNT composites, the CNT-template electrodeposition method has been employed to preserve the CNT intrinsic conductivities by directly embedding aligned CNTs in metal matrix, and to achieve a high-volume fraction (45–50 vol.%) [106–109]. Straight CNTs can be synthesized for the template electrodeposition process using current nanotube synthesis techniques [110–112]. An experimental study demonstrated that Cu-CNT composites made from the CNT-template electrodeposition presented a CNT volume fraction of 45%, 100 times greater ampacity, 26% greater specific electrical conductivity, and similar thermal conductivity compared to pure copper at room temperature [106]. In another research, Cu-CNT composites fabricated by the CNT-template electrodeposition also exhibited 45 vol.% of CNT and a thermal conductivity of ~395 W/m·K at room temperature which was the highest conductivity reported for CNT-metal composites containing over 10 vol.% of CNT [107].

Despite the significant experimental efforts made for CNT orientations alignment and CNT straightening, the bulk conductivities of CNT-metal composites still do not far exceed those of pure metals presumably due to the large contact resistances present in the composite systems [94,113–115]. Contact resistances exist at CNT-metal and CNT-CNT interfaces, creating detrimental impacts on conductivities. The CNT-metal contact resistance is contingent on the synthesis process and originates from the imperfect adhesions and poor wettability between CNTs and copper [114,116,117]. Even with a perfect Cu-CNT bonding, the CNT-metal contact resistance still exists due to the mismatch

in the work functions [118]. The CNT-metal interfacial resistances are typically mitigated by employing carbide forming metals to improve Cu-CNT wettability [117,119–123]. One study fabricated Cu-CNT composites with tungsten as doping element to improve the interface bonding force between Cu and CNTs. Doped Cu-CNT composite exhibited ~6% greater electrical conductivity than undoped Cu-CNT composite [117]. Another study used chromium (Cr) as doping element to improve the Cu-CNT composite electrical conductivity by ~5% [119]. Doping with Cr also enhanced the thermal conductivity of Cu-CNT composites by 17% owing to the reinforced Cu-CNT bonding [120]. The CNT-CNT contact resistance exists at the CNT interconnects where CNTs are within the van der Waals (vdWs) distance. If the CNTs are in such extreme proximity, electrons and phonons can flow across the CNTs, but the electrical and thermal transports are affected by the interface resistances. The ballistic phonon and electron propagation within each CNT are scattered at the interface resulting in notably large CNT-CNT interfacial thermal resistance (up-to $\sim 10^{-7}$ m²K/W) and electrical resistance (up-to $\sim 10^4$ k Ω) [96,116,124–126].

For the applications of CNT composites, there has been effort to model the interplay between the CNT- and bulk-scale properties. Three-dimensional (3D) simulation models were developed to account for the geometric complexity of the CNT composites. A previous study simulated the electrical properties of 3D entangled CNT networks in an insulating matrix with CNT concentrations less than 0.3 vol.% [89]. The finite element model (FEM) simulations showed that the CNT-CNT contact resistance and the CNT morphological parameters such as CNT aspect ratio and tortuosity were crucial for the composite electrical conductivity. Another work investigated the influence of CNT-CNT

contact resistance, the length, diameter, and critical volume fractions of CNTs on the composite electrical conductivity by employing Monte Carlo simulation [127]. Another study employed 3D FEM to investigate the effect of axial loading on the CNT-CNT contacts in a CNT-epoxy composite with 0.5 vol.% CNT [128]. Although 3D modeling enables the modeling of realistic CNT morphologies in composites, it inevitably necessitates extensive computational resources due to the requirement of extremely fine mesh for CNTs, limiting the CNT volume fraction in simulation models below a few percentages. Alternatively, analytical models have been developed and shown to be effective in the bulk property estimation, although these models simplify the geometric characteristics of the CNT composites. Various analytical models were developed to investigate the influences of percolation path [129,130], CNT concentrations [131,132], aspect ratio [129,133], and tortuosity of CNTs [134] on the electrical conductivity of the CNT composites. Various models based on effective medium theory (e.g., Maxwell-Garnett model) were used to predict the thermal conductivities of CNT composites when the CNTs volumetric fraction was less than the percolation threshold ($< 0.1\%$) [113,114,135]. Although the previous models may give acceptable results, most models did not consider the interplay between the contact resistances both at CNT-metal and CNT-CNT interfaces, stochastic nature of CNT distribution, and a wide range of CNT concentrations due to the model complexity.

Herein, our work aims to study the electrical and thermal conductivities of Cu-CNT composites while accounting for the stochastic conduction networks, contact resistances both at Cu-CNT and CNT-CNT interfaces. For the first time, we report a two-dimensional

(2D) FEM for the CNT composites with simplified CNT morphology. Although the 2D approximation and simplification for the CNT morphologies would compromise the accuracy in simulations, these assumptions enable to simulate the complex transport phenomena in the CNT composites with high CNT volume fractions (up to 80%). Moreover, the 2D FEM simulations can be used to elucidate the dominant conduction paths in the composites when the contact resistances are manipulated over a wide range. It should be noted that this FEM may provide us appreciate insight into bulk properties of Cu-CNT composite on macroscale but it does not model the atomic level interactions between electrons and phonons which play critical role in the transport properties of CNT based composites.

4.4. Finite Element Model

To understand the electrical and thermal transports in aligned CNT composites with a wide range of CNT fractions, our model focuses on a simplified 2D Cu-CNT composite. Figure 4.1(a) shows a 3D schematic of Cu-CNT composite where CNTs are aligned to the field direction. In the composite, three types of contact between CNTs and copper matrix are possible [122,128,136] as illustrated in Fig. 4.1(b). Type I contact represents the Cu-CNT interfacial resistance. Type II contact represents the end-to-end contact resistance between two CNTs. Type III contact represents the side-to-side contact resistance between two CNTs. Type II and type III contact resistances are important when CNTs are separated by a distance less than vdWs spacing (~ 1 nm). Table 4.1 summarizes the type I interfacial resistances reported for Cu-CNT composites and type II and III interfacial resistances

between CNTs, along with the properties of SWCNT and copper near room temperature. To account for the CNT-CNT interface resistance in our model, several geometric parameters are defined in Fig. 4.1(b) including the CNT length, l_{CNT} , CNT width, w_{CNT} , horizontal spacing between CNTs, d_x , and vertical spacing between CNTs, d_y . The model employs l_{CNT} of 500 nm and w_{CNT} of 3 nm. Type II contact resistance is considered if $d_x \leq l_{CNT} + 1$ nm and $d_y \leq w_{CNT}$. Type III contact resistance is considered if $d_x \leq l_{CNT}$ and $d_y \leq w_{CNT} + 1$ nm.

To simulate the transport phenomena in 2D Cu-CNT composites, our FEM follows the three steps: (i) randomly distributing CNTs in a copper matrix, (ii) creating resistive elements at type II and III contacts, and (iii) computing the electrical potential and temperature fields in the composite.

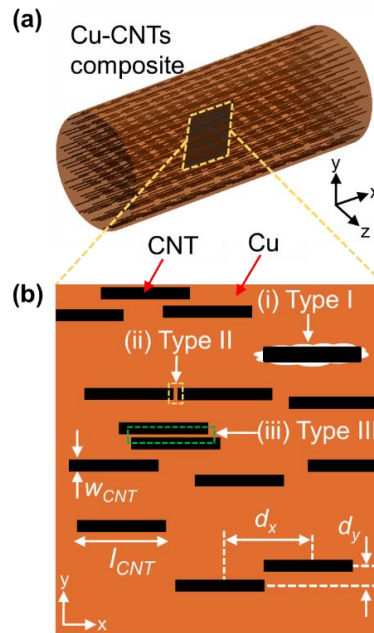


Figure 4.1. (a) 3D schematic of a Cu-CNT composite. (b) Three types of contacts in Cu-CNT composites: (i) type I: Cu-CNT interface contact (white dashed line), (ii) type II: end-

to-end contact (yellow dashed line) and (iii) type III: side-to-side contact (green dashed line).

Figure 4.2 depicts how the CNTs are randomly distributed in a copper matrix of length L and width W while achieving a CNT volume fraction f . First, CNTs of full length l_{CNT} are distributed in a domain with an extended length, $L' = L + l_{CNT}$. The maximum number of CNTs per each y -position, n_{max} , is limited by the relation $L' = n_{max} \times l_{CNT}$. The maximum number of y -positions allowed for CNTs, i_{max} , is determined by the total number of CNTs divided by n_{max} . The total number of CNTs is obtained from f . The CNT distribution begins by randomly locating CNTs in the first y -position, $y_1 = 0.5w_{CNT}$, while satisfying $d_x > l_{CNT}$ as shown in Fig. 4.2(a). In the next y -position, $y_2 > y_1 + w_{CNT}$, CNTs are randomly positioned as shown in Fig. 4.2(b), and this process repeats until the number of y -positions reaches i_{max} , as shown in Fig. 4.2(c). Then, all the CNT positions are randomly offset both in x and y directions without an overlap between CNTs as depicted in Fig. 4.2(d). Finally, the $L' \times W$ domain is truncated to a $L \times W$ domain, resulting in the truncation of some CNTs near the $L \times W$ domain boundaries. Figure 4.3 illustrates the examples of the Cu-CNT models generated for various f .

The spacing between two neighboring CNTs dictate where the type II and III contacts exist. If the inter-CNT distance is less than the vdWs spacing, we create a rectangular resistive element in the interface region to model the CNT-CNT contact resistance, similar to previous works [89,127]. The resistive elements possess constant values of interfacial electrical resistances, $R_{c,CNT-CNT} = 10^2$ k Ω , and interfacial thermal resistance, $R''_{CNT-CNT} = 10^{-8}$ m²K/W, which were obtained by averaging the values reported

in the literature listed in Table 4.1. The simulations are conducted for two separate configurations: (i) steady-state electrical conduction and (ii) heat conduction without internal heat generation. For electrical analysis, a potential difference across the domain, ΔV , is $1 \mu\text{V}$. For thermal analysis, the initial domain temperature is set to 27°C . A temperature difference across the domain, ΔT , is 1°C . The boundaries that are perpendicular to the field direction are electrically and thermally insulated. The entire Cu-CNT interface is subject to the type I interfacial electrical resistance, $R_c = 60 \Omega\text{--}60 \text{ k}\Omega$ and interfacial thermal resistance, $R''_{t,c} = 10^{-10}\text{--}10^{-7} \text{ m}^2\text{K/W}$.

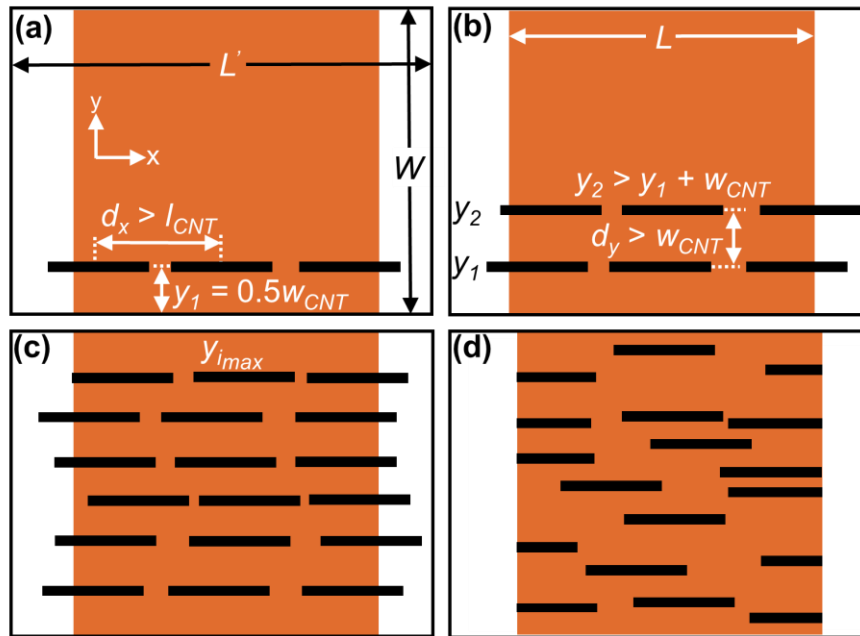


Figure 4.2. Cu-CNT composite model generation: (a) locating CNTs at y_1 , (b) locating CNTs at y_2 , (c) locating CNTs at all y positions, and (d) giving random offsets to CNTs and truncating CNTs outside the domain $L \times W$.

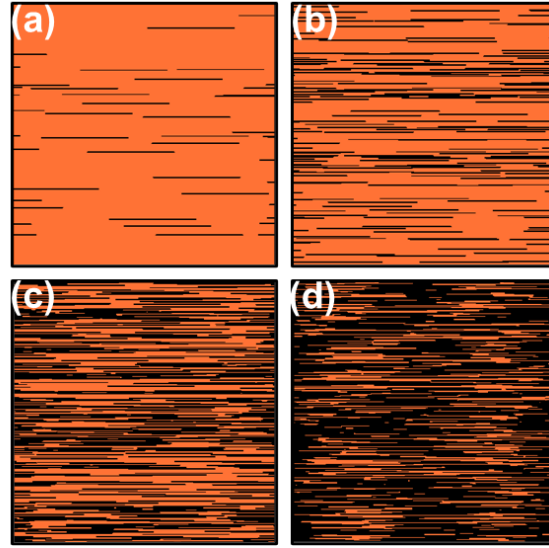


Figure 4.3. Randomly generated Cu-CNT composite models with (a) $f = 5\%$, (b) $f = 20\%$, (c) $f = 50\%$, and (d) $f = 80\%$.

Table 4.1. Properties used to simulate the Cu-CNT composites

Property	Symbol	Units	Values	References
Thermal conductivity of copper matrix	k_m	W/m·K	401	[94]
Electrical conductivity of copper matrix	σ_m	S/m	0.58×10^8	[94]
Thermal conductivity of SWCNT	k_{CNT}	W/m·K	2980	[137,138]
Electrical conductivity of SWCNT	σ_{CNT}	S/m	7.1×10^9	[139]
Type I interfacial thermal resistance	$R''_{t,c}$	m ² K/W	10^{-10} – 10^{-7}	[95,96,113]
Type I interfacial electrical resistance	R_c	Ω	20 – 2×10^4	[140–144]
Type II and III interfacial thermal resistance	$R''_{CNT-CNT}$	m ² K/W	10^{-9} – 10^{-7}	[116,124]
Type II and III interfacial electrical resistance	$R_{c,CNT-CNT}$	k Ω	10^0 – 10^4	[125,126]

4.4.1. Generation of Stochastic Cu-CNT Networks

For each fraction, the simulations are repetitively performed on 10 Cu-CNT composite models with different CNT distributions, and their results are averaged to obtain a representative result for a certain f . The FEM simulation solves the 2D electrical and heat conduction equations in Cu-CNT models to estimate the electric potential and temperature

distributions. The resulting current density, J , and conductive heat flux, q'' across the domain boundary at $x = L$, are computed. The Cu-CNT composite effective electrical conductivity, σ_e , is calculated by a relation $\sigma_e = \int J dy|_{x=L} / \Delta V$. The effective thermal conductivity, k_e , is calculated by a relation $k_e = \int q'' dy|_{x=L} / \Delta T$. The conductivities are normalized by using Cu matrix electrical conductivity, σ_m , and thermal conductivity, k_m , at room temperature.

4.4.2. Computational Domain size and Grid Independence Test

The FEM solutions must be independent of computational domain size, which can be achieved by creating a stochastic system including enough number of CNTs. We compared the simulation results for three domain sizes to understand the domain size effect when f was 80%. Figure 4.4 shows σ_e/σ_m and k_e/k_m as a function of the interface resistances while varying the simulation domain width as $L = 1l_{CNT}, 3l_{CNT}, 6l_{CNT}$. The number of CNTs corresponding to each domain size is approximately 130, 1200 and 4750. Both σ_e and k_e calculated with a small domain, i.e., $L = 1l_{CNT}$, deviate more than 10% from the conductivities obtained with a large domain, i.e., $L = 6l_{CNT}$. When the domain width becomes equal or greater than $L = 3l_{CNT}$, the predicted σ_e and k_e deviate below 3% relative to the conductivities obtained at $L = 6l_{CNT}$. Thus, for computational efficiency, we employed $L = 3l_{CNT}$ for the subsequent simulations. Interestingly, the range between the maximum and minimum conductivities obtained from different CNT distributions increases with the domain size. For example, when $L = 6l_{CNT}$ and $R''_{t,c} = 10^{-10} \text{ m}^2\text{K/W}$, the range of k_e/k_m stretches to $\sim 2.1\text{--}4.8$. When CNTs were aggregated and created a large CNT-

CNT contact area, the conductivity was highly improved if the interface resistances were small. Based on the ranges of conductivities shown in Fig. 4.4, it seems that the effect of how CNTs are aggregated becomes more important for the larger domain. Furthermore, a grid test was conducted to determine the minimum grid size ensuring accuracy and computational efficiency. The subsequent simulations use a minimum grid size of 0.1 nm.

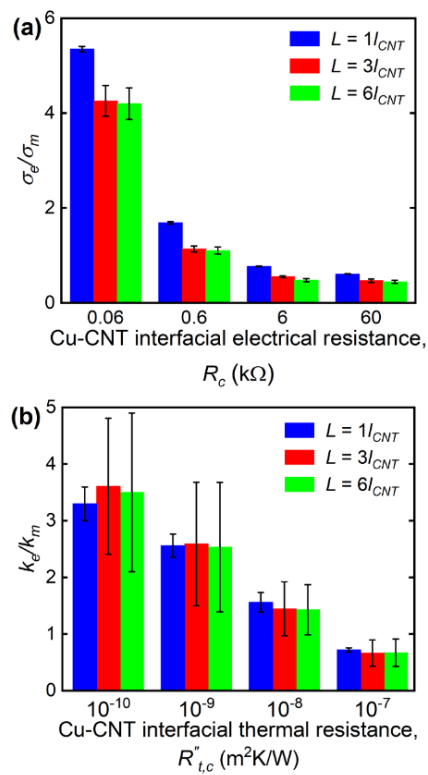


Figure 4.4. (a) σ_e/σ_m as a function of R_c and (b) k_e/k_m as a function of $R''_{t,c}$ for various domain sizes. The error bar represents the range between maximum and minimum conductivities.

4.5. Model Estimations and Comparison to Experiments

This section presents the simulation results obtained for $f = 5\text{--}80\%$, $R_c = 60\ \Omega\text{--}60\ \text{k}\Omega$ and $R''_{t,c} = 10^{-10}\text{--}10^{-7}\ \text{m}^2\text{K/W}$. We compare the FEM predictions with the conductivities reported in literature to estimate the order of magnitude of interface resistances in bulk composite materials. To understand the dominant conduction paths in the composites, the streamlines of current and heat flows are visualized.

Figure 4.5 shows σ_e/σ_m of Cu-CNT composite as a function of f predicted by FEM along with previously reported records. When the type I interfacial electrical resistance R_c is highly regulated (i.e., $R_c \leq 600\ \Omega$), σ_e increases as f increases, which is a desirable result of CNT integration. At $R_c = 60\ \Omega$, σ_e/σ_m ranges from ~ 1.3 to 4.8 . However, with a large R_c and f (i.e., $R_c \geq 6\ \text{k}\Omega$ and $f > 20\%$), embedding CNTs in the composites raises the resistance instead, which is an undesirable effect. At $R_c \geq 6\ \text{k}\Omega$, σ_e/σ_m ranges from ~ 0.45 to 1 . With a large R_c and small f (i.e., $R_c \geq 6\ \text{k}\Omega$ and $f < 20\%$), no considerable effect is observed, leading to $0.93 < \sigma_e/\sigma_m < 1.04$. Most previously reported σ_e/σ_m are close to our FEM predictions with a high R_c (i.e., $R_c \geq 6\ \text{k}\Omega$), indicating that achieving small R_c , i.e., small density of defects at Cu - CNT contact, is extremely challenging for bulk material synthesis. There might be other factors influencing conductivities of bulk samples such as non-uniform orientation and distribution of CNTs and nonideal CNT morphologies, which is discussed later in detail. Based on the comparison with FEM, R_c of most bulk samples is estimated to be greater than $1\ \text{k}\Omega$. For example, for the Cu-CNT composite reported in [106], σ_e/σ_m is 0.8 at $f = 45\%$, indicating that R_c would be on the order of $1\ \text{k}\Omega$. For the Cu-CNT composites reported in all other works, R_c is approximately on the order of $10\ \text{k}\Omega$ and

above. To achieve σ_e greater than σ_m in CNT composites, discovering a scalable method to create high quality metal-CNT contacts would be the most important. Thus far, sub-k Ω R_c has been achievable only via low-throughput methods for creating strong interfacial adhesion between the CNTs and metal such as plasma enhanced chemical vapor deposition and transition metal-doped chemical vapor deposition [142,143].

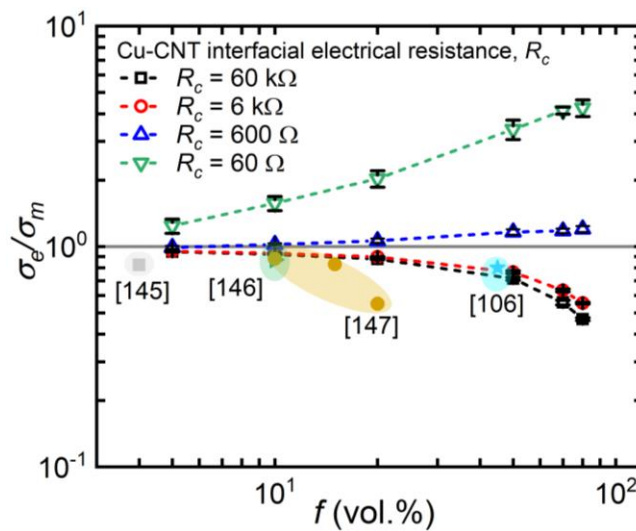


Figure 4.5. σ_e/σ_m as a function of f for different R_c . Hollow symbols with dashed lines correspond to FEM predictions. Solid symbols are σ_e/σ_m of Cu-CNT composites reported in previous works. The error bar represents the range between maximum and minimum conductivities.

The electrical transport at various f and R_c can be elucidated by visualizing the current density streamlines. Current density streamline is a curve everywhere tangent to an instantaneous current density field gradient, representing the directional flow path of

electrons through the domain. For visual clarity, the streamlines are generated only with four random starting points. Figures 4.6(a) and 4.6(b) depict current density streamlines overlaid in the electric field at $f=20\%$ with $R_c = 60 \Omega$ and $R_c = 60 \text{ k}\Omega$. The electric potential distribution does not uniformly decay along the field direction due to the CNT layout, resulting in nonuniform resistance distribution. The streamlines show that current seeks the least resistive path through the domain. With a small R_c , i.e., $R_c = 60 \Omega$, current preferably flows across as many CNTs as possible, since CNTs offer about 100 times greater conductivity than the copper matrix. However, with a large R_c , i.e., $R_c = 60 \text{ k}\Omega$, flowing across the CNTs does not provide the least resistive paths, leading to the current paths dominantly through the copper matrix. Figures 4.6(c) and 4.6(d) show the current density streamlines in electric fields at $f = 80\%$ with $R_c = 60 \Omega$ and $R_c = 60 \text{ k}\Omega$. With $R_c = 60 \Omega$, the dominant conduction path is formed through CNTs. With $R_c = 60 \text{ k}\Omega$, the current preferably flows through the Cu matrix. When CNTs are densely packed and R_c is large, the inhomogeneity of electric potential distribution increases as compared to when the CNTs are loosely packed and R_c is small. For example, with $f = 80\%$ and $R_c = 60 \text{ k}\Omega$, abrupt changes of electric potential occur in the locations where the copper matrix is completely isolated by surrounding CNTs.

Figure 4.7 presents k_e/k_m of Cu-CNT composite as a function of f predicted by FEM along with previously reported records. When the type I interfacial thermal resistance $R''_{t,c}$ is considerably small (i.e., $R''_{t,c} \leq 10^{-8} \text{ m}^2\text{K/W}$), k_e increases as f increases, implying that the CNT integration promotes the heat flow through the composite. At $R''_{t,c} = 10^{-10} \text{ m}^2\text{K/W}$, k_e/k_m ranges from 1 to ~ 4.8 . In contrast, when $R''_{t,c}$ is poorly regulated and f is large (i.e.,

$R''_{t,c} \geq 10^{-7} \text{ m}^2\text{K/W}$ and $f > 20\%$), embedded CNTs raise the composite resistance. At $R''_{t,c} = 10^{-7} \text{ m}^2\text{K/W}$, k_e/k_m ranges between $\sim 0.55\text{--}0.91$. With a large $R''_{t,c}$ and small f (i.e., $R''_{t,c} \geq 10^{-7} \text{ m}^2\text{K/W}$ and $f \leq 20\%$), integrating the CNTs has a negligible effect, resulting in $0.92 < k_e/k_m < 0.99$. When comparing the previous records with the FEM predictions, k_e/k_m of actual bulk samples are close to the FEM predictions with high $R''_{t,c}$ (i.e., $R''_{t,c} \geq 10^{-7} \text{ m}^2\text{K/W}$). This fact suggests that achieving $R''_{t,c}$ below $10^{-7} \text{ m}^2\text{K/W}$ range is yet to be realized in bulk samples. According to the FEM predictions, $R''_{t,c}$ of bulk samples are estimated to be on the order of $\geq 10^{-7} \text{ m}^2\text{K/W}$. For instance, k_e/k_m is 0.98 at $f = 45\%$ in a Cu-CNT composite reported in [107], which indicates that $R''_{t,c}$ would be on the order of $10^{-7} \text{ m}^2\text{K/W}$.

Heat flux streamlines are utilized to understand and visualize the underlying thermal transport at various f and $R''_{t,c}$. Heat flux streamline is a curve everywhere tangent to an instantaneous heat flux field gradient, representing the directional heat flow path through the domain. Figures 4.8(a) and 4.8(b) illustrate the heat flux streamlines overlaid in the temperature field, at $f = 20\%$ with $R''_{t,c} = 10^{-10} \text{ m}^2\text{K/W}$ and $R''_{t,c} = 10^{-7} \text{ m}^2\text{K/W}$. The inhomogeneity in the temperature field reflects the non-uniform resistance distribution owing to the CNT arrangement. The streamlines show that heat tends to follow the least resistive path through the domain. When $R''_{t,c}$ is small, i.e., $R''_{t,c} = 10^{-10} \text{ m}^2\text{K/W}$, heat prefers to flow through thermally conductive CNTs, since CNTs are about 7.5 times more conductive than copper. In contrast, with a large $R''_{t,c}$, i.e., $R''_{t,c} \geq 10^{-7} \text{ m}^2\text{K/W}$, copper becomes the dominant conduction medium as crossing the CNT boundaries is highly resistive. Thus, with large $R''_{t,c}$, heat flux streamlines are nearly aligned to field direction.

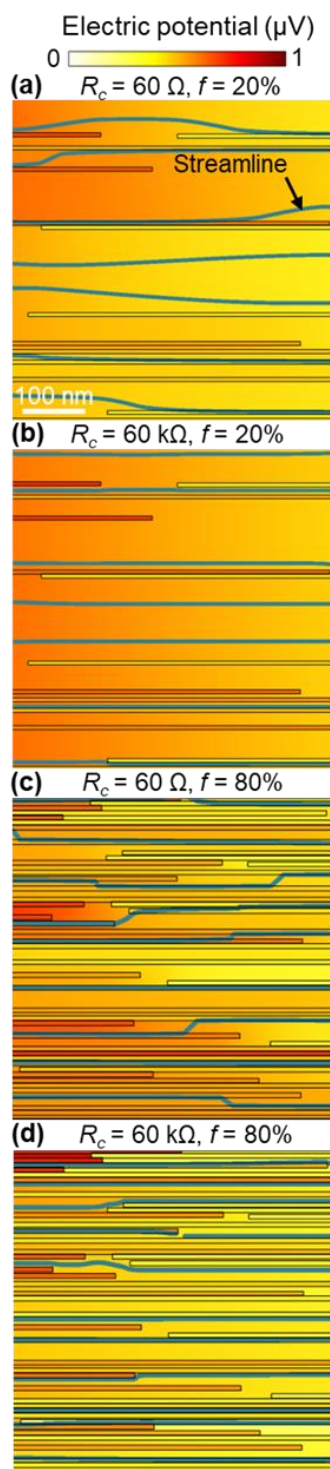


Figure 4.6. Electrical potential distributions in a Cu-CNT composite when (a) $f = 20\%$, $R_c = 60 \Omega$, (b) $f = 20\%$, $R_c = 60 \text{ k}\Omega$, (c) $f = 80\%$, $R_c = 60 \Omega$, and (d) $f = 80\%$, $R_c = 60 \text{ k}\Omega$.

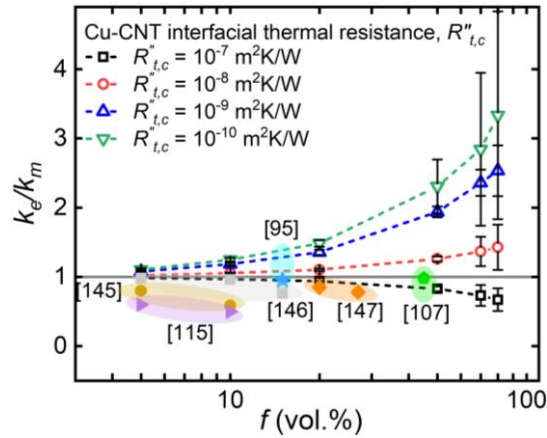


Figure 4.7. k_e/k_m as a function of f for different $R''_{t,c}$. Hollow symbols with dashed lines correspond to FEM predictions. Solid symbols are k_e/k_m of Cu-CNT composites reported in previous works. The error bar represents the range between maximum and minimum conductivities.

Figures 4.8(c) and 4.8(d) depict heat flux streamlines overlaid in the temperature map at $f = 80\%$, with $R''_{t,c} = 10^{-10} \text{ m}^2\text{K/W}$ and $R''_{t,c} = 10^{-7} \text{ m}^2\text{K/W}$. The dominant conduction medium is CNTs when $R''_{t,c}$ is $10^{-10} \text{ m}^2\text{K/W}$. The copper serves as the efficient heat medium when $R''_{t,c}$ is $10^{-7} \text{ m}^2\text{K}$. When $R''_{t,c}$ is large and CNTs are tightly packed, the inhomogeneity in temperature field is far more prominent compared to when $R''_{t,c}$ is small and CNTs are loosely packed. For instance, at $R''_{t,c} = 10^{-7} \text{ m}^2\text{K/W}$ and $f = 80\%$, steep changes in temperature occur in the locations where the resistive CNT boundaries entirely surround.

The mismatch between the 2D FEM predictions and experimental measurements shown in Fig. 4.5 and 4.7 implies the importance of composite features present in bulk materials such as nonuniform orientations and distribution of CNTs and nonideal CNT morphologies. The 2D FEM assumes an ideal composite morphology that simplifies the

bulk materials features. However, in the composites synthesized by powder metallurgy, CNTs agglomerate easily [145–148], which exacerbates with high fractions of CNTs [115,147]. The intense CNT agglomeration causes significant reduction in conductivities (< 40%) as compared to the conductivities of the ideal composite model. Another important feature is the CNT morphology, i.e., CNT tortuosity and orientations. If the actual CNT morphologies are close to the ideal morphology, the composites exhibit conductivities similar to the FEM estimations. For instance, the composites produced by template electrodeposition methods [106,107] contain relatively straight, aligned, and well-dispersed CNT bundles, the bulk conductivities presented small discrepancies (< 10%) between the conductivities of actual materials and ideal model. The Cu-CNT composite fabricated with powder-metallurgy involving particle-compositing process (high-pressure air blow on Cu and CNT powder mixture to disintegrate CNT clusters) exhibits smaller discrepancies (< 10%) to FEM predictions [66], compared to composite without the disintegration process [148]. Therefore, if the 2D FEM is employed to estimate the bulk material properties, the bulk material features determined by the synthesis methods must be considered to account for the discrepancy between the ideal and actual bulk composites. Despite the discrepancies against the actual materials, the 2D FEM serves an ideal model to predict the conductivities and understand the dominant conduction paths in Cu-CNT composites as a function of the interface resistances and CNT fractions. The 2D simplification of the composite morphology enables the modeling of CNT composites toward a considerably high CNT fraction. The average computation time for a 2D Cu-CNT model with $f = 80\%$ was ~395 mins using a six-core CPU (2.2 GHz).

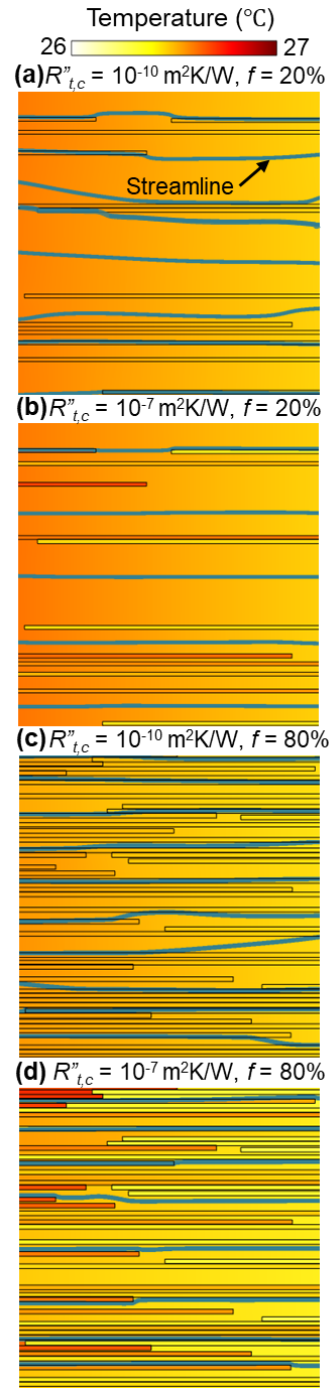


Figure 4.8. Temperature distributions in a Cu-CNT composite when (a) $f = 20\%$, $R''_{t,c} = 10^{-10} \text{ m}^2\text{W/K}$, (b) $f = 20\%$, $R''_{t,c} = 10^{-7} \text{ m}^2\text{W/K}$, (c) $f = 80\%$, $R''_{t,c} = 10^{-10} \text{ m}^2\text{W/K}$, and (d) $f = 80\%$, $R''_{t,c} = 10^{-7} \text{ m}^2\text{W/K}$.

4.6. Conclusions

This article reports a 2D FEM for the electrical and thermal conductivities of Cu-CNT composites. The 2D FEM accounts for the random distribution of CNTs and the resistances present at Cu-CNT and CNT-CNT interfaces. The model employs a simplified CNT morphology, i.e., straight CNTs aligned to the field direction, enabling the computation over a wide range of CNT fractions ($0 < f < 80\%$). In spite of the superior transport properties of CNTs, the interface resistances must be well regulated below a $1 \text{ k}\Omega$ (electrical) and $10^{-7} \text{ m}^2\text{K/W}$ (thermal) ranges for the composites to achieve greater conductivity than the copper matrix at $27 \text{ }^\circ\text{C}$. With the low levels of interface resistances, σ_e and k_e increases by ~ 5 times than Cu conductivity when CNTs are embedded by $f = 80\%$. FEM predictions were compared with previous records to understand the orders of interface resistances in reported bulk samples. The streamlines of current and heat flow visually elucidate that the dominant conduction paths are established through CNTs only with a low order of interface resistance. It must be noted that this FEM is for simplified and ideal composite designs. The actual bulk composites involve several defects including grain boundary dislocations, imperfections or voids within metal matrix, imperfections, or interstitial voids in CNTs and non-uniform dispersion of CNTs. All these factors degrade the transport properties through the bulk composite and must be accounted for actual bulk composites. The possible extension of our work would be (i) to precisely compare the simulated conductivities of Cu-CNT composites against experimental measurements and (ii) to extend our 2D FEM to include the possible defects which may effect the transport properties through the microstructure.

4.7. References

- [89] Dalmas, F., Dendievel, R., Chazeau, L., Cavail , J. Y., and Gauthier, C., 2006, “Carbon Nanotube-Filled Polymer Composites. Numerical Simulation of Electrical Conductivity in Three-Dimensional Entangled Fibrous Networks,” *Acta Mater.*, **54**(11), pp. 2923–2931.
- [90] Hone, J., Llaguno, M. C., Nemes, N. M., Johnson, A. T., Fischer, J. E., Walters, D. A., Casavant, M. J., Schmidt, J., and Smalley, R. E., 2000, “Electrical and Thermal Transport Properties of Magnetically Aligned Single Wall Carbon Nanotube Films,” *Appl. Phys. Lett.*, **77**(5), pp. 666–668.
- [91] Wang, H., Zhang, Z. H., Hu, Z. Y., Song, Q., and Yin, S. P., 2018, “Interface Structure and Properties of CNTs/Cu Composites Fabricated by Electroless Deposition and Spark Plasma Sintering,” *Mater. Res. Express*, **5**(1).
- [92] Ghorbani-Asl, M., Bristowe, P. D., and Koziol, K., 2015, “A Computational Study of the Quantum Transport Properties of a Cu-CNT Composite,” *Phys. Chem. Chem. Phys.*, **17**(28), pp. 18273–18277.
- [93] Hjortstam, O., Isberg, P., S derholm, S., and Dai, H., 2004, “Can We Achieve Ultra-Low Resistivity in Carbon Nanotube-Based Metal Composites?,” *Appl. Phys. A Mater. Sci. Process.*, **78**(8), pp. 1175–1179.
- [94] Sundaram, R. M., Sekiguchi, A., Sekiya, M., Yamada, T., and Hata, K., 2018, “Copper/Carbon Nanotube Composites: Research Trends and Outlook,” *R. Soc. Open Sci.*, **5**(11).
- [95] Chu, K., Guo, H., Jia, C., Yin, F., Zhang, X., Liang, X., and Chen, H., 2010, “Thermal Properties of Carbon Nanotube-Copper Composites for Thermal Management Applications,” *Nanoscale Res. Lett.*, **5**(5), pp. 868–874.
- [96] Xu, Z., and Buehler, M. J., 2009, “Nanoengineering Heat Transfer Performance at Carbon Nanotube Interfaces,” *ACS Nano*, **3**(9), pp. 2767–2775.
- [97] Zhao, J., Rao, Z., and Li, Y., 2015, “Thermal Performance of Mini-Channel Liquid Cooled Cylinder Based Battery Thermal Management for Cylindrical Lithium-Ion Power Battery,” *Energy Convers. Manag.*, **103**, pp. 157–165.
- [98] Huang, H., Liu, C., Wu, Y., and Fan, S., 2005, “Aligned Carbon Nanotube Composite Films for Thermal Management,” *Adv. Mater.*, **17**(13), pp. 1652–1656.
- [99] Yoo, S. J., Han, S. H., and Kim, W. J., 2013, “A Combination of Ball Milling and High-Ratio Differential Speed Rolling for Synthesizing Carbon Nanotube/Copper Composites,” *Carbon N. Y.*, **61**, pp. 487–500.
- [100] Khaleghi, E., Torikachvili, M., Meyers, M. A., and Olevsky, E. A., 2012, “Magnetic Enhancement of Thermal Conductivity in Copper-Carbon Nanotube

Composites Produced by Electroless Plating, Freeze Drying, and Spark Plasma Sintering,” *Mater. Lett.*, **79**, pp. 256–258.

- [101] Park, Cheol ; Wilkinson, John ; Banda, Sumanth ; Ounaies, Zoubeida ; Wise, Kristopher E ; Sauti, Godfrey ; Lillehei, Peter T ; Harrison, J. S., 2006, “Aligned Single-Wall Carbon Nanotube Polymer Composites Using an Electric Field,” *J. Polym. Sci.*, **44**(12), pp. 1751–1762.
- [102] Choi, E. S., Brooks, J. S., Eaton, D. L., Al-Haik, M. S., Hussaini, M. Y., Garmestani, H., Li, D., and Dahmen, K., 2003, “Enhancement of Thermal and Electrical Properties of Carbon Nanotube Polymer Composites by Magnetic Field Processing,” *J. Appl. Phys.*, **94**(9), pp. 6034–6039.
- [103] Dai, J., Wang, Q., Li, W., Wei, Z., and Xu, G., 2007, “Properties of Well Aligned SWNT Modified Poly (Methyl Methacrylate) Nanocomposites,” *Mater. Lett.*, **61**(1), pp. 27–29.
- [104] Wang, Q., Dai, J., Li, W., Wei, Z., and Jiang, J., 2008, “The Effects of CNT Alignment on Electrical Conductivity and Mechanical Properties of SWNT/Epoxy Nanocomposites,” *Compos. Sci. Technol.*, **68**(7–8), pp. 1644–1648.
- [105] Gupta, P., Rajput, M., Singla, N., Kumar, V., and Lahiri, D., 2016, “Electric Field and Current Assisted Alignment of CNT inside Polymer Matrix and Its Effects on Electrical and Mechanical Properties,” *Polymer (Guildf.)*, **89**, pp. 119–127.
- [106] Subramaniam, C., Yamada, T., Kobashi, K., Sekiguchi, A., Futaba, D. N., Yumura, M., and Hata, K., 2013, “One Hundred Fold Increase in Current Carrying Capacity in a Carbon Nanotube-Copper Composite,” *Nat. Commun.*, **4**, pp. 1–7.
- [107] Subramaniam, C., Yasuda, Y., Takeya, S., Ata, S., Nishizawa, A., Futaba, D., Yamada, T., and Hata, K., 2014, “Carbon Nanotube-Copper Exhibiting Metal-like Thermal Conductivity and Silicon-like Thermal Expansion for Efficient Cooling of Electronics,” *Nanoscale*, **6**(5), pp. 2669–2674.
- [108] Sun, S., Mu, W., Edwards, M., Mencarelli, D., Pierantoni, L., Fu, Y., Jeppson, K., and Liu, J., 2016, “Vertically Aligned CNT-Cu Nano-Composite Material for Stacked through-Silicon-via Interconnects,” *Nanotechnology*, **27**(33).
- [109] Subramaniam, C., Sekiguchi, A., Yamada, T., Futaba, D. N., and Hata, K., 2016, “Nano-Scale, Planar and Multi-Tiered Current Pathways from a Carbon Nanotube-Copper Composite with High Conductivity, Ampacity and Stability,” *Nanoscale*, **8**(7), pp. 3888–3894.
- [110] Liu, L., Ma, W., and Zhang, Z., 2011, “Macroscopic Carbon Nanotube Assemblies: Preparation, Properties, and Potential Applications,” *Small*, **7**(11), pp. 1504–1520.
- [111] Jorio, A., Saito, R., Hertel, T., Weisman, R. B., Dresselhaus, G., and Dresselhaus,

- M. S., 2018, “Carbon Nanotube Photophysics,” (April 2004).
- [112] Zeng, W., Shu, L., Li, Q., Chen, S., Wang, F., and Tao, X. M., 2014, “Fiber-Based Wearable Electronics: A Review of Materials, Fabrication, Devices, and Applications,” *Adv. Mater.*, **26**(31), pp. 5310–5336.
- [113] Xue, Q. Z., 2006, “Model for the Effective Thermal Conductivity of Carbon Nanotube Composites,” *Nanotechnology*, **17**(6), pp. 1655–1660.
- [114] Nan, C. W., Shi, Z., and Lin, Y., 2003, “A Simple Model for Thermal Conductivity of Carbon Nanotube-Based Composites,” *Chem. Phys. Lett.*, **375**(5–6), pp. 666–669.
- [115] Kim, K. T., Eckert, J., Liu, G., Park, J. M., Lim, B. K., and Hong, S. H., 2011, “Influence of Embedded-Carbon Nanotubes on the Thermal Properties of Copper Matrix Nanocomposites Processed by Molecular-Level Mixing,” *Scr. Mater.*, **64**(2), pp. 181–184.
- [116] Zhong, H., and Lukes, J. R., 2006, “Interfacial Thermal Resistance between Carbon Nanotubes: Molecular Dynamics Simulations and Analytical Thermal Modeling,” *Phys. Rev. B - Condens. Matter Mater. Phys.*, **74**(12), pp. 1–10.
- [117] Chu, K., Jia, C. C., and Li, W. S., 2013, “Thermal Conductivity Enhancement in Carbon Nanotube/Cu-Ti Composites,” *Appl. Phys. A Mater. Sci. Process.*, **110**(2), pp. 269–273.
- [118] Wilhite, P., Vyas, A. A., Tan, J., Tan, J., Yamada, T., Wang, P., Park, J., and Yang, C. Y., 2014, “Metal-Nanocarbon Contacts,” *Semicond. Sci. Technol.*, **29**(5).
- [119] Zuo, T., Li, J., Gao, Z., Zhang, L., Da, B., Zhao, X., Ding, F., Li, S., Yang, Y., and Xiao, L., 2020, “Enhanced Electrical Conductivity and Hardness of Copper/Carbon Nanotubes Composite by Tuning the Interface Structure,” *Mater. Lett.*, **280**, pp. 1–4.
- [120] Zuo, T., Li, J., Gao, Z., Wu, Y., Zhang, L., Da, B., Zhao, X., and Xiao, L., 2020, “Simultaneous Improvement of Electrical Conductivity and Mechanical Property of Cr Doped Cu/CNTs Composites,” *Mater. Today Commun.*, **23**(January).
- [121] Kong, J., Zhang, C. Y., and Cheng, X., 2013, “Novel Cu-Cr Alloy Matrix CNT Composites with Enhanced Thermal Conductivity,” *Appl. Phys. A Mater. Sci. Process.*, **112**(3), pp. 631–636.
- [122] Milowska, K. Z., Ghorbani-Asl, M., Burda, M., Wolanicka, L., Čatić, N., Bristowe, P. D., and Koziol, K. K., 2017, “Breaking the Electrical Barrier between Copper and Carbon Nanotubes,” *Nanoscale*, **9**(24), pp. 8458–8469.
- [123] Nie, J., Jia, C., Jia, X., Zhang, Y., Shi, N., and Li, Y., 2011, “Fabrication, Microstructures, and Properties of Copper Matrix Composites Reinforced by Molybdenum-Coated Carbon Nanotubes,” *Rare Met.*, **30**(4), pp. 401–407.

- [124] Cola, B. A., Xu, J., and Fisher, T. S., 2009, "Contact Mechanics and Thermal Conductance of Carbon Nanotube Array Interfaces," *Int. J. Heat Mass Transf.*, **52**(15–16), pp. 3490–3503.
- [125] Nirmalraj, P. N., Lyons, P. E., De, S., Coleman, J. N., and Boland, J. J., 2009, "Electrical Connectivity in Single-Walled Carbon Nanotube Networks," *Nano Lett.*, **9**(11), pp. 3890–3895.
- [126] Gong, S., Zhu, Z. H., and Haddad, E. I., 2013, "Modeling Electrical Conductivity of Nanocomposites by Considering Carbon Nanotube Deformation at Nanotube Junctions," *J. Appl. Phys.*, **114**(7), pp. 1–10.
- [127] Narayanunni, V., Gu, H., and Yu, C., 2011, "Monte Carlo Simulation for Investigating Influence of Junction and Nanofiber Properties on Electrical Conductivity of Segregated-Network Nanocomposites," *Acta Mater.*, **59**(11), pp. 4548–4555.
- [128] Shkolnik, K., and Chalivendra, V., 2018, "Numerical Studies of Electrical Contacts of Carbon Nanotubes-Embedded Epoxy under Tensile Loading," *Acta Mech.*, **229**(1), pp. 99–107.
- [129] Li, B. J., Ma, P. C., Chow, W. S., To, C. K., Tang, B. Z., and Kim, J., 2007, "Correlations between Percolation Threshold , Dispersion State , and Aspect Ratio of Carbon Nanotubes," pp. 3207–3215.
- [130] Coleman, J. N., Curran, S., Dalton, A. B., Davey, A. P., Mccarthy, B., Blau, W., and Barklie, R. C., 1998, "Percolation-Dominated Conductivity in a Conjugated-Polymer-Carbon-Nanotube Composite," *Phys. Rev. B*, **58**(12), pp. 7492–7495.
- [131] Allaoui, A., Hoa, S. V., Evesque, P., and Bai, J. B., 2009, "Electronic Transport in Carbon Nanotube Tangles under Compression: The Role of Contact Resistance," *Scr. Mater.*, **61**(6), pp. 628–631.
- [132] Rahman, R., and Servati, P., 2014, "Efficient Analytical Model of Conductivity of CNT / Polymer Composites for Wireless Gas Sensors," (c), pp. 1–12.
- [133] Foygel, M., Morris, R. D., Anez, D., French, S., and Sobolev, V. L., 2005, "Theoretical and Computational Studies of Carbon Nanotube Composites and Suspensions: Electrical and Thermal Conductivity," *Phys. Rev. B - Condens. Matter Mater. Phys.*, **71**(10), pp. 1–8.
- [134] Deng, F., and Zheng, Q. S., 2008, "An Analytical Model of Effective Electrical Conductivity of Carbon Nanotube Composites," *Appl. Phys. Lett.*, **92**(7), pp. 90–93.
- [135] Bagchi, A., and Nomura, S., 2006, "On the Effective Thermal Conductivity of Carbon Nanotube Reinforced Polymer Composites," *Compos. Sci. Technol.*, **66**(11–12), pp. 1703–1712.

- [136] Mohiuddin, M., and Hoa, S. V., 2013, “Estimation of Contact Resistance and Its Effect on Electrical Conductivity of CNT/PEEK Composites,” *Compos. Sci. Technol.*, **79**, pp. 42–48.
- [137] Che, Jianwei ; Çagin, Tahir ; Goddard III, W. A., 2000, “Thermal Conductivity of Carbon Nanotubes,” *Nanotechnology*, **11**(2), pp. 65–69.
- [138] Wang, J., Xie, H., Xin, Z., and Li, Y., 2010, “Increasing the Thermal Conductivity of Palmitic Acid by the Addition of Carbon Nanotubes,” *Carbon N. Y.*, **48**(14), pp. 3979–3986.
- [139] Li, S., Yu, Z., Rutherglen, C., and Burke, P. J., 2004, “Electrical Properties of 0.4 Cm Long Single-Walled Carbon Nanotubes,” *Nano Lett.*, **4**(10), pp. 2003–2007.
- [140] Kane, A. A., Sheps, T., Branigan, E. T., Apkarian, V. A., Cheng, M. H., Hemminger, J. C., Hunt, S. R., and Collins, P. G., 2009, “Graphitic Electrical Contacts to Metallic Single-Walled Carbon Nanotubes Using Pt Electrodes,” *Nano Lett.*, **9**(10), pp. 3586–3591.
- [141] Matsuda, Y., Deng, W. Q., and Goddard, W. A., 2010, “Contact Resistance for ‘End-Contacted’ Metal-Graphene and Metal-Nanotube Interfaces from Quantum Mechanics,” *J. Phys. Chem. C*, **114**(41), pp. 17845–17850.
- [142] Tong, T., Zhao, Y., Delzeit, L., Majumdar, A., and Kashani, A., 2017, “Multiwalled Carbon Nanotube/Nanofiber Arrays as Conductive and Dry Adhesive Interface Materials,” *Proc. ASME 2004 3rd Integr. Nanosyst. Conf. Des. Synth. Appl.*, pp. 1–6.
- [143] Park, M., Cola, B. A., Siegmund, T., Xu, J., Maschmann, M. R., Fisher, T. S., and Kim, H., 2006, “Effects of a Carbon Nanotube Layer on Electrical Contact Resistance between Copper Substrates,” *Nanotechnology*, **17**(9), pp. 2294–2303.
- [144] Lim, S. C., Jang, J. H., Bae, D. J., Han, G. H., Lee, S., Yeo, I. S., and Lee, Y. H., 2009, “Contact Resistance between Metal and Carbon Nanotube Interconnects: Effect of Work Function and Wettability,” *Appl. Phys. Lett.*, **95**(26), pp. 1–4.
- [145] Akbarpour, M. R., Mousa Mirabad, H., Alipour, S., and Kim, H. S., 2020, “Enhanced Tensile Properties and Electrical Conductivity of Cu-CNT Nanocomposites Processed via the Combination of Flake Powder Metallurgy and High Pressure Torsion Methods,” *Mater. Sci. Eng. A*, **773**(September 2019), p. 138888.
- [146] Pan, Y., Xiao, S. Q., Lu, X., Zhou, C., Li, Y., Liu, Z. W., Liu, B. W., Xu, W., Jia, C. C., and Qu, X. H., 2019, “Fabrication, Mechanical Properties and Electrical Conductivity of Al₂O₃ Reinforced Cu/CNTs Composites,” *J. Alloys Compd.*, **782**, pp. 1015–1023.
- [147] Daoush, W. M., Lim, B. K., Mo, C. B., Nam, D. H., and Hong, S. H., 2009,

“Electrical and Mechanical Properties of Carbon Nanotube Reinforced Copper Nanocomposites Fabricated by Electroless Deposition Process,” *Mater. Sci. Eng. A*, **513–514(C)**, pp. 247–253.

- [148] Nie, J. H., Jia, C. C., Jia, X., Li, Y., Zhang, Y. F., and Liang, X. B., 2012, “Fabrication and Thermal Conductivity of Copper Matrix Composites Reinforced by Tungsten-Coated Carbon Nanotubes,” *Int. J. Miner. Metall. Mater.*, **19(5)**, pp. 446–452.

5. DATA-DRIVEN MODELING OF TRANSPORT MECHANISMS IN COPPER-CARBON NANOTUBE COMPOSITES

5.1. Introduction

Copper (Cu) is by far the most widely used conductive material in electronics, aviation, construction and power transmission lines. The progressive miniaturization and sophistication of high-power density devices demand copper alternatives to facilitate efficient electrical and thermal transport. Cu-carbon nanotube (CNT) composites are theoretically estimated to be superior electrical and thermal conductors to Cu at room temperature (27 °C) [94]. The conductivities of Cu-CNT composites are strongly influenced by CNT morphologies, i.e., CNT volume fraction and interfacial resistance at Cu-CNT and CNT-CNT interfaces. The electrical and thermal transport in CNT composites manifests in complex physics, which is extremely challenging to represent with closed-form models. Existing physics-based models, e.g., finite element model (FEM), are highly compute intensive, predominantly due to the extremely fine mesh required for CNTs and CNT-CNT interfaces.

Deep learning, a class of machine learning (ML), is applied in various scientific research areas to readily discover features from high-dimensional unstructured data (e.g., images, audio clips) [149,150]. For some nonlinear transport problems accompanied with complex physics in composites, deep learning algorithms interpret nonlinear patterns of data to classify or predict outputs without iteratively calculating the governing physical equations; thus, demanding lower computational costs than numerical simulation

techniques [151–155]. Thus, researchers are actively investigating data driven deep learning analysis as an alternate modeling approach in composites [156–159].

5.2. Background Review and Problem Statement

With the recent rapid development of ML methods, there has been growing interest in predicting the nanocomposite attributes without performing compute-intensive simulations. A previous study used convolutional neural networks (CNN) to predict thermal conductivity in composite materials [156]. 1500 composite material structures with volume fractions up to 30% were generated using the quartet structure generation set and effective thermal conductivities were calculated using the lattice Boltzmann method (LBM). The predicted results using CNN were found close to LBM with root mean square error (RMSE) of 1.9%. A past study utilized artificial neural networks (ANN) to determine the most favorable bridging alloying atom in Aluminum-CNT composite [157]. ANN was trained with 357 examples from literature for various alloying elements along with their strengthening efficiencies. The strengthening efficiencies approximated by the ML model were comparable to those of experiments with accuracy greater than 90%. Another research used ANN to predict the multiaxial strain-sensing response of CNT-polymer composites [158]. The ML model employed physics-based FEM at microscale to generate 15000 examples to train ANN and approximated the macro-scale strain responses in CNT-polymer composites with accuracy of 99.65%. One previous record developed and trained the Gaussian Process Regression (GPR) model to predict the tensile strength in CNT-polymers nanocomposites [159]. The training data was collected from the available

literature with 23 different polymers, combined with 22 CNT incorporating methods and 20 CNT modifications. The GPR model exhibited strong performance in predicting the tensile strength of CNT-polymer composites with training and validation accuracy of greater than 91%.

In this article, a convolutional neural network (CNN) is presented that infers the electrical and thermal conductivity of Cu-CNT composites at room temperature (27 °C) when an input data describing the stochastic distribution of CNTs, CNT volume fraction and Cu-CNT interfacial resistance is provided. The CNN model learns the important features from the images of Cu-CNT networks to predict the conductivities. To improve the accuracy of the CNN model, the influence of various hyperparameters such as learning rate, batch size and number of neurons in hidden layers is investigated. The trained CNN can serve as a surrogate model for Cu-CNT composite systems if the morphology of CNT network can be expressed in two-dimensional (2D) image format. For example, if the 2D images of Cu-CNT composites that sharply visualize the boundaries of CNTs, obtained either from computational modeling or processed microscopic images, are available, the trained CNN can rapidly examine the composite properties before conducting the expensive FEM or actual measurements.

5.3. Training Data Generation

Training data is generated by creating the 2D stochastic Cu-CNT networks and simulating their electrical and thermal conductivities. A 2D finite element model (FEM) is used for the simulation that accounts for the CNT volume fractions, f , Cu-CNT interfacial

resistances, and CNT-CNT interfacial resistances arising from the van der Waals interaction between two closely spaced CNTs. Since full details of FEM are available elsewhere [160], only a minimal description follows. The 2D FEM model employs a simplified CNT morphology, i.e., straight CNTs aligned to the field direction, enabling the simulations of CNT networks with high volume fractions (up to 80%) at reduced computational costs. Several studies have reported that aligned, straightened CNTs exhibit enhanced electrical and thermal conductivities than entangled, randomly oriented CNTs [9,100,102–104]. Figure 5.1(a) illustrates some examples of Cu–CNT network models with various f . The 2D composite consists of non–overlapping CNTs (length 500 nm and width 10 nm) which are randomly distributed in the Cu matrix. Figure 5.1(b) shows the electrical and thermal boundary conditions used in FEM, which represent the following configurations: (i) steady-state electrical conduction and (ii) heat conduction without internal heat generation. For electrical analysis, a potential difference, ΔV , of 1 μV is applied across the domain of length, L . For thermal analysis, the initial domain temperature is set to 27 $^{\circ}\text{C}$ and the temperature difference across the domain, ΔT , is kept at 1 $^{\circ}\text{C}$. At Cu-CNT interfaces, the interfacial electrical resistance (R_c) and interfacial thermal resistance ($R''_{t,c}$) are defined in the ranges of $R_c = 20 \Omega - 20 \text{ k}\Omega$ and $R''_{t,c} = 10^{-10} \text{ m}^2\text{K/W} - 10^{-7} \text{ m}^2\text{K/W}$. The FEM estimates the electrical potential and temperature distributions in the Cu-CNT composite that are needed for the computation of effective electrical conductivity (σ_e) and thermal conductivity (k_e). The conductivities are normalized by the Cu matrix electrical conductivity ($\sigma_{Cu} = 0.58 \times 10^8 \text{ S/m}$)[160] and thermal conductivity ($k_{Cu} = 401 \text{ W/mK}$)[160] at room temperature. The training dataset is collected using FEM

simulations and data augmentation. Figure 5.2 summarizes the data preparation process. First, 20 different images of Cu-CNT networks with random CNT distributions were generated for each target CNT fraction. Since 6 CNT volume fractions (*i.e.*, $f = 5\%$, 10% , 20% , 50% , 70% and 80%) were considered, in total, 120 Cu-CNT network images were created. Three-channel RGB images of Cu-CNT networks were converted into single-channel gray images to reduce the size of data. The information of Cu-CNT interfacial resistance was encoded in the Cu-CNT network image through a color code. The color intensity of the Cu domain was chosen by assigning grayscale intensities representing R_c or $R''_{t,c}$, while CNT regions

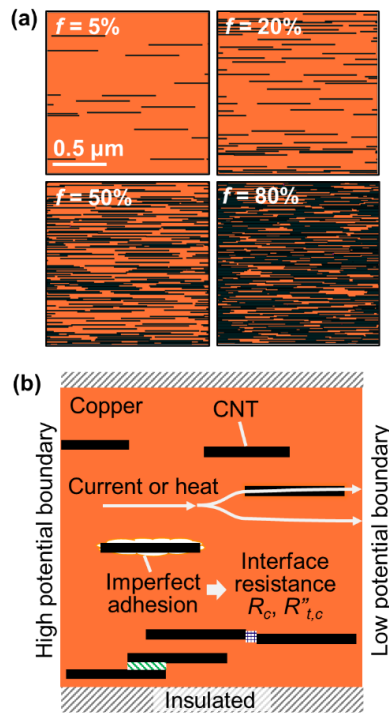


Figure 5.1. (a) Schematics of Cu-CNT networks with various CNT fractions f , (b) Schematic of a Cu-CNT network with boundary conditions. The patterned bars represent the side-to-side and end-to-end CNT-CNT interfacial resistance.

were represented by white color (i.e., pixel intensity of 255). The pixel intensity of the Cu domain was varied as 0, 63, 129, 163 to encode four different levels of R_c and $R''_{t,c}$. The total number of images after the color modification is increased to 480. The amount of training data was amplified using a simple image transformation technique, similar to a previous work [151]. As shown in Fig. 5.1(c), the original images were flipped in three ways: (i) horizontal, (ii) vertical and (iii) diagonal flips. The transformed Cu-CNT networks were assumed to possess identical conductivities to their original Cu-CNT network. With the data augmentation, the total number of Cu-CNT network models is increased to 1920. Finally, the Cu-CNT network images and tabulated electrical and thermal conductivities from FEM simulations were paired as the training dataset.

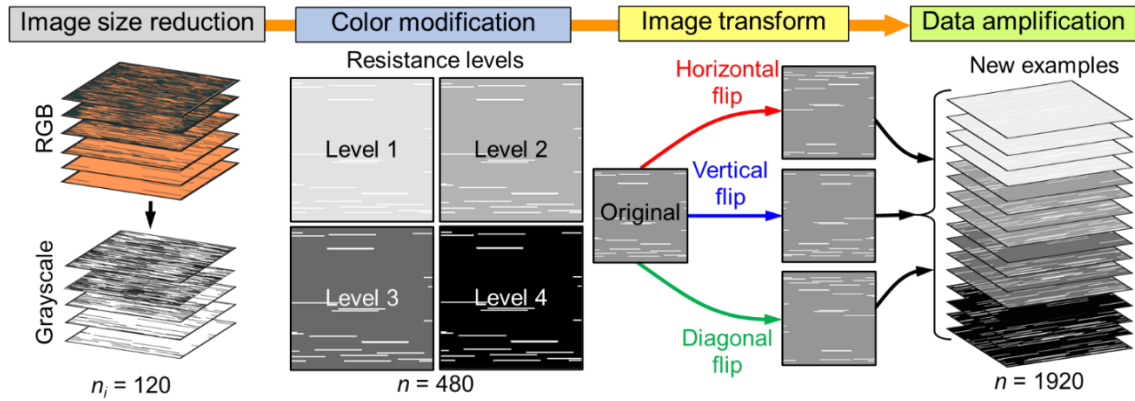


Figure 5.2. Schematic for the data preparation. The image data size of Cu-CNT networks is reduced by converting RGB scale into grayscale. The Cu-CNT interfacial resistance is encoded by the selection of Cu domain color intensity. The resistance levels are defined as follows. Level 1: $R_c = 20 \text{ k}\Omega$ or $R''_{t,c} = 10^{-7} \text{ m}^2\text{K/W}$, Level 2: $R_c = 2 \text{ k}\Omega$ or $R''_{t,c} = 10^{-8} \text{ m}^2\text{K/W}$, Level 3: $R_c = 200 \text{ }\Omega$ or $R''_{t,c} = 10^{-9} \text{ m}^2\text{K/W}$, and Level 4: $R_c = 20 \text{ }\Omega$ or $R''_{t,c} = 10^{-10} \text{ m}^2\text{K/W}$.

m²K/W. The images are flipped horizontally, vertically, and diagonally to amplify the training dataset by four folds.

5.4. Convolutional Neural Network

Convolutional neural network (CNN) is a class of deep neural networks which is widely-used in image recognition tasks with remarkable success [161]. There are several CNN models with different structures successfully applied for image recognition such as AlexNet [162], ResNet [163], LeNet-5 [164], etc. The CNN model outperforms other machine learning algorithms in terms of non-linear function approximation and the ability to extract and articulate data features [165]. Thus, compared to conventional artificial neural networks such as multilayer perceptron and feed-forward networks, the CNN significantly reduces the computational demands when processing high-dimensional image information due to the feature parameter sharing and dimensionality reduction. Figure 5.3 shows the architecture of our CNN model obtained through hyperparameter tuning which is discussed in the next section. The CNN model consists of an input layer (i.e., Cu-CNT network), an output layer (i.e., predicted conductivities) and 6 hidden layers. The input layer is a single channel Cu-CNT network image, equivalent to a 228×228×1 matrix. The image size was chosen to retain high resolution and capture minuscule details of CNT networks, particularly at high CNT fractions. A convolution layer is added to generate feature maps from the input layer. The convolutional layer contains a series of 3×3 kernels which are convoluted with inputs to extract features while preserving the spatial relationships between image pixels. The batch normalization layer is added after every convolution layer

to normalize and standardize the inputs between 0 to 1. A rectified linear unit activation (ReLU) layer is added to prevent the vanishing gradient problem, allowing the model to learn faster with improved stability. To down-sample the input feature map, a pooling layer with a filter size of 2 and stride of 2 is inserted after every activation layer. The pooling layer applies an average pooling operation in a prescribed filter size and abstracts the input feature maps, reducing the low-level features while extracting high-order features. After 6 iterations of hidden layers, a fully connected layer takes all the outputs in the previous layer and connects them to its single neuron, i.e., a one-dimensional feature vector. The feature vector represents the major features of the original input and can be used to establish the regression model for the electrical or thermal conductivities.

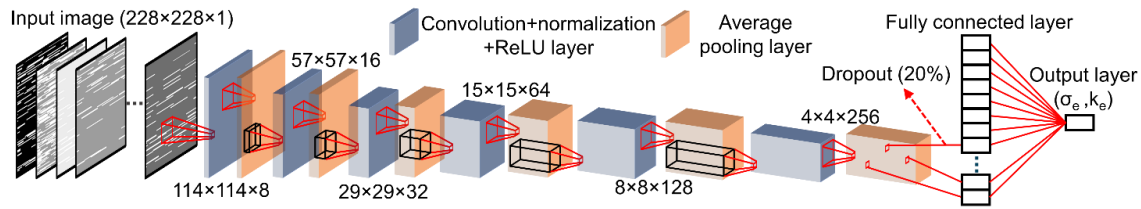


Figure 5.3. The architecture of CNN to approximate the effective electrical and thermal conductivities of Cu-CNT networks. σ_e denotes the effective electrical conductivity and k_e denotes the effective thermal conductivity.

To train the CNN model, stochastic gradient descent (SGD) algorithm is used. SGD is one of the popular iterative optimization techniques for determining weights that minimize the errors in neural networks. SGD calculates the gradients on small randomized subsets of the training set, called minibatch. The gradient is calculated in small-steps called

learning rate which determines the moving step size from one point to the next point with a negative gradient. After a full forward and backward pass on the complete training dataset, i.e., 1 epoch, the model weights are updated. By testing with a minibatch in the range of 5 - 20 and learning rate in the range of 10^{-2} - 10^{-7} , we selected an optimal minibatch size as 20, a learning rate as 10^{-3} and epochs as 400. The learning rate was dropped by a factor of 0.1 after every 150 epochs, allowing the model to learn an optimal set of weights. The model training begins by initiating the kernel parameters using Gaussian initialization method which extracts the features of the Cu-CNT network. The kernel parameters are optimized according to the Euclidean loss function, $(1/n) \sum_{i=1}^n ||y_i - y_i' ||^2$, which calculates the square sum of the difference between the two training outputs, i.e., predictive value, y_i and known value, y_i' . The loss function is subsequently minimized after each iteration by updating the parameters.

5.5. Results and Discussion

The number of neurons in hidden layers was adjusted to balance the model accuracy and training time. The coefficient of determination (R^2) was employed to quantitatively examine the model accuracy. Table 5.1 summarizes the R^2 of training dataset (R^2_{Train}) and the validation dataset (R^2_{Valid}) along with model training time as a function of neurons in each convolution layer for both σ_e/σ_{Cu} and k_e/k_{Cu} predictions. The model training was performed on a graphic card (Nvidia RTX A6000) with 48 GB memory. In general, as the number of neurons, equivalently the depth of output volume, increases, both training and validation R^2 increases along with the cost of additional training time. In our experiment,

the number of neurons used in case 4 provided the highest R^2_{Train} and $R^2_{Valid} (\geq 0.94)$ with a training time of ~ 3 minutes. The model R^2 was not improved by further increasing the number of neurons as seen in case 5. Therefore, the number of neurons in each layer was chosen to be 16, 32, 64, 128 and 256 for all subsequent CNN training. The CNN was trained to predict the electrical and thermal conductivities of the Cu-CNT networks over wide range of interfacial resistances, i.e., $R_c = 20 \Omega - 20 \text{ k}\Omega$ and $R''_{t,c} = 10^{-10} \text{ m}^2\text{K/W} - 10^{-7} \text{ m}^2\text{K/W}$.

Table 5.1. CNN model R^2 and training time obtained with various hidden layer neurons.

Case	Neurons in each layer	σ_e/σ_{Cu} predictions			k_e/k_{Cu} predictions		
		R^2_{Train}	R^2_{Valid}	Time (second)	R^2_{Train}	R^2_{Valid}	Time (second)
1	10, 20, 30, 40, 50, 60	0.83	0.79	110	0.83	0.71	114
2	20, 40, 60, 80, 100, 120	0.87	0.86	144	0.89	0.87	152
3	40, 80, 120, 160, 200, 240	0.96	0.91	280	0.94	0.90	299
4	8, 16, 32, 64, 128, 256	0.99	0.98	170	0.99	0.98	175
5	16, 32, 64, 128, 256, 512	0.99	0.94	352	0.98	0.92	322

Figure 5.4 compares the CNN model approximations and FEM predictions for σ_e/σ_{Cu} . Overall, the training of CNN was successful with $R^2_{Train} \geq 0.99$, and the trained CNN was able to accurately predict the unseen Cu-CNT network models with $R^2_{Valid} \geq 0.98$. Note that training the CNN with 1920 Cu-CNT models took only ~ 3 minutes. With this training cost, the CNN model can estimate the conductivity of an unseen Cu-CNT network within 1 second, whereas the FEM requires ~ 155 minutes on average for the same task. Such characteristics of the CNN model suggest that the deep learning approach is a promising

method when it is necessary to rapidly and repetitively estimate the properties of stochastic composite materials if the training dataset, *i.e.*, images of composite materials and corresponding properties, is available. The training and validation datasets were designed to include diversified examples with various CNT fractions and interfacial resistances. The diversity in training data critically affects whether the neural network is able to overcome the bias or not. In our dataset, σ_e/σ_{Cu} ranges from 0.08 to 10.45 and k_e/k_{Cu} ranges from 0.15 to 4.25 as shown in Fig. 5.4. For the data generated with a large interfacial resistance (*i.e.*, $R_c = 20 \text{ k}\Omega$ and $R''_{t,c} = 10^{-7} \text{ m}^2\text{K/W}$), the Cu-CNT composites with high f (*i.e.*, $f \geq 50\%$) possessed effective conductivities that were smaller than that of copper (*i.e.*, $0 < \sigma_e/\sigma_{Cu}$, $k_e/k_{Cu} < 0.5$). For the examples with a Large R_c , $R''_{t,c}$ and small f (*i.e.*, $f < 20\%$), the effective conductivities were close to unity. When the interfacial resistance is small (*i.e.*, $R_c = 20 \Omega$ and $R''_{t,c} = 10^{-10} \text{ m}^2\text{K/W}$), the examples with high f (*i.e.*, $f \geq 50\%$) exhibited effective conductivities that were greater than that of copper (*i.e.*, $7.5 < \sigma_e/\sigma_{Cu} < 11$ and $2 < k_e/k_{Cu} < 4.5$). By combining various levels of f , R_c and $R''_{t,c}$, the dataset incorporated the examples having effective conductivities similar to previously reported Cu-CNT composites [95,106,107,115,145–148].

The method introduced in this article demonstrates that the deep neural networks can rapidly approximate the complex relation between the morphology of fiber composites and their electrical and thermal transport properties. The introduced approach will be useful for the researchers who need a surrogate model for fiber composite systems that estimates the composite properties before the expensive finite element simulations or actual measurements. Thus, the application of the introduced approach for inferring the properties

of actual composite materials can be an extension of this work. Since the images of Cu-CNT composites used in this work showed the shapes of CNTs distinctly without any blurriness, the CNN readily recognized the layouts of CNTs and made predictions accurately. For the application of the introduced approach to actual materials, it will be necessary to acquire microscopic images of the samples from various parts and process the images to extract the morphology of CNT network similar to Fig. 5.1(a) while eliminating the background image features.

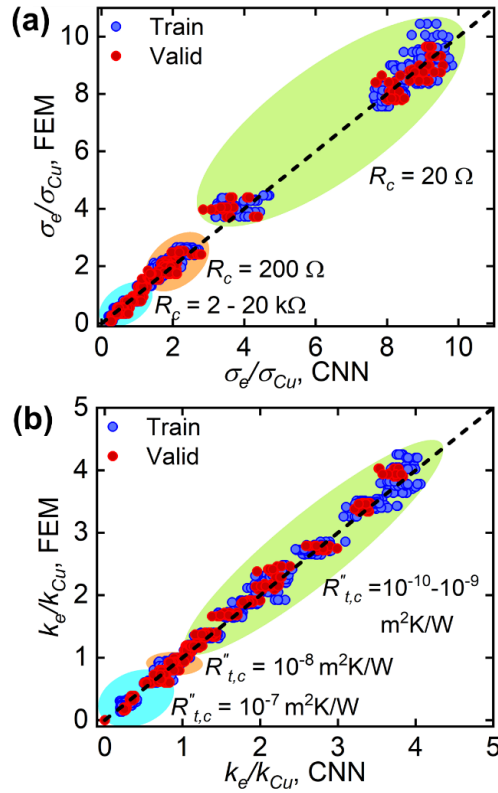


Figure 5.4. Comparison between CNN approximations and FEM predictions for (a) effective electrical conductivities with $R^2_{Train} = 0.991$, $R^2_{Valid} = 0.982$, and (b) effective thermal conductivities with $R^2_{Train} = 0.992$, $R^2_{Valid} = 0.986$.

5.6. Conclusions

This work reports a CNN that is trained to approximate the effective electrical and thermal conductivities of stochastic Cu-CNT networks when their 2D images are provided as inputs. The CNN architecture and hyperparameters were optimized to make approximations with $R^2 > 0.98$. Despite the complex and nonlinear transport mechanism, the CNN predicted for unseen Cu-CNT networks of various CNT volume fractions and Cu-CNT interfacial resistances with the R^2 greater than 98%. To provide a variety of learnable examples in CNN without performing additional FEM simulations, a simple image augmentation technique was used to diversify the training dataset by 4-folds. A possible extension of this work is to investigate the potential of CNN or other deep learning methods as rapid prediction models for microscopic images of fabricated bulk-scale Cu-CNT networks or other composite materials.

6. NON-LINEAR TRANSPORT MECHANISM MODELING IN CARBON-NANOTUBE FIBERS

6.1. Introduction

State-of-the-art carbon nanofibers (CNF) possess unique combination of properties including excellent mechanical, electrical and thermal properties which compete with both high strength fibers and metallic conductors. The excellent properties of CNF make them attractive for high-end fields such as military equipment, robotics, aeronautics, and space elevators [160,166,167]. CNF are touted to become next-generation fiber due to its superior flexibility and low density [168]. The macroscopic bulk properties of CNF are controlled by quality and type of constituent CNT bundles and their connectivity [166,167]. However, it is extremely challenging to retain inherent properties of individual carbon nanotubes (CNT) during CNF production and several research efforts have been made on improving the CNF synthesis methods [166,169,170].

There are two main methods for fiber production: liquid- and solid-state spinning. Natural fibers such as wool and cotton are formed by solid-state spinning, whereas most synthetic fibers are created from a concentrated, viscous liquid. Direct-spun CNT fibers and films can achieve high tensile strength (2–10 GPa) with relatively long-length constituent CNTs (~1 mm) but have low electrical conductivity (1–3 MS/m) because of their low orientation and packing density [166,167]. By contrast, solution-spun fibers are processed into shorter CNTs (~12 μm) but exhibit both high tensile strength (2–5 GPa) and electrical conductivity (~11 MS/m) [167,168]. Among the many parameters for producing

high-performance CNT fibers, the alignment and packing of the fibers can be improved by subsequent processes.

In CNT fibers, a number of structural methods exist to improve the fiber properties. CNT fiber consists of a hierarchical structure in which CNTs form a bundle, and multiple bundles form the CNT fiber [171]. CNT fibers therefore contain numerous voids and defects on the inter-bundle (tens to hundreds of nanometer scale) and intra-bundle (less than a few nanometers scale), which are generated during fiber formation, and the macroscopic properties of the obtained fiber are highly dependent on the size and amount of defects that are present [166,167,171]. Within a CNT bundle, improving the interaction between adjacent nanotubes is critical for high-performance CNT fibers [167]. By regulating the CNT aspect ratio (L/d , L is CNT length and d is CNT diameter), the CNT-CNT interaction can be improved in the fiber [167,171,172], and the significance of CNT aspect ratio has been mentioned in several past literatures. In general, polygonal CNTs bring greater advantages in the packing of CNT arrays than circular structures. For example, in case of electrical conductivity, higher aspect ratio may provide higher conductivity of CNT fibers owing to the reduction of junctions between CNTs per unit fiber length [167].

Theoretical analysis and simulation are powerful techniques for investigating the performance of CNT fibers, and they can provide significant insights regarding the effects of various processing and structural parameters, such as CNT length, diameter, fiber twist angle, etc. To date, a few analyses and simulations have been performed to investigate the

electrical and thermal conductivities of CNT fibers as well as the morphology of their constituent CNTs.

In this chapter, we propose a two-dimensional (2D) finite element model (FEM) to study the electrical and thermal conductivities of CNT fibers while accounting for the various CNT aspect ratios, range of intrinsic CNT electrical and thermal conductivities, and range of contact resistances at CNT-CNT interfaces. Although the 2D approximations and simplifications for the CNT morphologies would compromise the accuracy in simulations, these assumptions enable to simulate the complex transport phenomena in the CNT composites with void fraction $< 0.1\%$.

6.2. Finite Element Model

The FEM based on three-dimensional CNT morphologies may provide the realistic transport properties. However, as the individual single walled CNTs (SWCNTs) are extremely thin (~ 1.5 nm [160]), the incurring computational costs can be extremely large due to highly fine mesh requirements for SWCNTs. This may inhibit modelling the long CNT fibers in 3D analysis. In order to reduce the computational demands, we have made few approximations which allow us to utilize 2D FEM to model the transport mechanism through sufficiently long CNT fibers (up to $60 \mu\text{m}$) and void fraction $< 0.1\%$ in a reasonable computation time.

The irregular shaped multiwall CNTs are common within a CNT bundle due to fabrication constraints [160]. In order to rapidly create CNT bundles with negligible void fraction ($< 0.1\%$), we have approximated CNTs of uniform hexagonal planar cross-section.

Within a CNT bundle, there is different proportion of single-walled, double-walled and multi-walled CNTs [167]. We have assumed that all the CNTs are single-walled in the fiber.

To reduce 3D analysis to 2D, we have assumed that the electrical and thermal transport through an individual CNT is only influenced by adjacent CNTs on each side. A 3D FEM is developed which can be used to simulate the transport behavior through two row CNT bundle. Figure 6.1 shows the 3D CNT fiber with uniform hexagonal planar cross section. The voids between each CNT row in a bundle can be varied, along with the CNT-CNT interfacial resistances. For the sake of simplicity, we have assumed that there are no intra-bundle voids between CNTs. Using 3D FEM, we can simulate the electrical and thermal transport through two row CNT bundle and approximate the resultant conductivities of the bundle as conductivity of a single CNT in the 2D FEM.

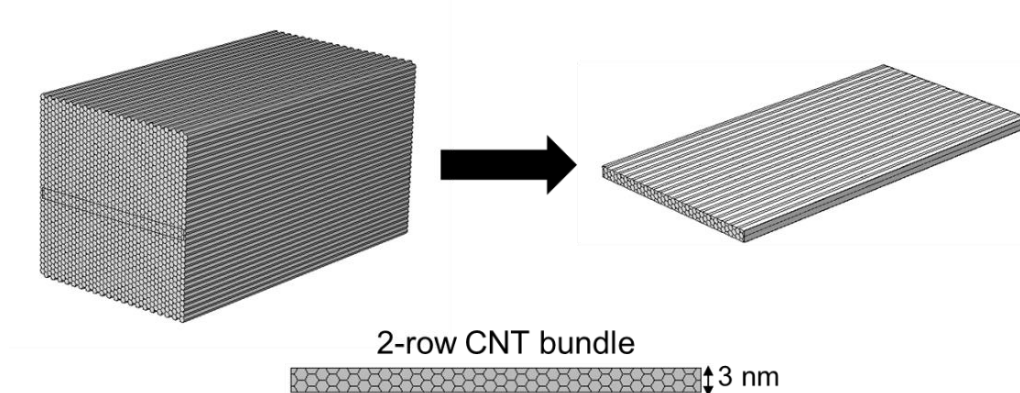


Figure 6.1: 2-row CNT bundle extracted from 3D schematic of CNT fiber

To understand the electrical and thermal transports, our model focuses on parallel (ribboned) and aligned CNTs in the CNT fiber. Figure 6.2(a) shows a 2D schematic of CNT fiber of length, L , and diameter, d , are aligned to the field direction. In the CNT fiber, two types of contact between CNTs are possible [1] as illustrated in Fig. 6.2(b). Type I contact represents the CNT end-to-end contact resistance. Type II contact represents the side-to-side contact resistance between two CNTs. Both types of contact resistances are important when CNTs are separated by a distance less than vdWs spacing (~ 1 nm). The CNT-CNT contact resistance exists at the CNT interconnects where CNTs are within the van der Waals (vdWs) distance. If the CNTs are in such extreme proximity, electrons and phonons can flow across the CNTs, but the electrical and thermal transports are affected by the interface resistances. The ballistic phonon and electron propagation within each CNT are scattered at the interface resulting in notably large CNT-CNT interfacial thermal resistance (up-to $\sim 10^{-7}$ m²K/W) and interfacial electrical resistance (up-to $\sim 10^4$ k Ω) [160].

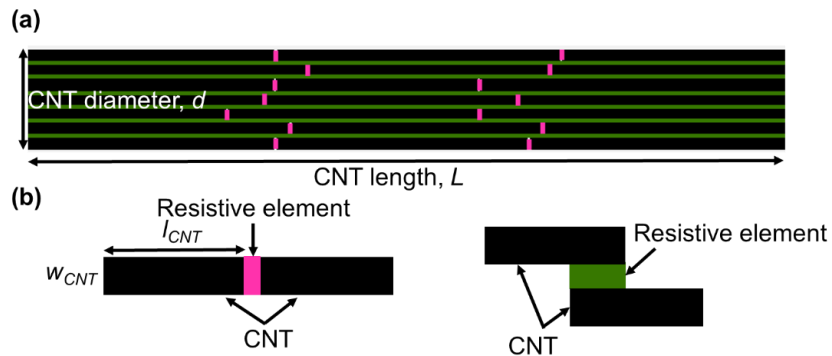


Figure 6.2: (a) Schematic of 2D CNT fiber layout, and (b) resistive element for type-I (end-to-end) CNT interface (left) and resistive element for type-II (side-to-side) CNT interface.

To simulate the transport phenomena in 2D CNT fiber, our FEM follows the three steps: (i) randomly distributing CNTs, (ii) creating resistive elements at type I and II contacts, and (iii) computing the electrical potential and temperature fields in the fiber.

To generate the CNT layout, we have chosen CNT dimensions corresponding to DX-2 fiber in a previous work [1], i.e., CNT length, l_{CNT} , of 2300 nm and CNT width, w_{CNT} , of 1.5 nm. As CNT-CNT interfaces are created at different locations depending on various synthesis parameters, it is imperative to generate a random layout of CNTs, in such a way that CNT interfaces in each are generated at different locations relative to other rows. For this purpose, the length of first CNT in each row is randomly chosen between 1800 nm – 2300 nm, while all the remaining CNTs in each row have fixed length of 2300 nm. The vertical spacing between each adjacent row is fixed to 0.2 nm ($<vdws$), while the end-to-end spacing between CNTs in each row is randomly varied between 0.3 nm to 1 nm ($<vdws$). The resistive elements are added in the spacings and assigned the CNT-CNT interfacial resistances (or equivalently CNT-CNT interfacial conductivities). The simulations are conducted for two separate configurations: (i) steady-state electrical conduction and (ii) heat conduction without internal heat generation. For electrical analysis, a potential difference across the domain, ΔV , is 1 μV . For thermal analysis, the initial domain temperature is set to 27 °C. A temperature difference across the domain, ΔT , is 1 °C. The boundaries that are perpendicular to the field direction are electrically and thermally insulated.

6.3. Domain Independence Analysis

The FEM solutions must be independent of computational domain size, which can be achieved by creating a stochastic system including enough number of CNTs in both axial and transverse direction. The domain independence analysis can be categorized into two cases. Case 1: the CNT length, L , is kept constant (equivalent to $L = 3l_{CNT}$), while the CNT width, d , is varied between 20 nm to 50 nm. Case 2: the CNT width, d , is used from case 1 and CNT length, L , is varied between ranges of $3l_{CNT} - 6l_{CNT}$. For each geometric parameter, the simulations are repetitively performed on 10 CNT fiber layouts with different CNT distributions, and their results are averaged to obtain a representative result for a certain geometric parameter. The FEM simulation solves the 2D electrical and heat conduction equations in CNT fiber models to estimate the electric potential and temperature distributions. The resulting current density, J , and conductive heat flux, q'' , at various x locations are computed. The CNT fiber effective electrical conductivity, σ_e , is calculated by a relation $\sigma_e = \int J dy |_x / \Delta V$. The effective thermal conductivity, k_e , is calculated by a relation $k_e = \int q'' dy |_x / \Delta T$. For domain independence analysis, we will only show the effective thermal conductivities as the deductions are analogous to effective electrical conductivities.

Figure 6.3(a) shows k_e as a function of simulation domain width, d (case 1). As domain width is increased from 20 nm to 50 nm, the variation in conductivities is less than 10%. Between $d = 40$ nm and $d = 50$ nm, the variation in conductivities is less than 3%. Therefore, it is recommended to use domain width of 40 nm. Figure 6.3(b) shows k_e as a function of simulation domain length, L (case 2) using $d = 40$ nm. Between $L = 4 \times l_{CNT}$ and

$L = 5 \times l_{CNT}$, the variation in conductivities is less than 8%. Therefore, it is recommended to use domain length of $L = 4 \times l_{CNT}$ (i.e., 4 CNTs per row). Collectively, we deduce that the domain independence results may be obtained with domain length of $L = 4 \times l_{CNT} = 9200$ nm and domain width of 40 nm. Furthermore, a grid test was conducted to determine the minimum grid size ensuring accuracy and computational efficiency. The subsequent simulations use a minimum grid size of 1000 nm, maximum grid size of 2000 nm, curvature factor of 0.5, maximum element growth of 2000 nm and narrow regions resolution of 0.2. The average meshing time per design is ~ 90 mins.

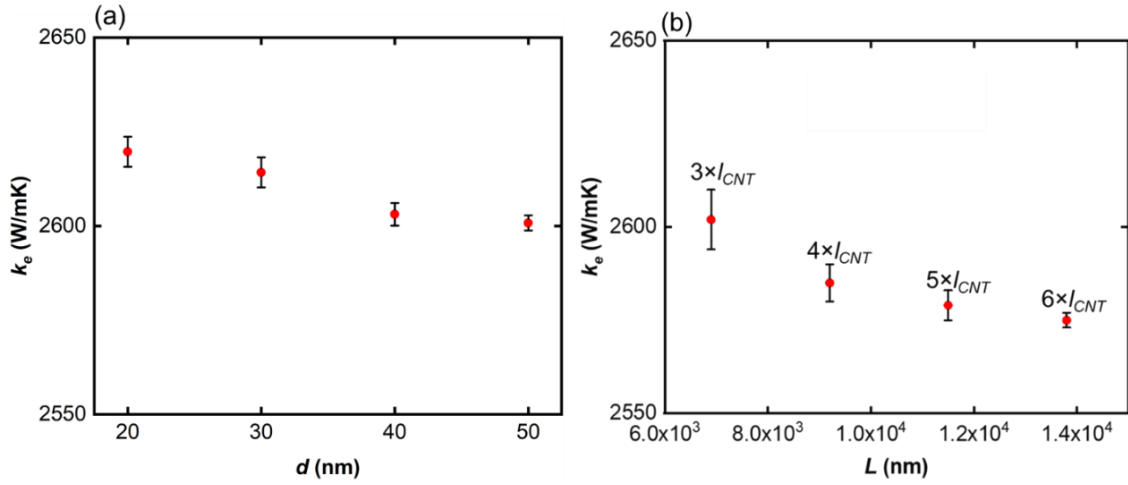


Figure 6.3: (a) Effective thermal conductivity as a function of CNT fiber width, d , and (b) effective thermal conductivity as a function of CNT fiber length, L .

6.4. Results and Discussion

This section presents the simulation results obtained for CNT aspect ratio, $\alpha = l_{CNT} / w_{CNT} = 1000 - 10,000$, intrinsic CNT electrical conductivity, $\sigma_{CNT} = 7.1 \times 10^6$ S/m - 7.1×10^9 S/m, and intrinsic CNT thermal conductivity, $k_{CNT} = 500 - 1000$ W/mK. Also, we

varied CNT-CNT interfacial electrical conductivity ($\sigma_{CNT-CNT} = 10^2 - 10^5$ S/m), and CNT-CNT interfacial thermal conductivity ($k_{CNT-CNT} = 0.1 - 10$ W/mK) to study interfacial resistance magnitude impact on effective conductivities of CNT fiber. Figure 6.4 shows σ_e as a function of CNT aspect ratio along with two different magnitudes of CNT-CNT interfacial electrical conductivities. As the aspect ratio is increased from 1000 – 10,000, the number of CNTs per row are reduced from 40 – 4, which in turn leads to lesser type-I interfaces (same as number of CNTs per row – 1). As α is increased, the effective conductivities are also improved as current flow is predominantly less obstructed by type-I interfaces.

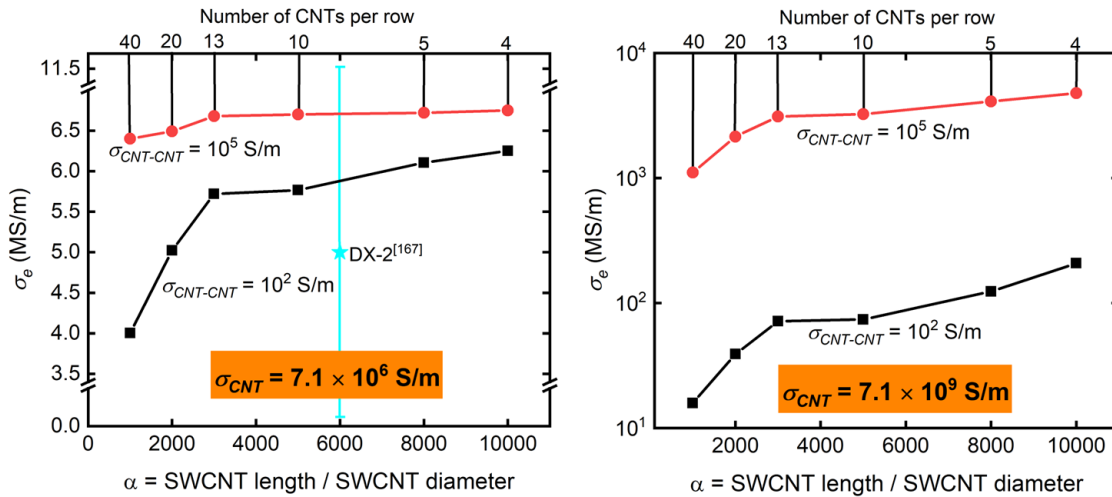


Figure 6.4: Effective electrical conductivity as a function of CNT aspect ratio for (a) $\sigma_{CNT} = 7.1 \times 10^6$ S/m and (b) $\sigma_{CNT} = 7.1 \times 10^9$ S/m.

When intrinsic CNT conductivities are low, the presence of greater number of poorly regulated CNT-CNT interfaces significantly deteriorate the effective conductivities (upto 44%), as shown in Fig. 6.4(a). For low conductive CNTs, decreasing the CNT aspect

ratio does not have drastic impact on the effective conductivities (upto 10% only) for highly regulated CNT-CNT interfaces. In contrast, for highly conductive CNTs, increasing the number of CNT-CNT interfaces lead to severe deterioration of effective conductivities (upto 85% for $\sigma_{CNT-CNT} = 10^2$ S/m, and upto 2 orders for $\sigma_{CNT-CNT} = 10^5$ S/m) as shown in Fig. 6.4(b). We also compared the CNT fiber electrical conductivity reported in a previous work [1] with our simulation results corresponding to $\alpha = 6000$. It implies that the reported CNT fiber's intrinsic electrical conductivity might have been in the order of 10^6 S/m, while the CNT-CNT interfacial electrical conductivity might be in the range of $10^{-1} - 10^6$ S/m.

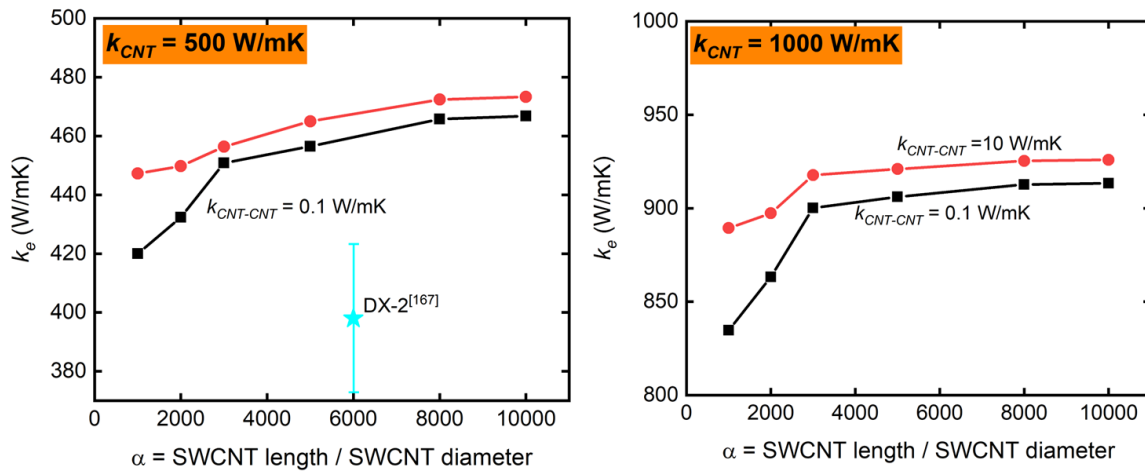


Figure 6.5: Effective thermal conductivity as a function of CNT aspect ratio for (a) $k_{CNT} = 500$ W/mK and (b) $k_{CNT} = 1000$ W/mK.

Figure 6.5 shows k_e as a function of CNT aspect ratio and two levels of CNT-CNT interfacial thermal conductivities. The underlying physics of thermal case is analogous to electrical analysis. For low thermally conductive CNTs, increased number of CNT-CNT

interfaces by reduced CNT aspect ratio adds more thermal barrier to the heat flow, leading to drop in effective conductivities by upto 16% for poorly regulated interfaces ($k_{CNT-CNT} = 0.1$ W/mK) and upto 10% for well-regulated interfaces ($k_{CNT-CNT} = 10$ W/mK), as shown in Fig. 6.5(a). For highly thermally conductive CNTs, increasing the number of CNT-CNT interfaces lead to deterioration of effective conductivities (upto 16% for $k_{CNT-CNT} = 0.1$ W/mK, and upto 11% for $k_{CNT-CNT} = 10$ W/mK) as shown in Fig. 6.5(b). We also compared the CNT fiber thermal conductivity reported in previous work [1] with our FEM approximations at $\alpha = 6000$. The comparison hints towards significantly high CNT-CNT interfacial thermal resistances (equivalently interfacial thermal conductivity in order of 10^{-3} W/mK) as the actual thermal conductivities are extremely poor in fabricated CNT fibers.

6.5. Conclusions

Our work reports a two-dimensional (2D) finite element model (FEM) for approximating electrical and thermal conductivities in CNT fibers. First, a three-dimensional (3D) finite element model was developed to approximate conductivities in a two-row single-walled CNT bundle (each CNT 1.5 nm wide) having planar hexagonal cross-section. This approximation allowed us to reduce the 3D analysis to 2D with an assumption that the CNT distribution along the transverse direction of fiber is uniform. We developed a 2D FEM which incorporates the obtained two-row CNT bundle's conductivity as an individual CNT's (3 nm wide) conductivity. In 2D FEM, the computational domain size independent results were obtained by varying the domain length (6900 – 13,800 nm) and domain width (20 – 50 nm). The domain size of 9200 nm (equivalent to $4 \times$ CNT

length) and width 40 nm was chosen as it presented < 8% fluctuation in the estimated electrical and thermal conductivities. Using 2D FEM, stochastic CNT distribution along fiber axis in sufficiently long CNT fibers (up to 60 μm) was possible as a function of various CNT aspect ratios (1000 – 10,000), intrinsic CNT conductivities (for electrical: $7 \times 10^6 - 7 \times 10^9$ S/m, for thermal: 500 – 1000 W/mK) and CNT-CNT interface conductivities (for electrical: $10^2 - 10^5$ S/m, for thermal: 0.1 – 10 W/mK) with a reasonable computational time (< 2 hrs per design using 2.2 GHz 6 core processor). Based on FEM estimations, the electrical and thermal conductivities can be significantly improved by increasing the aspect ratio of CNTs in the fiber. When the CNT-CNT interface resistance is poorly regulated, effective conductivities are deteriorated by decreasing the CNT aspect ratio (up to 2 orders for electrical, and 17% for thermal). Conversely, when the CNT-CNT interface is well regulated, decreasing the aspect ratio do not have drastic effect on effective conductivities (up to 11% for electrical and 10% for thermal). The presented framework for the FEM utilize reduced computational resources and demonstrated the potential of numerical simulations in understanding the complex transport mechanism through long CNT fibers.

7. CONCLUSION AND FUTURE WORK

7.1. Conclusions

This work explored the morphology control effect on the thermal, electrical and thermo-electrical properties of advanced materials such as thermo-electric generators, copper-carbon nanotube composites and carbon nanotube fibers. Using finite element modeling corroborated with experimental findings and comparisons, this research attempted to provide insights into harnessing superior bulk attributes by carefully controlling the material morphologies using advanced manufacturing techniques.

First, we propose novel additively manufacturable thermoelectric (TE) leg morphologies, which were not achievable before due to constraints in traditional manufacturing methods. This allowed the fabrication of TE cellular architectures which provided 26% more thermo-electric generation efficiency and offered 25% density reduction compared to traditional TE rectangular shaped legs. The FEM predictions were found to be in good agreement with experimental findings, with accuracy $> 90\%$. This innovative TE leg structure offers promising potential to replace traditional TE legs in high-end applications where maximum performance is needed in limited physical space. Moreover, we also explored the potential of utilizing multiple BiSbTe-based materials within a single TE device. Our FEM and experimental findings indicated record-high efficiency of 8.7% in 3D printed compositionally segmented leg with optimized material distribution and composition. By utilizing compositionally engineered all-inorganic BiSbTe-based inks, TE legs with unrestricted geometric design potential was possible without any electrical or thermal losses at the interfaces. This capability expanded the

operating temperature range of the TE generators from room temperature up to 250 °C. The research findings present a novel and cost-effective approach to the design of high-performance segmented TE generators, thereby offering new opportunities for the TE research community.

This research also offers a fundamental insight into the transport mechanisms in carbon nanotubes (CNT)-based composites. For the first time, computationally efficient FEM was formulated to model the electrical and thermal properties in CNT composites by simultaneously considering the stochastic CNT distribution, CNT fractions and interfacial resistances. The study used a simplified CNT morphology with straight CNTs aligned to the field direction, allowing the computation of a wide range of CNT fractions (up to 80%). The results indicated that interface resistances must be well regulated to achieve greater conductivity than the copper matrix at 27 °C. With low levels of interface resistances, the conductivity of the composites increases by ~5 times than Cu conductivity when CNTs were embedded at CNT fraction of 80%. The FEM predictions were compared with previous records to understand the orders of interface resistances in reported bulk samples. The current and heat flow streamlines visually elucidated that the dominant conduction paths were established through CNTs only with a low order of interface resistance. The proposed FEM model can help researchers to estimate the theoretical maximum possible conductivities if the CNT morphologies are carefully controlled, along with appreciable insight into the energy transport physics involved in these composites. Moreover, we also proposed data-driven modeling technique to rapidly approximate conductivities in composites using convolutional neural networks (CNN). Using FEM based generated

training data, CNN was trained and tuned by optimizing different hyper-parameters. Despite the complex and nonlinear transport mechanism, the CNN rapidly predicted for unseen composite layouts of various CNT volume fractions and interfacial resistances with the R^2 greater than 98%. Overall, this research may contribute towards development of efficient and accurate prediction models for composite materials without iteratively solving compute intensive physical governing equations.

Finally, we presented a pseudo 2D FEM utilizing reduced computational resources to model complex transport mechanisms in carbon nanotube fibers (CNF) with large aspect ratios (up to 10,000). Using the 2D FEM, we were able to simulate stochastic CNT distributions along fiber axis in sufficiently long CNT fibers (up to 60 μm) as a function of various CNT aspect ratios, intrinsic CNT conductivities, and CNT-CNT interface conductivities, with a reasonable computational time (<2 hrs per design using 2.2 GHz 6 core processor). The FEM estimations demonstrated that the electrical and thermal conductivities can be significantly improved by increasing the CNT aspect ratios in the fiber. However, if the CNT-CNT interface resistances were poorly regulated, effective conductivities were deteriorated with decreased aspect ratios (up to 2 orders for electrical, and 17% for thermal). Conversely, when the CNT-CNT interface was well regulated, decreasing the aspect ratio posed no drastic effect on effective conductivities (up to 11% for electrical and 10% for thermal).

7.2. Future Work

This section discusses the possible future work which can be extended from this research pertaining to advanced materials in the field of mechanical engineering.

For example, the ability to 3D print thermoelectric (TE) legs has opened new avenues for optimizing the design of TE legs for different applications. Unlike some other energy conversion systems, such as piezoelectric or triboelectric generators, there is generally no trade-off between the mechanical strength and power output of a TEG. The power output of a TEG is primarily determined by the temperature difference across the device and the efficiency of the thermoelectric materials used. While the mechanical strength of a TEG may not be a significant factor in determining its power output, it can be important for its reliability and durability. In certain applications, such as in space missions or remote power generation, the TEG may be subjected to harsh environmental conditions or physical stresses. In such cases, designing the TEG with sufficient mechanical strength is crucial to ensure its longevity and performance. With the ability to fabricate complex shapes and geometries, it is now possible to topologically optimize TE leg designs based on various loading conditions to improve their mechanical and thermo-electric performance. One potential area where this technology could have a significant impact is in aerospace applications. In aerospace, weight is a critical factor, and any reduction in weight can lead to improved fuel efficiency and overall performance. By topologically optimizing TE legs, it may be possible to reduce their weight while maintaining or even improving their thermo-electric performance. This could have a significant impact on the overall efficiency of aerospace systems. Another potential application for topologically

optimized TE legs is in the field of renewable energy. As the world seeks to transition to a more sustainable energy system, there is a growing need for more efficient and cost-effective energy conversion technologies. TE legs have the potential to play a significant role in this transition by converting waste heat into usable electrical energy. By topologically optimizing TE leg designs, it may be possible to improve their efficiency and reduce their cost, making them more competitive with other energy conversion technologies.

As the field of nanocomposites continues to advance, one area of future research that holds immense promise is the development of neural networks to rapidly predict the transport properties of actual CNT based composites. While previous work has shown the potential of neural networks in predicting these properties for ideal 2D CNT morphologies, the accuracy of these predictions can be limited for actual composites in which CNTs are unaligned, entangled and form clusters. One potential solution to this problem is to initiate a collaboration to develop and open-source the training data for actual CNT-based composite images. This could involve partnering with researchers and industry experts to generate a database of high-quality images of CNT-based composites, along with detailed information about their transport properties. This data could then be made publicly available for use in training neural networks, enabling researchers and engineers around the world to build more accurate predictive models. It would provide a valuable resource for researchers and engineers working in the field of nanocomposites, enabling them to develop more accurate predictive models and accelerate the pace of innovation. Additionally, by making this data freely available, it would encourage greater collaboration

and knowledge sharing within the field, facilitating the development of new ideas and approaches.

The field of mechanical engineering has seen a significant transformation in recent years due to the advent of artificial intelligence (A.I) and machine learning (ML). ML has become an indispensable tool for solving complex engineering problems, and its integration has led to new and innovative solutions in areas such as design optimization, materials science, and manufacturing. As the world continues to embrace A.I-based solutions, there is a growing need to educate and train the next generation of engineers and scientists on the potential applications of ML in mechanical engineering. One potential future work is to develop education materials such as tutorials and webinars that can be used to teach students about ML in mechanical engineering. The aim of these education materials would be to spread awareness among young students towards applications of ML in mechanical engineering related research problems. The materials can be developed for students of all levels, from high school to graduate school. Developing educational materials and open-source software and tools can help to accelerate the pace of research and development, leading to new and innovative solutions in mechanical engineering.

REFERENCES

- [1] Sanyal, M. K., Datta, A., and Hazra, S., 2002, “Morphology of Nanostructured Materials,” *Pure Appl. Chem.*, **74**(9), pp. 1553–1570.
- [2] Dandekar, P., Kuvadia, Z. B., and Doherty, M. F., 2013, “Engineering Crystal Morphology,” *Annu. Rev. Mater. Res.*, **43**(March), pp. 359–386.
- [3] Hwang, J., Ejsmont, A., Freund, R., Goscianska, J., Schmidt, B. V. K. J., and Wuttke, S., 2020, “Controlling the Morphology of Metal-Organic Frameworks and Porous Carbon Materials: Metal Oxides as Primary Architecture-Directing Agents,” *Chem. Soc. Rev.*, **49**(11), pp. 3348–3422.
- [4] Samothrakitis, S., Raventós, M., Čapek, J., Larsen, C. B., Grünzweig, C., Tovar, M., Garcia-Gonzalez, M., Kopeček, J., Schmidt, S., and Strobl, M., 2020, “Grain Morphology Reconstruction of Crystalline Materials from Laue Three-Dimensional Neutron Diffraction Tomography,” *Sci. Rep.*, **10**(1), pp. 1–7.
- [5] Yi, T., Li, L., and Kim, C. J., 2000, “Microscale Material Testing of Single Crystalline Silicon: Process Effects on Surface Morphology and Tensile Strength,” *Sensors Actuators, A Phys.*, **83**(1), pp. 172–178.
- [6] Lu, T. J., 1999, “Heat Transfer Efficiency of Metal Honeycombs,” *Int. J. Heat Mass Transf.*, **42**(11), pp. 2031–2040.
- [7] Jung, H., Yu, S., Bae, N. S., Cho, S. M., Kim, R. H., Cho, S. H., Hwang, I., Jeong, B., Ryu, J. S., Hwang, J., Hong, S. M., Koo, C. M., and Park, C., 2015, “High Through-Plane Thermal Conduction of Graphene Nanoflake Filled Polymer Composites Melt-Processed in an L-Shape Kinked Tube,” *ACS Appl. Mater. Interfaces*, **7**(28), pp. 15256–15262.
- [8] Choo, S., Ejaz, F., Ju, H., Kim, F., Lee, J., Yang, S. E., Kim, G., Kim, H., Jo, S., Baek, S., Cho, S., Kim, K., Kim, J. Y., Ahn, S., Chae, H. G., Kwon, B., and Son, J. S., 2021, “Cu₂Se-Based Thermoelectric Cellular Architectures for Efficient and Durable Power Generation,” *Nat. Commun.*, **12**(1), pp. 1–11.
- [9] Zhou, B., Luo, W., Yang, J., Duan, X., Wen, Y., Zhou, H., Chen, R., and Shan, B., 2016, “Thermal Conductivity of Aligned CNT/Polymer Composites Using Mesoscopic Simulation,” *Compos. Part A Appl. Sci. Manuf.*, **90**, pp. 410–416.
- [10] Xue, Q., 2004, “The Influence of Particle Shape and Size on Electric Conductivity of Metal-Polymer Composites,” *Eur. Polym. J.*, **40**(2), pp. 323–327.
- [11] Gong, S., Zhu, Z. H., and Meguid, S. A., 2015, “Anisotropic Electrical Conductivity of Polymer Composites with Aligned Carbon Nanotubes,” *Polymer (Guildf.)*, **56**, pp. 498–506.
- [12] Huang, Z., Zheng, Z., Zhao, S., Dong, S., Luo, P., and Chen, L., 2017, “Copper

Matrix Composites Reinforced by Aligned Carbon Nanotubes: Mechanical and Tribological Properties,” *Mater. Des.*, **133**, pp. 570–578.

- [13] Joshi, G., Lee, H., Lan, Y., Wang, X., Zhu, G., Wang, D., Gould, R. W., Cuff, D. C., Tang, M. Y., Dresselhaus, M. S., Chen, G., and Ren, Z., 2008, “Enhanced Thermoelectric Figure-of-Merit in Nanostructured p-Type Silicon Germanium Bulk Alloys,” *Nano Lett.*, **8**(12), pp. 4670–4674.
- [14] Sootsman, J. R., Chung, D. Y., and Kanatzidis, M. G., 2009, “New and Old Concepts in Thermoelectric Materials,” *Angew. Chemie - Int. Ed.*, **48**(46), pp. 8616–8639.
- [15] Jo, S., Park, S. H., Ban, H. W., Gu, D. H., Kim, B. S., Son, J. H., Hong, H. K., Lee, Z., Han, H. S., Jo, W., Lee, J. E., and Son, J. S., 2016, “Simultaneous Improvement in Electrical and Thermal Properties of Interface-Engineered BiSbTe Nanostructured Thermoelectric Materials,” *J. Alloys Compd.*, **689**, pp. 899–907.
- [16] Ge, Y., Liu, Z., Sun, H., and Liu, W., 2018, “Optimal Design of a Segmented Thermoelectric Generator Based on Three-Dimensional Numerical Simulation and Multi-Objective Genetic Algorithm,” *Energy*, **147**, pp. 1060–1069.
- [17] Sahin, A. Z., and Yilbas, B. S., 2013, “The Thermoelement as Thermoelectric Power Generator: Effect of Leg Geometry on the Efficiency and Power Generation,” *Energy Convers. Manag.*, **65**, pp. 26–32.
- [18] Picard, M., Turenne, S., Vasilevskiy, D., and Masut, R. A., 2013, “Numerical Simulation of Performance and Thermomechanical Behavior of Thermoelectric Modules with Segmented Bismuth-Telluride-Based Legs,” *J. Electron. Mater.*, **42**(7), pp. 2343–2349.
- [19] Erturun, U., Erermis, K., and Mossi, K., 2014, “Effect of Various Leg Geometries on Thermo-Mechanical and Power Generation Performance of Thermoelectric Devices,” *Appl. Therm. Eng.*, **73**(1), pp. 128–141.
- [20] Bell, L. E., 2008, “Cooling, Heating, Generating Power, and Recovering Waste Heat with Thermoelectric Systems,” *Science (80-.)*, **321**(5895), pp. 1457–1461.
- [21] Disalvo, F. J., 1999, “Thermoelectric Cooling and Power Generation,” *Science (80-.)*, **285**(5428), pp. 703–706.
- [22] He, J., and Tritt, T. M., 2017, “Advances in Thermoelectric Materials Research: Looking Back and Moving Forward,” *Science (80-.)*, **357**(6358), p. eaak9997.
- [23] Snyder, G. J., and Toberer, E. S., 2008, “Complex Thermoelectric Materials,” *Nat. Mater.*, **7**(2), pp. 105–114.
- [24] Zhang, Y., Cleary, M., Wang, X., Kempf, N., Schoensee, L., Yang, J., Joshi, G., and Meda, L., 2015, “High-Temperature and High-Power-Density Nanostructured Thermoelectric Generator for Automotive Waste Heat Recovery,” *Energy*

Convers. Manag., **105**, pp. 946–950.

- [25] Jo, S., Park, S. H., Ban, H. W., Gu, D. H., Kim, B. S., Son, J. H., Hong, H. K., Lee, Z., Han, H. S., Jo, W., Lee, J. E., and Son, J. S., 2016, “Simultaneous Improvement in Electrical and Thermal Properties of Interface-Engineered BiSbTe Nanostructured Thermoelectric Materials,” *J. Alloy. Comp.*, **689**, pp. 899–907.
- [26] Jo, S., Park, S. H., Shin, H., Oh, I., Heo, S. H., Ban, H. W., Jeong, H., Kim, F., Choo, S., Gu, D. H., Baek, S., Cho, S., Kim, J. S., Kim, B. S., Lee, J. E., Song, S., Yoo, J. W., Song, J. Y., and Son, J. S., 2019, “Soluble Telluride-Based Molecular Precursor for Solution-Processed High-Performance Thermoelectrics,” *ACS Appl. Energy Mater.*, **2**(7), pp. 4582–4589.
- [27] Kim, S. Il, Lee, K. H., Mun, H. A., Kim, H. S., Hwang, S. W., Roh, J. W., Yang, D. J., Shin, W. H., Li, X. S., Lee, Y. H., Snyder, G. J., and Kim, S. W., 2015, “Dense Dislocation Arrays Embedded in Grain Boundaries for High-Performance Bulk Thermoelectrics,” *Science (80-.)*, **348**(6230), pp. 109–114.
- [28] Zheng, G., Su, X., Xie, H., Shu, Y., Liang, T., She, X., Liu, W., Yan, Y., Zhang, Q., Uher, C., Kanatzidis, M. G., and Tang, X., 2017, “High Thermoelectric Performance of P-BiSbTe Compounds Prepared by Ultra-Fast Thermally Induced Reaction,” *Energy Environ. Sci.*, **10**(12), pp. 2638–2652.
- [29] Liu, H., Shi, X., Xu, F., Zhang, L., Zhang, W., Chen, L., Li, Q., Uher, C., Day, T., and Snyder Jeffrey, G., 2012, “Copper Ion Liquid-like Thermoelectrics,” *Nat. Mater.*, **11**(5), pp. 422–425.
- [30] Liu, W. Di, Yang, L., Chen, Z. G., and Zou, J., 2020, “Promising and Eco-Friendly Cu₂X-Based Thermoelectric Materials: Progress and Applications,” *Adv. Mater.*, **32**(8), p. e1905703.
- [31] Wei, T. R., Qin, Y., Deng, T., Song, Q., Jiang, B., Liu, R., Qiu, P., Shi, X., and Chen, L., 2018, “Copper Chalcogenide Thermoelectric Materials,” *Sci. China Mater.*, **62**(1), pp. 8–24.
- [32] Zhao, K., Qiu, P., Shi, X., and Chen, L., 2019, “Recent Advances in Liquid-like Thermoelectric Materials,” *Adv. Funct. Mater.*, **30**(8), p. 1903867.
- [33] Zong, P. A., Hanus, R., Dylla, M., Tang, Y., Liao, J., Zhang, Q., Snyder, G. J., and Chen, L., 2017, “Skutterudite with Graphene-Modified Grain-Boundary Complexion Enhances ZT Enabling High-Efficiency Thermoelectric Device,” *Energy Environ. Sci.*, **10**(1), pp. 183–191.
- [34] Xing, Y., Liu, R., Liao, J., Zhang, Q., Xia, X., Wang, C., Huang, H., Chu, J., Gu, M., Zhu, T., Zhu, C., Xu, F., Yao, D., Zeng, Y., Bai, S., Uher, C., and Chen, L., 2019, “High-Efficiency Half-Heusler Thermoelectric Modules Enabled by Self-Propagating Synthesis and Topologic Structure Optimization,” *Energy Environ. Sci.*, **12**(11), pp. 3390–3399.

- [35] Heo, S. H., Jo, S., Kim, H. S., Choi, G., Song, J. Y., Kang, J. Y., Park, N. J., Ban, H. W., Kim, F., Jeong, H., Jung, J., Jang, J., Lee, W. B., Shin, H., and Son, J. S., 2019, “Composition Change-Driven Texturing and Doping in Solution-Processed SnSe Thermoelectric Thin Films,” *Nat. Commun.*, **10**(1).
- [36] Zhao, L. D., Lo, S. H., Zhang, Y., Sun, H., Tan, G., Uher, C., Wolverton, C., Dravid, V. P., and Kanatzidis, M. G., 2014, “Ultralow Thermal Conductivity and High Thermoelectric Figure of Merit in SnSe Crystals,” *Nature*, **508**(7496), pp. 373–377.
- [37] Kraemer, D., Sui, J., McEnaney, K., Zhao, H., Jie, Q., Ren, Z. F., and Chen, G., 2015, “High Thermoelectric Conversion Efficiency of MgAgSb-Based Material with Hot-Pressed Contacts,” *Energy Environ. Sci.*, **8**(4), pp. 1299–1308.
- [38] Choi, J., Jung, Y., Yang, S. J., Oh, J. Y., Oh, J., Jo, K., Son, J. G., Moon, S. E., Park, C. R., and Kim, H., 2017, “Flexible and Robust Thermoelectric Generators Based on All-Carbon Nanotube Yarn without Metal Electrodes,” *ACS Nano*, **11**(8), pp. 7608–7614.
- [39] Gu, D. H., Jo, S., Jeong, H., Ban, H. W., Park, S. H., Heo, S. H., Kim, F., Jang, J. I., Lee, J. E., and Son, J. S., 2017, “Colloidal Synthesis of Te-Doped Bi Nanoparticles: Low-Temperature Charge Transport and Thermoelectric Properties,” *ACS Appl. Mater. Interfaces*, **9**(22), pp. 19143–19151.
- [40] Kim, J., Bae, E. J., Kang, Y. H., Lee, C., and Cho, S. Y., 2020, “Elastic Thermoelectric Sponge for Pressure-Induced Enhancement of Power Generation,” *Nano Energy*, **74**, p. 104824.
- [41] Ferreira-Teixeira, S., and Pereira, A. M., 2018, “Geometrical Optimization of a Thermoelectric Device: Numerical Simulations,” *Energy Convers. Manag.*, **169**, pp. 217–227.
- [42] Xing, T., Song, Q., Qiu, P., Zhang, Q., Gu, M., Xia, X., Liao, J., Shi, X., and Chen, L., 2021, “High Efficiency GeTe-Based Materials and Modules for Thermoelectric Power Generation,” *Energy Environ. Sci.*, **14**(2), pp. 995–1003.
- [43] Qiu, P., Mao, T., Huang, Z., Xia, X., Liao, J., Agne, M. T., Gu, M., Zhang, Q., Ren, D., Bai, S., Shi, X., Snyder, G. J., and Chen, L., 2019, “High-Efficiency and Stable Thermoelectric Module Based on Liquid-like Materials,” *Joule*, **3**(6), pp. 1538–1548.
- [44] Yeo, S. J., Oh, M. J., and Yoo, P. J., 2019, “Structurally Controlled Cellular Architectures for High Performance Ultra Lightweight Materials,” *Adv. Mater.*, **31**(34), p. 1803670.
- [45] Tian, X., and Zhou, K., 2020, “3D Printing of Cellular Materials for Advanced Electrochemical Energy Storage and Conversion,” *Nanoscale*, **12**(14), pp. 7416–7432.

- [46] Schaedler, T. A., Jacobsen, A. J., Torrents, A., Sorensen, A. E., Lian, J., Greer, J. R., Valdevit, L., and Carter, W. B., 2011, “Ultralight Metallic Microlattices,” *Science* (80-.), **334**(6058), pp. 962–965.
- [47] Berger, J. B., Wadley, H. N. G., and McMeeking, R. M., 2017, “Mechanical Metamaterials at the Theoretical Limit of Isotropic Elastic Stiffness,” *Nature*, **543**(7646), pp. 533–537.
- [48] Bauer, J., Hengsbach, S., Tesari, I., Schwaiger, R., and Kraft, O., 2014, “High-Strength Cellular Ceramic Composites with 3D Microarchitecture,” *Proc. Natl Acad. Sci. USA*, **111**(7), pp. 2453–2458.
- [49] Muth, J. T., Dixon, P. G., Woish, L., Gibson, L. J., and Lewis, J. A., 2017, “Architected Cellular Ceramics with Tailored Stiffness via Direct Foam Writing,” *Proc. Natl Acad. Sci. USA*, **114**(8), pp. 1832–1837.
- [50] Lewis, J. A., and Ahn, B. Y., 2015, “Three-Dimensional Printed Electronics,” *Nature*, **518**(7537), pp. 42–43.
- [51] Sun, K., Wei, T. S., Ahn, B. Y., Seo, J. Y., Dillon, S. J., and Lewis, J. A., 2013, “3D Printing of Interdigitated Li-Ion Microbattery Architectures,” *Adv. Mater.*, **25**(33), pp. 4539–4543.
- [52] He, M., Zhao, Y., Wang, B., Xi, Q., Zhou, J., and Liang, Z., 2015, “3D Printing Fabrication of Amorphous Thermoelectric Materials with Ultralow Thermal Conductivity,” *Small*, **11**(44), pp. 5889–5894.
- [53] Qiu, J., Yan, Y., Luo, T., Tang, K., Yao, L., Zhang, J., Zhang, M., Su, X., Tan, G., Xie, H., Kanatzidis, M. G., Uher, C., and Tang, X., 2019, “3D Printing of Highly Textured Bulk Thermoelectric Materials: Mechanically Robust BiSbTe Alloys with Superior Performance,” *Energy Environ. Sci.*, **12**(10), pp. 3106–3117.
- [54] Du, Y., Chen, J., Meng, Q., Xu, J., Paul, B., and Eklund, P., 2020, “Flexible Ternary Carbon Black/Bi₂Te₃ Based Alloy/Polylactic Acid Thermoelectric Composites Fabricated by Additive Manufacturing,” *J. Mater.*, **6**(2), pp. 293–299.
- [55] Oztan, C., Ballikaya, S., Ozgun, U., Karkkainen, R., and Celik, E., 2019, “Additive Manufacturing of Thermoelectric Materials via Fused Filament Fabrication,” *Appl. Mater. Today*, **15**, pp. 77–82.
- [56] Jo, S., Choo, S., Kim, F., Heo, S. H., and Son, J. S., 2019, “Ink Processing for Thermoelectric Materials and Power-Generating Devices,” *Adv. Mater.*, **31**(20), p. e1804930.
- [57] Aw, Y. Y., Yeoh, C. K., Idris, M. A., Teh, P. L., Hamzah, K. A., and Sazali, S. A., 2018, “Effect of Printing Parameters on Tensile, Dynamic Mechanical, and Thermoelectric Properties of FDM 3D Printed CABS/ZnO Composites,” *Materials (Basel)*, **11**(4), p. 466.

- [58] Su, N., Zhu, P., Pan, Y., Li, F., and Li, B., 2020, “3D-Printing of Shape-Controllable Thermoelectric Devices with Enhanced Output Performance,” *Energy*, **195**, p. 116892.
- [59] Yazawa, K., and Shakouri, A., 2017, “Optimization of Power and Efficiency of Thermoelectric Devices with Asymmetric Thermal Contacts,” *J. Appl. Phys.*, **111**(2), p. 024509.
- [60] Roh, I. J., Lee, Y. G., Kang, M. S., Lee, J. U., Baek, S. H., Kim, S. K., Ju, B. K., Hyun, D. Bin, Kim, J. S., and Kwon, B., 2016, “Harman Measurements for Thermoelectric Materials and Modules under Non-Adiabatic Conditions,” *Sci. Rep.*, **6**.
- [61] Meo, M., Morris, A. J., Vignjevic, R., and Marengo, G., 2003, “Numerical Simulations of Low-Velocity Impact on an Aircraft Sandwich Panel,” *Compos. Struct.*, **62**(3–4), pp. 3–4.
- [62] Lu, C., Zhao, M., Jie, L., Wang, J., Gao, Y., Cui, X., and Chen, P., 2015, “Stress Distribution on Composite Honeycomb Sandwich Structure Suffered from Bending Load,” *Procedia Eng.*, **99**, pp. 405–412.
- [63] Sun, G., Huo, X., Chen, D., and Li, Q., 2017, “Experimental and Numerical Study on Honeycomb Sandwich Panels under Bending and In-Panel Compression,” *Mater. Des.*, **133**, pp. 154–168.
- [64] Wang, X., Qiu, P., Zhang, T., Ren, D., Wu, L., Shi, X., Yang, J., and Chen, L., 2015, “Compound Defects and Thermoelectric Properties in Ternary CuAgSe-Based Materials,” *J. Mater. Chem. A*, **3**(26), pp. 13662–13670.
- [65] Xie, H., 2008, “The Role of Zn in Chalcopyrite CuFeS₂: Enhanced Thermoelectric Properties of Cu_{1-x}Zn_xFeS₂ with in Situ Nanoprecipitates,” *Adv. Energy Mater.*, **112**, pp. 521–525.
- [66] Zhao, L. D., Lo, S. H., Zhang, Y., Sun, H., Tan, G., Uher, C., Wolverton, C., Dravid, V. P., and Kanatzidis, M. G., 2014, “Ultralow Thermal Conductivity and High Thermoelectric Figure of Merit in SnSe Crystals,” *Nature*, **508**(7496), pp. 373–377.
- [67] Heremans, J. P., Jovovic, V., Toberer, E. S., Saramat, A., Kurosaki, K., Charoenphakdee, A., Yamanaka, S., and Snyder, G. J., 2008, “Enhancement of Thermoelectric Efficiency in PbTe by Distortion of the Electronic Density of States,” *Science (80-.)*, **321**(5888), pp. 554–557.
- [68] Sales, B. C., Mandrus, D., and Williams, R. K., 1996, “Filled Skutterudite Antimonides: A New Class of Thermoelectric Materials,” *Science (80-.)*, **272**(5266), pp. 1325–1328.
- [69] Lan, Y., Minnich, A. J., Chen, G., and Ren, Z., 2010, “Enhancement of

- Thermoelectric Figure-of-Merit by a Bulk Nanostructuring Approach,” *Adv. Funct. Mater.*, **20**(3), pp. 357–376.
- [70] Pei, Y., Shi, X., Lalonde, A., Wang, H., Chen, L., and Snyder, G. J., 2011, “Convergence of Electronic Bands for High Performance Bulk Thermoelectrics,” *Nature*, **473**(7345), pp. 66–69.
- [71] Hao, F., Qiu, P., Tang, Y., Bai, S., Xing, T., Chu, H. S., Zhang, Q., Lu, P., Zhang, T., Ren, D., Chen, J., Shi, X., and Chen, L., 2016, “High Efficiency Bi₂Te₃-Based Materials and Devices for Thermoelectric Power Generation between 100 and 300 °c,” *Energy Environ. Sci.*, **9**(10), pp. 3120–3127.
- [72] Mun, H., Choi, S. M., Lee, K. H., and Kim, S. W., 2015, “Boundary Engineering for the Thermoelectric Performance of Bulk Alloys Based on Bismuth Telluride,” *ChemSusChem*, **8**(14), pp. 2312–2326.
- [73] Seo, S., Desilva, M. A., Xia, H., and Brennecke, J. F., 2015, “Effect of Cation on Physical Properties and CO₂ Solubility for Phosphonium-Based Ionic Liquids with 2-Cyanopyrrolide Anions,” *J. Phys. Chem. B*, **119**(35), pp. 11807–11814.
- [74] Wei, Z., Li, Z., Luo, P., Zhang, J., and Luo, J., 2020, “Simultaneously Increased Carrier Concentration and Mobility in P-Type Bi_{0.5}Sb_{1.5}Te₃ Through Cd Doping,” *J. Alloys Compd.*, **830**.
- [75] Ngan, P. H., Christensen, D. V., Snyder, G. J., Hung, L. T., Linderoth, S., Nong, N. Van, and Pryds, N., 2014, “Towards High Efficiency Segmented Thermoelectric Unicouples,” *Phys. Status Solidi Appl. Mater. Sci.*, **211**(1), pp. 9–17.
- [76] Zhang, Q., Liao, J., Tang, Y., Gu, M., Ming, C., Qiu, P., Bai, S., Shi, X., Uher, C., and Chen, L., 2017, “Realizing a Thermoelectric Conversion Efficiency of 12% in Bismuth Telluride/Skutterudite Segmented Modules through Full-Parameter Optimization and Energy-Loss Minimized Integration,” *Energy Environ. Sci.*, **10**(4), pp. 956–963.
- [77] Badillo-Ruiz, C. A., Olivares-Robles, M. A., and Ruiz-Ortega, P. E., 2018, “Performance of Segmented Thermoelectric Cooler Micro-Elements with Different Geometric Shapes and Temperature-Dependent Properties,” *Entropy*, **20**(2).
- [78] Qiu, P., Mao, T., Huang, Z., Xia, X., Liao, J., Agne, M. T., Gu, M., Zhang, Q., Ren, D., Bai, S., Shi, X., Snyder, G. J., and Chen, L., 2019, “High-Efficiency and Stable Thermoelectric Module Based on Liquid-Like Materials,” *Joule*, **3**(6), pp. 1538–1548.
- [79] Pu, H. Y., Xie, R. Q., Peng, Y., Yang, Y., He, S. Y., Luo, J., Sun, Y., Xie, S. R., and Luo, J., 2019, “Accelerating Sample Preparation of Graded Thermoelectric Materials Using an Automatic Powder Feeding System,” *Adv. Manuf.*, **7**(3), pp.

278–287.

- [80] Qi, X., Chen, J., Guo, K., He, S., Yang, J., Li, Z., Xing, J., Hu, J., Luo, H., Zhang, W., and Luo, J., 2019, “Thermal Stability of Ag₉GaSe₆ and Its Potential as a Functionally Graded Thermoelectric Material,” *Chem. Eng. J.*, **374**, pp. 494–501.
- [81] Gelbstein, Y., Dashevsky, Z., and Dariel, M. P., 2007, “Powder Metallurgical Processing of Functionally Graded P-Pb₁-XSn_xTe Materials for Thermoelectric Applications,” *Phys. B Condens. Matter*, **391**(2), pp. 256–265.
- [82] Farahani, R. D., Dubé, M., and Therriault, D., 2016, “Three-Dimensional Printing of Multifunctional Nanocomposites: Manufacturing Techniques and Applications,” *Adv. Mater.*, **28**(28), pp. 5794–5821.
- [83] Burton, M. R., Mehraban, S., Beynon, D., McGettrick, J., Watson, T., Lavery, N. P., and Carnie, M. J., 2019, “3D Printed SnSe Thermoelectric Generators with High Figure of Merit,” *Adv. Energy Mater.*, **9**(26).
- [84] Skylar-Scott, M. A., Mueller, J., Visser, C. W., and Lewis, J. A., 2019, “Voxelated Soft Matter via Multimaterial Multinozzle 3D Printing,” *Nature*, **575**(7782), pp. 330–335.
- [85] Hardin, J. O., Ober, T. J., Valentine, A. D., and Lewis, J. A., 2015, “Microfluidic Printheads for Multimaterial 3D Printing of Viscoelastic Inks,” *Adv. Mater.*, **27**(21), pp. 3279–3284.
- [86] Crane, D. T., Kossakovski, D., and Bell, L. E., 2009, “Modeling the Building Blocks of a 10% Efficient Segmented Thermoelectric Power Generator,” *J. Electron. Mater.*, **38**(7), pp. 1382–1386.
- [87] Anatyshuk, L. I., Vikhor, L. N., Strutynska, L. T., and Termena, I. S., 2011, “Segmented Generator Modules Using Bi₂Te₃-Based Materials,” *J. Electron. Mater.*, **40**(5), pp. 957–961.
- [88] Kuroki, T., Kabeya, K., Makino, K., Kajihara, T., Kaibe, H., Hachiuma, H., Matsuno, H., and Fujibayashi, A., 2014, “Thermoelectric Generation Using Waste Heat in Steel Works,” *J. Electron. Mater.*, **43**(6), pp. 2405–2410.
- [89] Dalmas, F., Dendievel, R., Chazeau, L., Cavaillé, J. Y., and Gauthier, C., 2006, “Carbon Nanotube-Filled Polymer Composites. Numerical Simulation of Electrical Conductivity in Three-Dimensional Entangled Fibrous Networks,” *Acta Mater.*, **54**(11), pp. 2923–2931.
- [90] Hone, J., Llaguno, M. C., Nemes, N. M., Johnson, A. T., Fischer, J. E., Walters, D. A., Casavant, M. J., Schmidt, J., and Smalley, R. E., 2000, “Electrical and Thermal Transport Properties of Magnetically Aligned Single Wall Carbon Nanotube Films,” *Appl. Phys. Lett.*, **77**(5), pp. 666–668.
- [91] Wang, H., Zhang, Z. H., Hu, Z. Y., Song, Q., and Yin, S. P., 2018, “Interface

Structure and Properties of CNTs/Cu Composites Fabricated by Electroless Deposition and Spark Plasma Sintering,” *Mater. Res. Express*, **5**(1).

- [92] Ghorbani-Asl, M., Bristowe, P. D., and Koziol, K., 2015, “A Computational Study of the Quantum Transport Properties of a Cu-CNT Composite,” *Phys. Chem. Chem. Phys.*, **17**(28), pp. 18273–18277.
- [93] Hjortstam, O., Isberg, P., Söderholm, S., and Dai, H., 2004, “Can We Achieve Ultra-Low Resistivity in Carbon Nanotube-Based Metal Composites?,” *Appl. Phys. A Mater. Sci. Process.*, **78**(8), pp. 1175–1179.
- [94] Sundaram, R. M., Sekiguchi, A., Sekiya, M., Yamada, T., and Hata, K., 2018, “Copper/Carbon Nanotube Composites: Research Trends and Outlook,” *R. Soc. Open Sci.*, **5**(11).
- [95] Chu, K., Guo, H., Jia, C., Yin, F., Zhang, X., Liang, X., and Chen, H., 2010, “Thermal Properties of Carbon Nanotube-Copper Composites for Thermal Management Applications,” *Nanoscale Res. Lett.*, **5**(5), pp. 868–874.
- [96] Xu, Z., and Buehler, M. J., 2009, “Nanoengineering Heat Transfer Performance at Carbon Nanotube Interfaces,” *ACS Nano*, **3**(9), pp. 2767–2775.
- [97] Zhao, J., Rao, Z., and Li, Y., 2015, “Thermal Performance of Mini-Channel Liquid Cooled Cylinder Based Battery Thermal Management for Cylindrical Lithium-Ion Power Battery,” *Energy Convers. Manag.*, **103**, pp. 157–165.
- [98] Huang, H., Liu, C., Wu, Y., and Fan, S., 2005, “Aligned Carbon Nanotube Composite Films for Thermal Management,” *Adv. Mater.*, **17**(13), pp. 1652–1656.
- [99] Yoo, S. J., Han, S. H., and Kim, W. J., 2013, “A Combination of Ball Milling and High-Ratio Differential Speed Rolling for Synthesizing Carbon Nanotube/Copper Composites,” *Carbon N. Y.*, **61**, pp. 487–500.
- [100] Khaleghi, E., Torikachvili, M., Meyers, M. A., and Olevsky, E. A., 2012, “Magnetic Enhancement of Thermal Conductivity in Copper-Carbon Nanotube Composites Produced by Electroless Plating, Freeze Drying, and Spark Plasma Sintering,” *Mater. Lett.*, **79**, pp. 256–258.
- [101] Park, Cheol ; Wilkinson, John ; Banda, Sumanth ; Ounaies, Zoubeida ; Wise, Kristopher E ; Sauti, Godfrey ; Lillehei, Peter T ; Harrison, J. S., 2006, “Aligned Single-Wall Carbon Nanotube Polymer Composites Using an Electric Field,” *J. Polym. Sci.*, **44**(12), pp. 1751–1762.
- [102] Choi, E. S., Brooks, J. S., Eaton, D. L., Al-Haik, M. S., Hussaini, M. Y., Garmestani, H., Li, D., and Dahmen, K., 2003, “Enhancement of Thermal and Electrical Properties of Carbon Nanotube Polymer Composites by Magnetic Field Processing,” *J. Appl. Phys.*, **94**(9), pp. 6034–6039.
- [103] Dai, J., Wang, Q., Li, W., Wei, Z., and Xu, G., 2007, “Properties of Well Aligned

SWNT Modified Poly (Methyl Methacrylate) Nanocomposites,” *Mater. Lett.*, **61**(1), pp. 27–29.

- [104] Wang, Q., Dai, J., Li, W., Wei, Z., and Jiang, J., 2008, “The Effects of CNT Alignment on Electrical Conductivity and Mechanical Properties of SWNT/Epoxy Nanocomposites,” *Compos. Sci. Technol.*, **68**(7–8), pp. 1644–1648.
- [105] Gupta, P., Rajput, M., Singla, N., Kumar, V., and Lahiri, D., 2016, “Electric Field and Current Assisted Alignment of CNT inside Polymer Matrix and Its Effects on Electrical and Mechanical Properties,” *Polymer (Guildf.)*, **89**, pp. 119–127.
- [106] Subramaniam, C., Yamada, T., Kobashi, K., Sekiguchi, A., Futaba, D. N., Yumura, M., and Hata, K., 2013, “One Hundred Fold Increase in Current Carrying Capacity in a Carbon Nanotube-Copper Composite,” *Nat. Commun.*, **4**, pp. 1–7.
- [107] Subramaniam, C., Yasuda, Y., Takeya, S., Ata, S., Nishizawa, A., Futaba, D., Yamada, T., and Hata, K., 2014, “Carbon Nanotube-Copper Exhibiting Metal-like Thermal Conductivity and Silicon-like Thermal Expansion for Efficient Cooling of Electronics,” *Nanoscale*, **6**(5), pp. 2669–2674.
- [108] Sun, S., Mu, W., Edwards, M., Mencarelli, D., Pierantoni, L., Fu, Y., Jeppson, K., and Liu, J., 2016, “Vertically Aligned CNT-Cu Nano-Composite Material for Stacked through-Silicon-via Interconnects,” *Nanotechnology*, **27**(33).
- [109] Subramaniam, C., Sekiguchi, A., Yamada, T., Futaba, D. N., and Hata, K., 2016, “Nano-Scale, Planar and Multi-Tiered Current Pathways from a Carbon Nanotube-Copper Composite with High Conductivity, Ampacity and Stability,” *Nanoscale*, **8**(7), pp. 3888–3894.
- [110] Liu, L., Ma, W., and Zhang, Z., 2011, “Macroscopic Carbon Nanotube Assemblies: Preparation, Properties, and Potential Applications,” *Small*, **7**(11), pp. 1504–1520.
- [111] Jorio, A., Saito, R., Hertel, T., Weisman, R. B., Dresselhaus, G., and Dresselhaus, M. S., 2018, “Carbon Nanotube Photophysics,” (April 2004).
- [112] Zeng, W., Shu, L., Li, Q., Chen, S., Wang, F., and Tao, X. M., 2014, “Fiber-Based Wearable Electronics: A Review of Materials, Fabrication, Devices, and Applications,” *Adv. Mater.*, **26**(31), pp. 5310–5336.
- [113] Xue, Q. Z., 2006, “Model for the Effective Thermal Conductivity of Carbon Nanotube Composites,” *Nanotechnology*, **17**(6), pp. 1655–1660.
- [114] Nan, C. W., Shi, Z., and Lin, Y., 2003, “A Simple Model for Thermal Conductivity of Carbon Nanotube-Based Composites,” *Chem. Phys. Lett.*, **375**(5–6), pp. 666–669.
- [115] Kim, K. T., Eckert, J., Liu, G., Park, J. M., Lim, B. K., and Hong, S. H., 2011, “Influence of Embedded-Carbon Nanotubes on the Thermal Properties of Copper

Matrix Nanocomposites Processed by Molecular-Level Mixing,” *Scr. Mater.*, **64**(2), pp. 181–184.

- [116] Zhong, H., and Lukes, J. R., 2006, “Interfacial Thermal Resistance between Carbon Nanotubes: Molecular Dynamics Simulations and Analytical Thermal Modeling,” *Phys. Rev. B - Condens. Matter Mater. Phys.*, **74**(12), pp. 1–10.
- [117] Chu, K., Jia, C. C., and Li, W. S., 2013, “Thermal Conductivity Enhancement in Carbon Nanotube/Cu-Ti Composites,” *Appl. Phys. A Mater. Sci. Process.*, **110**(2), pp. 269–273.
- [118] Wilhite, P., Vyas, A. A., Tan, J., Tan, J., Yamada, T., Wang, P., Park, J., and Yang, C. Y., 2014, “Metal-Nanocarbon Contacts,” *Semicond. Sci. Technol.*, **29**(5).
- [119] Zuo, T., Li, J., Gao, Z., Zhang, L., Da, B., Zhao, X., Ding, F., Li, S., Yang, Y., and Xiao, L., 2020, “Enhanced Electrical Conductivity and Hardness of Copper/Carbon Nanotubes Composite by Tuning the Interface Structure,” *Mater. Lett.*, **280**, pp. 1–4.
- [120] Zuo, T., Li, J., Gao, Z., Wu, Y., Zhang, L., Da, B., Zhao, X., and Xiao, L., 2020, “Simultaneous Improvement of Electrical Conductivity and Mechanical Property of Cr Doped Cu/CNTs Composites,” *Mater. Today Commun.*, **23**(January).
- [121] Kong, J., Zhang, C. Y., and Cheng, X., 2013, “Novel Cu-Cr Alloy Matrix CNT Composites with Enhanced Thermal Conductivity,” *Appl. Phys. A Mater. Sci. Process.*, **112**(3), pp. 631–636.
- [122] Milowska, K. Z., Ghorbani-Asl, M., Burda, M., Wolanicka, L., Čatić, N., Bristowe, P. D., and Koziol, K. K. K., 2017, “Breaking the Electrical Barrier between Copper and Carbon Nanotubes,” *Nanoscale*, **9**(24), pp. 8458–8469.
- [123] Nie, J., Jia, C., Jia, X., Zhang, Y., Shi, N., and Li, Y., 2011, “Fabrication, Microstructures, and Properties of Copper Matrix Composites Reinforced by Molybdenum-Coated Carbon Nanotubes,” *Rare Met.*, **30**(4), pp. 401–407.
- [124] Cola, B. A., Xu, J., and Fisher, T. S., 2009, “Contact Mechanics and Thermal Conductance of Carbon Nanotube Array Interfaces,” *Int. J. Heat Mass Transf.*, **52**(15–16), pp. 3490–3503.
- [125] Nirmalraj, P. N., Lyons, P. E., De, S., Coleman, J. N., and Boland, J. J., 2009, “Electrical Connectivity in Single-Walled Carbon Nanotube Networks,” *Nano Lett.*, **9**(11), pp. 3890–3895.
- [126] Gong, S., Zhu, Z. H., and Haddad, E. I., 2013, “Modeling Electrical Conductivity of Nanocomposites by Considering Carbon Nanotube Deformation at Nanotube Junctions,” *J. Appl. Phys.*, **114**(7), pp. 1–10.
- [127] Narayanunni, V., Gu, H., and Yu, C., 2011, “Monte Carlo Simulation for Investigating Influence of Junction and Nanofiber Properties on Electrical

- Conductivity of Segregated-Network Nanocomposites,” *Acta Mater.*, **59**(11), pp. 4548–4555.
- [128] Shkolnik, K., and Chalivendra, V., 2018, “Numerical Studies of Electrical Contacts of Carbon Nanotubes-Embedded Epoxy under Tensile Loading,” *Acta Mech.*, **229**(1), pp. 99–107.
- [129] Li, B. J., Ma, P. C., Chow, W. S., To, C. K., Tang, B. Z., and Kim, J., 2007, “Correlations between Percolation Threshold , Dispersion State , and Aspect Ratio of Carbon Nanotubes,” pp. 3207–3215.
- [130] Coleman, J. N., Curran, S., Dalton, A. B., Davey, A. P., Mccarthy, B., Blau, W., and Barklie, R. C., 1998, “Percolation-Dominated Conductivity in a Conjugated-Polymer-Carbon-Nanotube Composite,” *Phys. Rev. B*, **58**(12), pp. 7492–7495.
- [131] Allaoui, A., Hoa, S. V., Evesque, P., and Bai, J. B., 2009, “Electronic Transport in Carbon Nanotube Tangles under Compression: The Role of Contact Resistance,” *Scr. Mater.*, **61**(6), pp. 628–631.
- [132] Rahman, R., and Servati, P., 2014, “Efficient Analytical Model of Conductivity of CNT / Polymer Composites for Wireless Gas Sensors,” (c), pp. 1–12.
- [133] Foygel, M., Morris, R. D., Anez, D., French, S., and Sobolev, V. L., 2005, “Theoretical and Computational Studies of Carbon Nanotube Composites and Suspensions: Electrical and Thermal Conductivity,” *Phys. Rev. B - Condens. Matter Mater. Phys.*, **71**(10), pp. 1–8.
- [134] Deng, F., and Zheng, Q. S., 2008, “An Analytical Model of Effective Electrical Conductivity of Carbon Nanotube Composites,” *Appl. Phys. Lett.*, **92**(7), pp. 90–93.
- [135] Bagchi, A., and Nomura, S., 2006, “On the Effective Thermal Conductivity of Carbon Nanotube Reinforced Polymer Composites,” *Compos. Sci. Technol.*, **66**(11–12), pp. 1703–1712.
- [136] Mohiuddin, M., and Hoa, S. V., 2013, “Estimation of Contact Resistance and Its Effect on Electrical Conductivity of CNT/PEEK Composites,” *Compos. Sci. Technol.*, **79**, pp. 42–48.
- [137] Che, Jianwei ; Çagin, Tahir ; Goddard III, W. A., 2000, “Thermal Conductivity of Carbon Nanotubes,” *Nanotechnology*, **11**(2), pp. 65–69.
- [138] Wang, J., Xie, H., Xin, Z., and Li, Y., 2010, “Increasing the Thermal Conductivity of Palmitic Acid by the Addition of Carbon Nanotubes,” *Carbon N. Y.*, **48**(14), pp. 3979–3986.
- [139] Li, S., Yu, Z., Rutherglen, C., and Burke, P. J., 2004, “Electrical Properties of 0.4 Cm Long Single-Walled Carbon Nanotubes,” *Nano Lett.*, **4**(10), pp. 2003–2007.

- [140] Kane, A. A., Sheps, T., Branigan, E. T., Apkarian, V. A., Cheng, M. H., Hemminger, J. C., Hunt, S. R., and Collins, P. G., 2009, “Graphitic Electrical Contacts to Metallic Single-Walled Carbon Nanotubes Using Pt Electrodes,” *Nano Lett.*, **9**(10), pp. 3586–3591.
- [141] Matsuda, Y., Deng, W. Q., and Goddard, W. A., 2010, “Contact Resistance for ‘End-Contacted’ Metal-Graphene and Metal-Nanotube Interfaces from Quantum Mechanics,” *J. Phys. Chem. C*, **114**(41), pp. 17845–17850.
- [142] Tong, T., Zhao, Y., Delzeit, L., Majumdar, A., and Kashani, A., 2017, “Multiwalled Carbon Nanotube/Nanofiber Arrays as Conductive and Dry Adhesive Interface Materials,” *Proc. ASME 2004 3rd Integr. Nanosyst. Conf. Des. Synth. Appl.*, pp. 1–6.
- [143] Park, M., Cola, B. A., Siegmund, T., Xu, J., Maschmann, M. R., Fisher, T. S., and Kim, H., 2006, “Effects of a Carbon Nanotube Layer on Electrical Contact Resistance between Copper Substrates,” *Nanotechnology*, **17**(9), pp. 2294–2303.
- [144] Lim, S. C., Jang, J. H., Bae, D. J., Han, G. H., Lee, S., Yeo, I. S., and Lee, Y. H., 2009, “Contact Resistance between Metal and Carbon Nanotube Interconnects: Effect of Work Function and Wettability,” *Appl. Phys. Lett.*, **95**(26), pp. 1–4.
- [145] Akbarpour, M. R., Mousa Mirabad, H., Alipour, S., and Kim, H. S., 2020, “Enhanced Tensile Properties and Electrical Conductivity of Cu-CNT Nanocomposites Processed via the Combination of Flake Powder Metallurgy and High Pressure Torsion Methods,” *Mater. Sci. Eng. A*, **773**(September 2019), p. 138888.
- [146] Pan, Y., Xiao, S. Q., Lu, X., Zhou, C., Li, Y., Liu, Z. W., Liu, B. W., Xu, W., Jia, C. C., and Qu, X. H., 2019, “Fabrication, Mechanical Properties and Electrical Conductivity of Al₂O₃ Reinforced Cu/CNTs Composites,” *J. Alloys Compd.*, **782**, pp. 1015–1023.
- [147] Daoush, W. M., Lim, B. K., Mo, C. B., Nam, D. H., and Hong, S. H., 2009, “Electrical and Mechanical Properties of Carbon Nanotube Reinforced Copper Nanocomposites Fabricated by Electroless Deposition Process,” *Mater. Sci. Eng. A*, **513–514**(C), pp. 247–253.
- [148] Nie, J. H., Jia, C. C., Jia, X., Li, Y., Zhang, Y. F., and Liang, X. B., 2012, “Fabrication and Thermal Conductivity of Copper Matrix Composites Reinforced by Tungsten-Coated Carbon Nanotubes,” *Int. J. Miner. Metall. Mater.*, **19**(5), pp. 446–452.
- [149] Krizhevsky, B. A., Sutskever, I., and Hinton, G. E., 2012, “ImageNet Classification with Deep Convolutional Neural Networks,” *Commun. ACM*, **60**(6), pp. 84–90.
- [150] Mikolov, T., Deoras, A., Povey, D., Burget, L., and Černocký, J., 2011, “Strategies

for Training Large Scale Neural Network Language Models,” 2011 IEEE Work. Autom. Speech Recognit. Understanding, ASRU 2011, Proc., pp. 196–201.

- [151] Kang, M., and Kwon, B., 2022, “Deep Learning of Forced Convection Heat Transfer,” *J. Heat Transfer*, **144**(2), pp. 1–7.
- [152] Raissi, M., Yazdani, A., and Karniadakis, G. E., 2020, “Hidden Fluid Mechanics: Learning Velocity and Pressure Fields from Flow Visualizations,” *Science (80-.)*, **367**(6481), pp. 1026–1030.
- [153] Edalatifar, M., Tavakoli, M. B., Ghalambaz, M., and Setoudeh, F., 2021, “Using Deep Learning to Learn Physics of Conduction Heat Transfer,” *J. Therm. Anal. Calorim.*, **146**(3), pp. 1435–1452.
- [154] Yang, L., Dai, W., Rao, Y., and Chyu, M. K., 2019, “Optimization of the Hole Distribution of an Effusively Cooled Surface Facing Non-Uniform Incoming Temperature Using Deep Learning Approaches,” *Int. J. Heat Mass Transf.*, **145**, p. 118749.
- [155] Kwon, B., Ejaz, F., and Hwang, L. K., 2020, “Machine Learning for Heat Transfer Correlations,” *Int. Commun. Heat Mass Transf.*, **116**(June), p. 104694.
- [156] Wei, H., Zhao, S., Rong, Q., and Bao, H., 2018, “Predicting the Effective Thermal Conductivities of Composite Materials and Porous Media by Machine Learning Methods,” *Int. J. Heat Mass Transf.*, **127**, pp. 908–916.
- [157] Lee, K. W., Son, H. S., Cho, K. S., and Choi, H. J., 2022, “Effect of Interfacial Bridging Atoms on the Strength of Al/CNT Composites: Machine-Learning-Based Prediction and Experimental Validation,” *J. Mater. Res. Technol.*, **17**, pp. 1770–1776.
- [158] Matos, M. A. S., Pinho, S. T., and Tagarielli, V. L., 2019, “Application of Machine Learning to Predict the Multiaxial Strain-Sensing Response of CNT-Polymer Composites,” *Carbon N. Y.*, **146**, pp. 265–275.
- [159] Le, T. T., 2021, “Prediction of Tensile Strength of Polymer Carbon Nanotube Composites Using Practical Machine Learning Method,” *J. Compos. Mater.*, **55**(6), pp. 787–811.
- [160] Faizan Ejaz, Munku Kang, Beomjin kwon, “A Two-Dimensional Finite Element Model for Cu-CNT Composite: The Impact of Interface Resistances on Electrical and Thermal Transports,” pp. 1–34.
- [161] Ren, S., He, K., Girshick, R., and Sun, J., 2017, “Faster R-CNN: Towards Real-Time Object Detection with Region Proposal Networks,” *IEEE Trans. Pattern Anal. Mach. Intell.*, **39**(6), pp. 1137–1149.
- [162] Russakovsky, O., Deng, J., Su, H., Krause, J., Satheesh, S., Ma, S., Huang, Z., Karpathy, A., Khosla, A., Bernstein, M., Berg, A. C., and Fei-Fei, L., 2015,


- “ImageNet Large Scale Visual Recognition Challenge,” *Int. J. Comput. Vis.*, **115**(3), pp. 211–252.
- [163] He, K., Zhang, X., Ren, S., and Sun, J., 2016, “Deep Residual Learning for Image Recognition,” *Proc. IEEE Comput. Soc. Conf. Comput. Vis. Pattern Recognit.*, **2016-Decem**, pp. 770–778.
- [164] LeCun, Y., Bottou, L., Bengio, Y., and Haffner, P., 1998, “Gradient-Based Learning Applied to Document Recognition,” *Proc. IEEE*, **86**(11), pp. 2278–2323.
- [165] Günen, M. A., 2022, “Performance Comparison of Deep Learning and Machine Learning Methods in Determining Wetland Water Areas Using EuroSAT Dataset,” *Environ. Sci. Pollut. Res.*, **29**(14), pp. 21092–21106.
- [166] Dariyal, P., Arya, A. K., Singh, B. P., and Dhakate, S. R., 2021, “A Review on Conducting Carbon Nanotube Fibers Spun via Direct Spinning Technique,” *J. Mater. Sci.*, **56**(2), pp. 1087–1115.
- [167] Kim, S. G., Choi, G. M., Jeong, H. D., Lee, D., Kim, S., Ryu, K. H., Lee, S., Kim, J., Hwang, J. Y., Kim, N. D., Kim, D. Y., Lee, H. S., and Ku, B. C., 2022, “Hierarchical Structure Control in Solution Spinning for Strong and Multifunctional Carbon Nanotube Fibers,” *Carbon N. Y.*, **196**(April), pp. 59–69.
- [168] Zhang, X., Lu, W., Zhou, G., and Li, Q., 2020, “Understanding the Mechanical and Conductive Properties of Carbon Nanotube Fibers for Smart Electronics,” *Adv. Mater.*, **32**(5), pp. 1–21.
- [169] Behabtu, N., Green, M. J., and Pasquali, M., 2008, “Carbon Nanotube-Based Neat Fibers,” *Nano Today*, **3**(5–6), pp. 24–34.
- [170] Zhang, X., Lin, H., Shang, H., Xu, J., Zhu, J., and Huang, W., 2021, “Recent Advances in Functional Fiber Electronics,” *SusMat*, **1**(1), pp. 105–126.
- [171] Taylor, L. W., Dewey, O. S., Headrick, R. J., Komatsu, N., Peraca, N. M., Wehmeyer, G., Kono, J., and Pasquali, M., 2021, “Improved Properties, Increased Production, and the Path to Broad Adoption of Carbon Nanotube Fibers,” *Carbon N. Y.*, **171**, pp. 689–694.
- [172] Bai, Y., Zhang, R., Ye, X., Zhu, Z., Xie, H., Shen, B., Cai, D., Liu, B., Zhang, C., Jia, Z., Zhang, S., Li, X., and Wei, F., 2018, “Carbon Nanotube Bundles with Tensile Strength over 80 GPa,” *Nat. Nanotechnol.*, **13**(7), pp. 589–595.

APPENDIX A
PERMISSION STATEMENTS

Permission Statement From: Jae Sung Son

CONSENT FORM

Faizan Ejaz has my permission to use our published articles, "Cu₂Se-based thermoelectric cellular architectures for efficient and durable power generation" and "Composition-segmented BiSbTe thermoelectric generator fabricated by multimaterial 3D printing" in his PhD thesis titled "Effect of Advanced Material Morphologies on Thermal, Electrical and Thermo-electrical Properties".

Permission Approved By (Signature):  Dated: Mar. 09, 2023

Permission Statement From: Dong Su Lee

CONSENT FORM

Faizan Ejaz has my permission to use our published articles, "A two-dimensional finite element model for Cu-CNT composite: The impact of interface resistances on electrical and thermal transports" and "Convolutional neural networks for approximating electrical and thermal conductivities of Cu-CNT composites" in his PhD thesis titled "Effect of Advanced Material Morphologies on Thermal, Electrical and Thermo-electrical Properties".

Permission Approved By (Signature):  Dated: March 09, 2023